Search for a Supersymmetric Higgs Boson using Multilepton Signatures with the CMS Detector at the Large Hadron Collider

Department of Physics
Graduate School, Chonnam National University

Kim, Zero Jaeho

A dissertation
submitted in partial fulfillment of the reuirements for the degree of
Doctor of Philosophy
in Physics

August 2013

"Let there be light", and there was light

Genesis 1:3, the Hole Bible

Abstract

Search for a Supersymmetric Higgs Boson using Multilepton Signatures with the CMS Detector at the Large Hadron Collider

Kim, Zero Jaeho

Department of Physics
Graduate School, Chonnam National University
(Supervised by Professor Jae Yool Kim)

A search for supersymmetric higgs boson in proton-proton collisions at $\sqrt{s} = 8$ TeV is presented, focusing on events with three and four leptons and large missing energy. The analyzed data corresponds to a total integrated luminosity of 19.5 fb^{-1} recorded by the CMS detector. The search uses a fully data-driven method to estimates residual Standard Model backgrounds. The analysis is performed on both of the channel of $\mu\mu+\mu(e)$ and $\mu\mu+\mu\mu(ee)$, The observed event rates are in agreement with expectations from the standard model. The results are used to set limits on the direct production of charginos, neutralinos, and sleptons in terms of limits on the parameter space, as well as a Simplified Model and Gauge Mediated Supersymmetry Breaking model. And the GMSB models with region of mass parameter μ between 330 and 370 for $\mu\mu + \mu$ and over 310 for $\mu\mu + e$ channel, which has the theoretical cross section out of the 95% C.L expected limit with two standard deviation, is proposed to check across with relevant study repeatedly.

Acknowledgements

First and foremost, I thank GOD for giving me today.

My special gratitude is to my excellent supervisor, prof. Jae Yool Kim, for his invaluable support, guidance, encouragement over five years. And I love to express my deepest gratitude to prof. In-taek Lim, prof. Kyung Kwang Joo, who encouraged me to take a progressive attitude with warm and bitter advice. Besides, I feel thankful to many professors from department of physics at Chonnam National University for executive help to make best environment for research.

I cannot but thanks to the Ministry of Education and Science Technology, the National Research Foundation of Korea and Jeollanamdo Office of Education, Hanbit high school at South Korea to stay at Switzerland and France and work for CERN. And specially I express my gratitude to korean CMS group, many professors and the members.

I specially thanks that the convenor of SUSY group, Oliver Buchmueller, from Imperial College guided me to SUSY research and gave me the first step to work in the first year at CERN. In addition to that wonderful beginners luck, Henning Flacher and Tom Whynite practiced me to make up the research environment, concerned theoretical background. In spite of my senseless and unaccustomed follow up, I deeply feel thankful to Imperial College group.

And Frederic Ronga from ETH Zurich gave me one more step to multi-lepton group, that makse me to face an excellent and joyful study which will be never happen again. Especially I express my deepest gratitude to David Stuart from University of Califonia Santa Barbara for his becoming my adviser with a good grace when I wander around. He has made much time to advise on my study in spite of his very busy time, so that I can understand an analysis more and do work hard more.

There are so many thankful people in SUSY multi-lepton group. James Smith from University of Colorado, Richard Gray from Rutgers University gave an advice in the practical side. Especially I thanks Karlsruhe Institute of Technology(KIT) and Wim de Boer, Martin Niegel, Valery Zhukov, Daniel Troendle, Stefan Wayand helped me to skim ntuples and checked my analysis step by step so many times, that strengthen my ability to stand alone. Although I have much lack of research still now, I cannot forget those much kind help of KIT group.

I hope to appreciate Marcello Maggi and Raffaello Trentadue from INFN, Alberto Andress Ocampo from Ghent University, Camilo Carrillo from Universidad de los andes gave me an unforgettable works and remembrance in Muon RPC team of Detector Performance Group.

I have another special memory in my study on analysis. CMS Data Analysis School held in 2012 January at Pisa in Italy present so many theoretical and practical expertise to me. I express my gratitude to Fabrizio Pala, Gigi Rolandi, Tommaso Boccali and Local Organizing Committee for preparing the best school. Its my luck to meet Pablo Martinez from ETH Zurich to enhance my eye of SUSY study.

Definitely all those happiness could never be in existence without LHC. I appreciate every members concerned to design, construct, maintain the LHC and CMS with best condition, and to accomplish every LHC project.

I would love to show my repect much more to CMS SUSY group and the leadership of current and previous conveners, Olive Buchmueller, Jeff Richman, David Stuart, Alex Tapper, Frederic Ronga, Eva Halkiadakis, Filip Moortgat, Didar Dobur, Ben Hooberman. That made me a big challenge even though I am still just like a kid in research.

And I thank my friends, Sanghyeon Song, Junsu Lee, Geonhee Oh, Ryeonggyun Park, In-Seok Jeong, from the Institute of Universe and Elementary Particles at Chonnam National University for giving deep discussions so many times.

Now I cannot mention the advice from the best teachers I had in my high school days, Jong Geun Kim and Jae Hak Woo, who work for Gwangju high school and Yudeok Middle school each as a principal and vice-principal now. I could not take all of these changes without their special advice.

Finally, I love to express my deepest respect to my parent who became a prop for me in every aspect for a very long time. And I have a deep sense of gratitude to my lover, Mme. Jung, for being with me as an best encourager even in Switzerland and France so far from hometown in Korea.

Contents

List of Figures

List of Tables

Chapter 1

Introduction

'In the beginning God created the heavens and the earth.'

Where we did come from? What is the world made of? And how does the nature work? A human has been seeking to the basic answer for those questions. A natural philosopher has studied the fundamental constituents of matter and their interactions. However, which particles are regarded as fundamental has changed with time as physicists knowledge has improved.

Modern theroy-called the standard model-attemps to explain all the phenomena of physics in terms of the properties and interactions of a small number of particles of three distinct types.

The standard model (SM) has been extremely successful in describing a wide range of phenomena in particle physics, and has survived some four decades of experimental testing. However, the only remaining undiscovered particle predicted by the SM, the Higgs boson [3] [4] [5] [6], suffers from quadratically divergent self-energy corrections at high energies [8]. Numerous extensions to the SM have been proposed to address these divergences. One such model, supersymmetry, a symmetry between fundamental bosons and fermions, results in cancellation of the divergences at tree level. The minimal supersymmetric extension to the standard model (MSSM) requires the presence of two Higgs doublets. This leads to a more complicated scalar sector, with five massive Higgs bosons: a light neutral state (h), two charged states ($H^{\pm}$), a heavy neutral CP-even state (H), and a neutral CP-odd state(A).

Since no supersymmetric particles have been found so far, supersymmetry has to be broken, if it exists. Within Gauge Mediated Supersymmetry Breaking (GMSB) models the breaking in a secluded sector is mediated via gauge interactions to the electroweak scale, such that the superpartners of the standard particles acquire additional masses.

The minimal GMSB model is characterised by six fundamental parameters. These are the effective SUSY breaking scale Λ, the mass scale of the messengers M_m, the number of messenger SU(5) supermultiplets N_5, the ratio of the Higgs vacuum expectation values $\tan\,\beta$, the sign of the higgsino mass term sign(μ) and the scale factor of the gravitino coupling C_{grav}, which determines the NLSP lifetime. Besides many other measurements, discovering signatures of GMSB and measuring the properties of the NLSP are among the physics goals of the ATLAS and CMS detectors [9]. GMSB models are a possibility to break SUSY on a low scale compared to generic mSUGRA models. A consequence is that the LSP is typically the gravitino which couples to the NLSP and its Standard Model partner.

The Standard Model and its minimal supersymmetric extension are briefly reviewed in Chapter 2 “Theoretical Foundation”. One of the main goals of the CMS detector at the Large Hadron Collider of CERN, a proton-proton collider with a nominal centre-of-mass energy of $\sqrt{s} = 14$ TeV, is to search for new physics Beyond the Standard Model. Chapter 3 “Experimental Setup” will introduce the Large Hadron Collider and the CMS detector. Chapter 4 “Physical Object Reconstruction” describe how to reconstruct the physical object,muons, electrons, and jets, with the CMS detector. The description of simulated Monte Carlo event samples used in this analysis is given in Chapter 5 “Data and Simulation”. The selection of the supersymmetric signal using the multilepton signature is discussed, and introduce how to predict background from the Standard Model by using data-driven method in Chapter 6 “Background Estimation”. Chapter 7 “Results of the Search” present the discovery prospects of CMS for a discovery of Supersimmetric Higgs events with multilepton search analysis. Chapter 8 “Conclusion”

Chapter 2

Theoretical Foundation

A theoretical overview followed by successful explanation of the results of experimental particle physics with the ways as a complete theory. And, we present the theory of supersymmetry, which is one of the several postulated theories that might lie behind the Standard Model, the search for the supersymmetry is the basis of this study.

2.1 The Standard Model

2.1.1 Elementary particles and interactions

The standard model attempts to explain all the phenomena of physics in terms of the properties and interactions of elementary particles of three types. The first two types are called *leptons* and *quarks* and are fermions with spin $-\frac{1}{2}$; the third is a set of spin -1 bosons, which are called *gauge bosons*, act as 'force carriers' in the theory of Standard Model. In the standard model, these particles are treated as point particles without internal structure or excited states, so they are assumed to be elementary.

The electron is the most familiar example of a lepton, that is bound in atoms by the *electromagnetic interaction*, which is one of the four fundamental forces of nature. Another example is the neutrino, a light and neutral particle, which is observed in the decay products of some unstable nuclei(β-decay). The force responsible for the β-decay of nuclei is called the *weak interaction*. In addition to leptons, There is another class of particles called *hadrons*, which is also observed in nature. The familiar examples of the hadrons are the neutron and proton, which are collectively called *nucleons*. In the standard model, these are made of quarks bound together by the third force of nature, the *strong interaction*, so considered to be elementary. It is unusual in the theory that the quarks themselves are not directly observable, only their bound states. The strong interactions , which are like nuclear forces binding nucleons into nuclei between quarks, also give rise to the observed strong interactions between hadrons. there is an analogy here with the fundamental electromagnetic interaction between electrons and nuclei which also gives rise to the more complicated forces between atoms(their bound states). In addition to the strong, weak and electromagnetic interactions between quarks and leptons, there is a fourth force of nature, *gravity*. However, the gravitational interaction between elementary particles is so small compared with the other three that we shall neglect in and refer to the 'three forces of nature'.

These forces are associated with elementary spin-1 bosons, the gauge bosons or force carriers like the electromagnetic interaction. In classical physics, the interaction between two charged particles is transmitted by electromagnetic waves, which are continuously absorbed and emitted. This is an natural description at long distances, but the quantum nature of the interaction must be taken into account at short distances. These are the force carriers, spin-1 *photons*, of the electromagnetic interaction, and as we shall see presently, the long-range nature of the force is related to the fact that the photons have zero mass.

The weak and strong interactions are also associated with the exchange of spin-1 particles. They are very massive, called W and Z bosons for the weak interaction. the resulting force is short range, and in many applications may be approximated by an interaction at a point. The equivalent particles for the strong interactions are massless like the photon and called *gluons*. Thus, the basic strong interaction between quarks is long range by analogy with electromagnetism. However, the residual strong interaction between the quark bound states, hadrons, is short range.

The leptons and quarks are the main actors, which are the basic constitutions of matter, and the 'force carriers'(the photon, the W and Z bosons, and the gluons) which mediate the interactions between them in the standard model. In addition, the quark bound states(i.e. hadrons) will also play a very important role, because not all these particles are directly observable.

The standard model(SM) is the theory of physics[10] [11] [12] that currently best describes the behavior of elementary particles. It is a Quantum Field Theory (QFT) [13] [14] built on symmetry principles: it includes the QFT of the electroweak interaction(Glashow-Weinberg-Salam model, GWS) and of the strong interaction(Quantum Chromo Dynamics, QCD). The important issue of the theory is the Electroweak Symmetry Breaking(EWSB) via the Higgs mechanism. That gives rise to the mass of the vector bosons and predicts the existence of the Higgs boson. Three out of four of the fundamental forces are described by the theory, that is the strong, the weak and the electromagnetic(EM) force. The gravitational interaction it is not relevant at the scales of mass and distance typical as in particle physics, so that is not taken into account.

The standard model describes matter as being composed of twelve elementary particles, the fermions with spin 1/2. The fermions can be divided into two main groups, leptons and quarks, and three families, as in the following table.

Fermions	1st family	2nd family	3rd family	Interactions
Quarks(2/3)	u	c	t	All
Quarks(-1/2)	d	s	b	All
Leptons(0)	ν_e	ν_μ	ν_τ	Weak
Leptons(-1)	e	μ	τ	Weak, EM

TABLE 2.1: Quarks and leptons

The interactions between particles are described in terms of exchange of vector bosons with spin 1, which are carriers of the fundamental interactions:

Interactions	Boson	Range[cm]
EM	Photon(γ)	∞
Weak	$W^{\pm}$, Z	10^{-16}
Strong	Gluons(g)	10^{-13}

TABLE 2.2: Interactions

Each particle is the quantum associated to an elementary field $\Phi_i(x)$ in the Minkowski space. The standard model is built around relativistic invariance. The fields and the associated particles are classified depending on how they transform under a Lorentz transformation, the Lagrangian of the theory is constructed using the possible scalar combinations of the fields. Since the others are irrelevant in the QFT, that is up to terms of dimension 4 in mass.

The theory is required to be locally invariant under transformations of the Lie group:

$$SU(3)_C \times SU(2)_L \times U(1)_Y \tag{2.1}$$

This kind of theory is called gauge theory. This requirement gives rise to the vector boson fields $V_i(x)$. The Lagrangian of standard model can be divided into three parts, the bosonic, the fermionic and the Yukawa sectors:

$$L_{SM} = L_B + L_F + L_Y \tag{2.2}$$

It contains the description of elementary interactions in terms of a quantum theory. The transition probabilities between quantum states can be calculated from elementary assumptions. The most important predictable quantities are basically cross sections and decay rates in subnuclear processes.

2.1.2 The bosonic sector

The bosonic sector is on the electroweak symmetry breaking and the Higgs mechanism. The sector is built around the complex scalar field, that has two components, and so four degrees of freedom:

$$\phi = \begin{pmatrix} \phi^1 \\ \phi^2 \end{pmatrix} \tag{2.3}$$

which is required to be locally invariant under the transformations of the Lie group:

$$SU(2)_L \times U(1)_Y \ni \Omega = e^{ig\alpha_a t^a} = e^{(ig_L \alpha_{Lb} T^b + ig_Y \alpha_Y Y)} \tag{2.4}$$

This group has four generators $(t^a)_{a=1,2,3,4}$: $(T^b)_{b=1;2;3}$ for $SU(2)_L$ and Y for $U(1)_Y$, and acts on the field ϕ:

$$\phi' = \Omega\phi \tag{2.5}$$

The group 2.4 is not simple, having two invariant subgroups $SU(2)_L$ (L stands for "left") and $U(1)_Y$ (Y stands for "hypercharge"). Thereby the corresponding QFT has two coupling constants g_L and g_Y , which are free parameters of the theory. The scalar field ϕ is a doublet of $SU(2)_L$ and has hypercharge 1/2. Composed of Lorentz and gauge invariant terms, the bosonic part of L_{SM} can be written as 2.6.

$$L_B = D^\mu \phi^\dagger D_\mu \phi - \mu^2 \phi^\dagger \phi - \lambda(\phi^\dagger \phi)^2 - \frac{1}{4} F_{a\mu\nu} F_a^{\mu\nu} \tag{2.6}$$

where D_μ is the covariant derivative, containing the gauge fields $A_\mu^a (= W^b, B)$:

$$D_\mu = \partial_\mu + ig_L T_b W_\mu^b + ig_Y Y B_\mu \tag{2.7}$$

$F_{a\mu\nu}$ is the tensor:

$$F_{a\mu\nu} = \partial_\mu A_{a\nu} - \partial_\nu A_{a\mu} - g f_a^{bc} A_{b\mu} A_{c\nu} \tag{2.8}$$

and f_a^{bc} are the structure constants of the group. No mass terms are present in the Lagrangian, and all the fields (ϕ and A_μ^a) are massless so far. The potential

$$V(\phi^\dagger \phi) = \lambda(\phi^\dagger \phi)^2 + \mu^2 \phi^\dagger \phi \tag{2.9}$$

can have different properties depending on the values of its parameters, μ^2 and λ. λ must be positive in order to have a physical potential that grows asymptotically with fields, while μ can be either positive or negative, leading to two different scenarios:

- $\mu^2 > 0$: all the bosonic fields are massless, the scalar field is quantized around the unique minimum of potential, that has the symmetry properties of the Lagrangian
- $\mu^2 < 0$: the potential has infinite minima for each field configuration satisfying

  $$(\phi^1)^2 + (\phi^2)^2 = -\frac{\mu^2}{\lambda} = v^2 \tag{2.10}$$

  the scalar field can be quantized around an arbitrary minimum. And that does not conserve the symmetry properties of the Lagrangian anymore. The typical choice for the minimum is

  $$\langle \phi \rangle = \frac{1}{\sqrt{2}} \begin{pmatrix} 0 \\ v \end{pmatrix} \tag{2.11}$$

  The symmetry is spontaneously broken, meaning that the Lagrangian keeps the symmetry properties while the vacuum state does not. The spontaneous symmetry breaking leaves a residual $U(1)$ symmetry still evident, called the electromagnetic symmetry group $U_{em}(1)$

The standard model has a spontaneously broken symmetry as observed experimentally, so $\mu^2 < 0$. The original symmetry $SU_L(2) \times U_Y(1)$ breaks down to $U_{em}(1)$:

$$SU_L(2) \times U_Y(1) \rightarrow U_{em}(1) \tag{2.12}$$

Three out of four Lie group dimensions are no more evident. The generator of the $U_{em}(1)$ symmetry group, called electromagnetic charge Q, is linked to the hypercharge group generator Y and to the third generator of $SU_L(2)$, T_3 by:

$$Q = Y + T_3 \tag{2.13}$$

The kinetic term of 2.6, evaluated at the minimum 2.11, yields these relevant terms:

$$L_{mass} = \frac{1}{\sqrt{2}} \begin{pmatrix} 0 & v \end{pmatrix} (g_L T_b W^b_\mu + g_Y Y B_\mu)(g_L T^b W^\mu_b + g_Y Y B^\mu) \begin{pmatrix} 0 \\ v \end{pmatrix} \tag{2.14}$$

Using the explicit form of the $SU_L(2) \times U_Y(1)$ generators, in the doublet representation:

$$T_b = \frac{\sigma^b}{2}, Y = \frac{1}{2} \tag{2.15}$$

where σ^b are the Pauli matrices, we can evaluate the matrix products explicitly:

$$L_{mass} = \frac{v^2}{8}[g_L^2(W^1_\mu)^2 + g_L^2(W^2_\mu)^2 + (-g_L^2 W^3_\mu + g_Y B_\mu)^2] \tag{2.16}$$

As we can read from 2.16 (the quadratic terms in the Lagrangian are mass terms), three combinations of the fields A^a_μ acquire mass. They are the boson carriers of the weak interaction:

$$W^\pm_\mu = \frac{W^1_\mu \mp iW^2_\mu}{\sqrt{2}}, \tag{2.17}$$

where mass $m_W = \sqrt{-\frac{\mu^2}{8\lambda} g_L}$, and

$$Z_\mu = cos\theta_W W^3_\mu - sin\theta_W B_\mu \tag{2.18}$$

where mass $m_Z = \sqrt{-\frac{\mu^2}{8\lambda}(g_L^2 + g_Y^2)^2}$, θ_W is the so called Weinberg angle, related to the coupling constants (and experimentally measured):

$$tan\theta_W = \frac{g_Y}{g_L} \simeq 0.24rad \tag{2.19}$$

The fields $W^\pm$ and Z gain a degree of freedom, after the spontaneous symmetry breaking, "eating" a component of the scalar field ϕ: this process is known as the "Higgs mechanism". The fourth combination of the fields A^a_μ, associated to the $U_{em}(1)$ group, keeps two degrees of freedom and remains massless. It is the photon:

$$A_\mu = sin\theta_W W_\mu^3 + cos\theta_W B_\mu \tag{2.20}$$

The fourth real component of the field ϕ remains free after the spontaneous symmetry breaking. It is therefore a free field with an associated particle that, after the spontaneous symmetry breaking, acquires mass: the Higgs boson H. To investigate this question we can work in the unitarity gauge, parameterizing the field ϕ as follows:

$$\phi = \frac{1}{\sqrt{2}} \begin{pmatrix} 0 \\ v + h(x) \end{pmatrix} \tag{2.21}$$

where $h(x)$ is a real scalar field, with null expectation value on vacuum. This parametrization makes explicit that ϕ has one degree of freedom after the symmetry breaking. The term containing the potential, in 2.6, takes the form:

$$V(h) = -\mu^2 h^2 + sqrt{-}\mu^2 \lambda h^3 + \frac{1}{4}\lambda h^4 \tag{2.22}$$

The Higgs boson is the particle associated with the field $h(x)$, with mass:

$$m_H = \sqrt{-2\mu^2} \tag{2.23}$$

The expansion of the kinetic energy term in 2.6, in unitarity gauge, yields the terms 2.16, that contain the masses, plus additional terms involving the coupling between vector bosons and the Higgs field h:

$$L_K = \frac{1}{2}(\partial_\mu h)^2 + \left[m_W^2 W_\mu^+ W_\mu^- + \frac{1}{2} m_Z^2 Z_\mu Z_\mu \right] \left(1 + \frac{h}{v}\right)^2 \tag{2.24}$$

The couplings of the Higgs particle to the gauge vector bosons are proportional to the squared masses of the bosons.

The bosonic sector of the SM has four parameters: the two coupling constants g_L and g_Y , and the potential parameters μ and λ. A summary table of the SM bosons and their masses, as functions of L_B parameters is [15]:

The parameters can be combined to form other four constants more easily measured by the experiments. Conventionally the four parameters of L_B are expressed using:

- The EM fine-structure constant (at low energy): $\alpha_{EM} = \frac{1}{137.035999679(94)}$

- The Fermi constant : $G_F = 1.1663787(6) \times 10^{-5} GeV^{-2}$
- The Z boson mass : $m_Z = 91.1876(21) GeV/c^2$
- The Higgs boson mass : unknown

2.1.3 The fermionic sector

The fermionic fields of the SM are Dirac four-component fields ψ_i. The chirality operator acts on the fields and divides them in left-handed and right-handed components:

$$\psi_{L,R} = \frac{1 \mp \gamma_5}{2} \psi, \psi = \psi_L + \psi_R \tag{2.25}$$

Depending on their chirality, the fields transform differently under transformations of the $SU_L(2) \times U_Y(1)$ group. The left-handed components of fields of leptons (l_L) and quarks (q_L) of the three families are grouped into doublets of $SU_L(2)$:

$$\begin{pmatrix} \nu_{eL} \\ e_L \end{pmatrix}, \begin{pmatrix} \nu_{\mu L} \\ \mu_L \end{pmatrix}, \begin{pmatrix} \nu_{\tau L} \\ \tau_L \end{pmatrix}, \begin{pmatrix} u_L \\ d_L \end{pmatrix}, \begin{pmatrix} c_L \\ s_L \end{pmatrix}, \begin{pmatrix} t_L \\ b_L \end{pmatrix} \tag{2.26}$$

The right-handed fields (l_R, q_R) are singlets of $SU_L(2)$, and do not transform under its action. Right-handed neutrinos are not included in the theory. Both right-handed and left-handed fields transform under the hypercharge group $U_Y(1)$. They carry both Y and T_3 charges. The following table summarizes charges of leptons l and quarks q:

The fermionic Lagrangian can be written (the sum over families is tacit):

$$\begin{aligned} L'_F \quad = \quad & i\bar{l}_L \gamma^\mu (\partial_\mu + i g_L \tfrac{\sigma^b}{2} W_{b\mu} + i g_Y (-\tfrac{1}{2}) B_\mu) l_L \\ & + i\bar{l}_R \gamma^\mu (\partial_\mu + i g_Y (-1) B_\mu) l_R \\ & + i\bar{q}_L \gamma^\mu (\partial_\mu + i g_L \tfrac{\sigma^b}{2} W_{b\mu} + i g_Y (\tfrac{1}{6}) B_\mu) q_L \\ & + i\bar{q}^u_R \gamma^\mu (\partial_\mu + i g_Y \tfrac{2}{3} B_\mu) q^u_R + i\bar{q}^d_R \gamma^\mu (\partial_\mu + i g_Y (-\tfrac{1}{3}) B_\mu) q^d_R \end{aligned} \tag{2.27}$$

Boson	mass^2	measured mass [GeV/c^2]
W$^\pm$	$-\frac{\mu^2 g_L^2}{8\lambda}$	80.385 ± 0.015
Z	$-\frac{\mu^2 (g_L^2 + g_Y^2)}{8\lambda}$	91.1876 ± 0.0021
A	0	0 ($< 10^{-26}$)
H	$-\mu^2$	unknown

TABLE 2.3: SM bosons and their masses

This Lagrangian contains couplings between fermions and vector bosons. Consequently, after the electroweak spontaneous symmetry breaking, the coupling terms between fermions and massive bosons $W^{\pm}, Z$ and A are:

- the electromagnetic interaction term:

$$L_{em} = -eA_{\mu}j^{\mu}_{em} \ , \ j^{\mu}_{em} = -\bar{l}\gamma^{\mu}l + \frac{2}{3}\bar{q}^{u}\gamma^{\mu}q^{u} - \frac{1}{3}\bar{q}^{d}\gamma^{\mu}q^{d} \tag{2.28}$$

- the weak neutral-current interaction term:

$$L_Z = -\sqrt{g_L^2 + g_Y^2}Z_{\mu}j^{\mu}_{Z} \ , \ j^{\mu}_{Z} = \bar{l}_L\gamma^{\mu}\frac{\sigma^3}{2}l_L + \bar{q}_L\gamma^{\mu}\frac{\sigma^3}{2}q_L - sin\theta_W j^{\mu}_{em} \tag{2.29}$$

- the weak charged-current interaction term:

$$L_W = -\frac{g_L}{\sqrt{2}}(W^{+}_{\mu}j^{\mu-} + h.c.) \ , \ j^{u-}_{W} = \bar{\nu}_L\gamma^{\mu}l_L + \bar{q}^{u}_{L}\gamma^{\mu}q^{d}_{L} \tag{2.30}$$

No new parameters are introduced in formula 2.27: the couplings between fermions and vector bosons depend on the 4 parameters of the bosonic sector of the SM. Note that no mass terms for fermions like $m(\bar{\psi_L}\psi_R + \bar{\psi_R}\psi_L)$ are permitted, since they would explicitly break the gauge symmetry: the right-handed and left-handed fermions belong to different $SU_L(2)$ representations and have different $U(1)$ charges: the fermions are massless in L'_F.

The QCD is introduced in the SM, postulating the $SU_c(3)$ local gauge invariance for the quark fields. The $SU_c(3)$ Lie group has 8 generators, each giving rise to a correspondent massless gluon field. The QCD Lagrangian can be written in a very compact way as:

$$L_{QCD} = \bar{\psi}_q(i\gamma^{\mu}D_{\mu})\psi_q - \frac{1}{4}G^{a}_{\mu\nu}G^{\mu\nu}_{a} \tag{2.31}$$

Field	Y	T_3	Q
ν_L	-1/2	1/2	0
l_L	-1/2	-1/2	-1
l_R	-1	0	-1
q^u_L	1/6	1/2	2/3
q^d_L	1/6	-1/2	-1/3
q^u_R	2/3	0	2/3
q^d_R	-1/3	0	-1/3

Table 2.4: Charges of leptons and quarks

where D_μ is the covariant derivative, containing the 8 gluon gauge fields $(g^a_\mu)_{a=1,\ldots,8}$

$$D_\mu = \partial_\mu + ig_{QCD} G_a g^a_\mu \tag{2.32}$$

$G_{\mu\nu}$ is the tensor:

$$G_{a\mu\nu} - \partial_\mu g_{a\nu} - \partial_\nu g_{a\mu} - g_{QCD} f^{bd}_a g_{b\mu} g_{c\nu} \tag{2.33}$$

and f^{bc}_a are the structure constants of the group. The L_{QCD} charge is the so called color: each quark can express itself in three possible colors, the color index is tacit in formula 2.31. The QCD is an asymptotically free theory, meaning that the running coupling constant $g_{QCD}(Q^2)$ becomes small in high energy-transfer processes: in QCD, a perturbative calculation of cross sections is possible only at high energy-transfer.

Adding the QCD Lagrangian, the formula for the fermionic sector of the SM is:

$$L_F = L'_F + L_{QCD} \tag{2.34}$$

2.1.4 The Yukawa sector

It is possible to write another term in the SM Lagrangian, which satisfies all the postulated symmetries. Thanks to this term, the masses of fermions are introduced in the SM. It is a sum of Yukawa-interaction terms that couple the fermions to the scalar field ϕ:

$$L_Y = -\sum_{i,j \in families} \left(\bar{l}_{IR}(g_L)_{ij}\phi^\dagger \begin{pmatrix} \nu_{iL} \\ l_{iL} \end{pmatrix} + \bar{d}_{iR}(g_d)_{ij}\phi^\dagger \begin{pmatrix} u_{jL} \\ d_{jL} \end{pmatrix} + \bar{u}_{iR}(g_u)_{ij}\tilde{\phi}^\dagger \begin{pmatrix} u_{iL} \\ d_{iL} \end{pmatrix} \right) + h.c. \tag{2.35}$$

where $\tilde{\phi} = i \begin{pmatrix} 0 & 1 \\ -1 & 0 \end{pmatrix} \phi^*$ is the scalar doublet with hypercharge -1/2.

The Yukawa matrices $(g_f)_{ij}$ are diagonalized by bi-unitary transformations:

$$(g_f)^{diag}_{ij} = U^\dagger_f (g_f)_{ij} V_f, \begin{cases} f_L \to V_f f_L \\ f_R \to U_f f_R \end{cases} \tag{2.36}$$

where V_f and U_f are unitary matrices. The 9 eigenvalues of $[(g_f)_{ij}]_{f \in fermions}$ are in one-to-one correspondence with fermion masses.

When the transformation 2.36 is inserted in 2.27, it gives rise, in the charged current terms, to a non-vanishing unitary matrix that mixes the families in the weak charged-current interactions, the CKM matrix:

$$V_{CKM} = V_u^\dagger V_d \tag{2.37}$$

This matrix describes the mixing of families in charged-current processes, so a down-like quark of a family can turn in an up-like quark of another family emitting a W boson, and vice-versa. The CKM matrix contains other 4 physical parameters: 3 “angles” and a “phase”, which is responsible for the CP violation in some SM processes.

In formula 2.35, we can read the couplings of the Higgs boson to the SM fermions:

$$L_{Hf} = -m_f \bar{f} f \left(1 + \frac{h}{v}\right) \tag{2.38}$$

Each coupling is proportional the corresponding fermion mass.

In total, the L_Y term of the SM Lagrangian has 13 free parameters: the 9 Yukawa coupling constants which are in one-to-one correspondence with fermion masses, and the 4 CKM matrix parameters. The SM lets the masses of fermions have different values, since they are free parameters of the theory, but it does not explain why they are so different, spanning 6 orders of magnitude, from 0.5 MeV/c^2 for the electron to about 173 GeV/c^2 for the top quark. This fact is known as the avor problem.

2.2 Beyond the Standard Model

The standard model gives the great success in explaining the wide experimental results. In spite of that sucess, we know that it cannot be the ultimate description of the universe. At first, it only describes three of the four known forces, but gravity. Thus the standard model is not a theory of everything. That model can be considered to be ad-hoc and inelegant, since the values of its 19 numerical constants are mostly unrelated and arbitrary. And there is no explanation as to why there should be three generations of particles.

The most well-known theoretical objection to the standard model is the hierarchy problem, which is from the weak force is so much stronger than gravity. The weak force depends on Fermis constant($G_F = 1/(\sqrt{2}v^2) \sim 10^{-5}GeV^{-2}$), and gravity depends on Newtons constant ($\sim 10^{-38}GeV^{-2}$). Quantum corrections to Fermis constant, calculated using the standard model, would make it closer to Newtons constant. And the only way around this is if there is a delicate cancellation between the bare value of Fermis constant and the quantum corrections to it, referred to as fine-tuning, an unpleasant feature of any theory. Another way to think about the hierarchy problem is via the Higgs mass (m_H). The Higgs mass receives large quantum corrections that are related to the scale up to which the standard model holds. The two common scales at which the standard model is expected to break down are the Planck scale and the grand unification theory (GUT) scale. The Planck scale(10^{19} GeV) is the scale at which the quantum effects of gravity are expected to be large. The GUT scale is the scale at which the electromagnetic, weak, and strong forces can be described as a unified force. This depends on the nature of the GUT, but it is typically about $10^{16}GeV$. In the absence of new physics between one of these scales and the electroweak scale(100 GeV), the corrections to the Higgs mass are many orders of magnitude larger than its actual mass. In order to keep the Higgs mass at the electroweak scale, the bare mass of the Higgs has to be fine-tuned.

Additionally, there are several experimental observations which the SM cannot account for. From several neutrino experiments, we know that neutrinos can oscillate from one flavor to another. This can only be explained if neutrinos have non-zero mass, inconsistent with the current SM formulation. From cosmological measurements, we know that ordinary baryonic matter can only account for about 4% of the energy density of the universe, the rest coming from dark matter (about 23%) and dark energy (about 73%). The existence of dark matter is inferred solely through its gravitational interactions with other matter. It is incapable of electromagnetic interactions, and therefore not observable through telescopes (*dark matter*). There is no particle in the SM that is a viable dark matter candidate. Dark energy is a hypothetical form of energy that permeates all space, and accelerates the expansion of the universe, and beyond the scope of the SM. The SM is unable to explain the matter-antimatter asymmetry of the current universe: if there were equal amounts of matter and antimatter after the Big Bang, then why is the observable universe mostly made of the matter i.e. where did the antimatter go? The SM is also unable to account for the strong CP problem, which can be stated as: why does QCD not violate the CP symmetry? In electroweak theory, gauge fields couple to chiral currents constructed from fermionic fields, whereas gluons couple to vector currents. Experiments do not indicate any CP violation in the QCD sector, the strongest constraint coming from the dipole moment of the neutron. There are natural terms in the QCD Lagrangian that are able to break the CP symmetry, and the only way to avoid that is through fine-tuning.

The scattering amplitude of longitudinally polarized W bosons at tree level grows as s, where s is the center of mass energy squared. This growth continues until the mass of the Higgs is reached, and thereafter it stays constant at a value proportional to m_H^2. Thus, for unitarity to not be violated, there must be an upper bound on m_H^2, which implies that the Higgs should appear below the TeV scale. The discovery of the Higgs at 125 GeV eliminates this problem.

Some examples of new physics that we may see at the LHC include supersymmetry, extra dimensions, hidden valley theories, or new gauge bosons. These new physics models address one or more shortcomings of the SM, and often predict the existence of particles beyond those postulated in the SM.

2.2.1 Hierarchy problem

In theory, the mass of a Higgs could be unstable if it is not fine tuned. The Higgs mass m_H has two contributions: the fundamental bare mass parameter m_0 and radiative boson corrections, in this example the W boson (the largest fermionic correction is from top loops).

$$m_H^2 = m_0^2 + \delta m_W^2 \tag{2.39}$$

The bare mass is not that which is measured in experiment. The corrections depend on the cutoff scale λ and the boson mass.

$$\delta m_W^2 \sim -g_W^2 \int_{\lambda_0}^{\lambda} \frac{d^4k}{k^2} \sim -g_W^2(\lambda^2 + m_W^2) \tag{2.40}$$

Using the Planck scale, $\lambda \sim M_{Pl}$, one gets a correction of order of 10^{36} GeV^2. Thus the mass parameter must be of the same order of magnitude to cancel this effect. To get a Higgs mass of the order of 100 GeV this cancellation must be accurate for 32 orders of magnitude. One may consider such fine tuning unnatural, although nature does not forbid it.

Consider the calculation of the electron mass as an example [16]. Let us assume there is no positron, and still we may perform the computation. The number turns out to be about 10 GeV, which is much larger than the mass of electron. This is, strictly speaking, not necessarily considered wrong, because the bare mass of electron is unknown any way, and instead the bare mass has to be fine tuned. However, one may introduce an antiparticle of electron and then the tuning becomes unnecessary, because electron and positron contributions are roughly canceled out due to the underlying chiral symmetry.

If there were fermions with roughly the same characteristics of the bosons, additional fermionic loops would be added.

$$m_H^2 = m_0^2 + \delta m_W^2 + \delta_{\tilde{W}}^2 \tag{2.41}$$

These loops stabilize the value of m_H as they introduce an opposite sign (bosonic loops do not bring a minus sign but fermionic ones do).

$$\delta m_{\tilde{W}^2} \sim +g_{\tilde{W}}^2 \int_{\lambda_0}^{\lambda} \frac{d^4k}{k^2} \sim +g_{\tilde{W}}^2(\lambda^2 + m_{\tilde{W}}^2) \tag{2.42}$$

This works only if $g_W^2 = g_{\tilde{W}}$ and $m_W^2 = m_{\tilde{W}}^2$. Otherwise fine tuning is still needed although it becomes less severe if $g_W^2 \sim g_{\tilde{W}}$ and $m_W^2 \sim m_{\tilde{W}}^2$, and it is called little hierarchy problem. To understand this, we can again check the masses of electron and positron, which are identical.

2.2.2 Supersymmetry

Most fundamental symmetries are already used in the SM. However, there is one symmetry missing in the SM, which is a symmetry between fermions and bosons. In the SM, the role assignment for fermions and bosons is fixed: bosons are force carriers, and fermions are matter content. If the symmetry between fermions and bosons is introduced, hierarchy problem goes away as explained in the previous section. By assuming such a symmetry exists at TeV scale, this is good news for experimentalists as it doubles the number of particles in the SM. Strictly speaking, the doubling is not exact, although sometimes it is said a mirror copy of the SM is created once SUperSYmmetry (SUSY) is introduced. One of complexities comes from electroweak symmetry breaking, which mixes B and W fields so that the weak bosons and photon can be realized as they are measured in experiments. There is, in general, no need to form a supersymmetric copy of photon for example. Instead, Bino and Winos are introduced before electroweak symmetry breaking. Another complexity comes from the structure of Higgs doublet.

With these exceptions in mind, for each SM particle, one new particle with exactly the same attributes is introduced by changing its spin by a half unit. Mathematically, there is an operator Qwhich transforms fermions to bosons and vice versa. Such operations must be anticommuting spinors carrying spin half, and thus supersymmetry is a space-time symmetry. For a realistic theory involving chiral fermions, the Haag-Lopuszanski-Sohnius extension of the Coleman- Mandula theorem requires the following relations on the operator Q [36] and [37].

$$\{Q, Q^{\dagger}\} = p^{\mu} \tag{2.43}$$

$$\{Q, Q\} = \{Q^{\dagger}, Q^{\dagger}\} = 0 \tag{2.44}$$

$$[P^{\mu}, Q] = [P^{\mu}, Q^{\dagger}] = 0 \tag{2.45}$$

where P is the generator of space-time translation.

One aspect of this algebra is that supermultiplets in which the particle states are grouped. As Q and $Q^{\dagger}$ commute with most symmetry transformations all states in one supermultiplet possess equal masses and quantum numbers with the exception of spin. The common mass within each supermultiplet is realized when the symmetry is intact. Once the symmetry is broken, there is no longer the common mass (*e.g.*, electron mass is different from the supersymmetric partner of electron). Each of these supermultiplets contains equal numbers of bosonic and fermionic degrees of freedom, as a natural result of the symmetry between fermion and boson as desired.

Let us construct simple supermultiplets starting with spin-0. The simplest one contains one spin-1/2 fermion and two scalars (spin-1/2 fermion has up and down states). The next simplest one contains one spin-1 boson, which ought to be massless to be renormalizable (3-1 = 2 states), and a massless spin-1/2 fermion. Finally there is a particle for each the SM particle, effectively doubling the number of particles. The last one contains a spin-2 graviton (5-1 = 4 states) and one spin-3/2 fermion (4 states).

The Higgs sector needs special care. If one assumes only one Higgs, gauge anomalies appear in the electroweak gauge sector, spoiling the renormalizability of the theory. Additionally the supersymmetric Higgs mechanism gives mass only to fermions in one spin state. To solve these problems two doublets are needed, resulting in eight degrees of freedom as opposed to four in the SM. Only three out of eight are consumed by vector bosons upon SUSY breaking, leaving five Higgs bosons left. Each fermion in the SM is accompanied by a supersymmetric partner. The gauge boson counterparts are gauginos. As mentioned earlier, gauginos usually do not directly correspond to gauge bosons in the SM, rather these supersymmetric particles mix together with four higgsinos to form neutralinos and charginos. The eight gluons have eight gluinos.

By recalling the fact a supermultiplet has one common mass, unbroken SUSY theories do not fit reality. No sparticle has been observed yet. For example, a boson with the mass of the electron would be easily observed.

Therefore the symmetry must be broken, meaning sparticle masses are not equal to the masses of their corresponding particles (*e.g.*, selectron mass must be much higher than electron mass). The breaking is usually introduced by additional terms in Lagrangian, which parametrize the effects of SUSY breaking without actually explaining why it is broken. If this breaking is hard, all couplings and masses are to be freely chosen, and the hierarchy problem would most likely reappear. Consequently, the breaking must be soft so that couplings in broken and unbroken SUSY must be approximately equal.

Then the SUSY Lagrangian can be separated in two pieces: one contains the gauge and Yukawa interactions that preserve SUSY invariance, and another one contains the breaking terms.

$$L = L_{SUSY} + L_{SOFT} \tag{2.46}$$

These breaking terms may spoil the solution for the hierarchy problem, if the sparticle masses are too high. To avoid the fine tuning, sparticle masses are kept to O(TeV).

In unbroken SUSY all attributes are determined, thus there are no new free parameters besides the 19 of the SM. Breaking leads to more free parameters: in the MSSM there are 105 new parameters, eight in the gaugino-higgsino sector, 21 masses, 36 mixing angles and 40 CP violating phases in the squark-slepton sector. Some of these parameters are constrained by experiments. However, most of them remain as free parameters, which of course makes SUSY theories comparisons to experimental results difficult.

2.2.3 SUSY answers to the problems in the SM

For all the above mentioned problems SUSY provides solutions. One may assign a new multiplicative quantum number, R-parity to each particle: +1 for the SM particle, and -1 for sparticle. If R-parity is conserved, sparticles can only be produced or annihilated in pairs. Thus the Lightest SUSY Particle (LSP) is stable and may be identified as Cold Dark Matter if it is electrically neutral, weakly interacting, and massive.

The coefficients of running the couplings, with new particles, become with two SUSY Higgs doublets.

$$b_1 = 0 - 2N_F - \frac{3}{10}N_H \tag{2.47}$$

$$b_2 = 6 - 2N_F - \frac{1}{2}N_H \tag{2.48}$$

$$b_3 = 9 - 2N_F - 0 \tag{2.49}$$

Thus the evolution of the couplings will change leading to one common point at high energy. Above this energy the coupling stays the same. The unification of the couplings do not take place for arbitrary number of new particles. SUSY does provide the right number of new particles so that the unification occurs at higher energy scale.

Finally, bosonic and fermionic SUSY particles now appear in the higgs mass calculation, resulting a cancellation of the divergence so that Higgs mass becomes finite and its mass scale stabilizes.

2.2.4 Minimal supergravity

Let us recall the procedure for local gauge theories. Starting from a free Dirac equation, pick a symmetry to be imposed. Transform the Lagrangian under the symmetry, and finally restore the symmetry by introducing additional fields. The same has been done for SUSY by assuming super gravity fields breaks SUSY. In this context, the newly introduced fields are the spin-3/2 gravitino, and spin-2 graviton.

As mentioned in the previous section, SUSY must be softly broken. Now one may recall how the electroweak symmetry was broken. Essentially the same mechanism can be used here as well. In a locally broken SUSY, the gravitino absorbs the goldstino (which is a supersymmetry version of Numbu-Goldstone boson) and thus acquires its mass: much like the Higgsmechanism in the SM. Although the theory now includes gravity, it is still not a full quantum theory of gravity, as it is still not renormalizable.

To avoid gauge anomalies the breaking must take place in a hidden sector. Its effect must then be transmitted to the visible sector. This can either be done by gauge forces or by gravity, Gauge Mediated SUSY Breaking (GMSB), and SUperGRAvity (SUGRA), respectively. While MSSM is a low energy effective theory, including gravity allows to consider energy close to the Planck scale.

2.3 Simplified Models of SUSY

A model of new physics is defined by a TeV-scale effective Lagrangian describing its particle content and interactions. A simplified model is specifically designed to involve only a few new particles and interactions.[17] Many simplified models are limits of more general new physics scenarios, where all but a few particles are integrated out. Simplified models can equally well be described by a small number of parameters directly related to collider physics observables: particle masses (and their decay widths, which can sometimes be neglected), production cross-sections, and branching fractions. Simplified models are clearly not model-independent, but they do avoid some pitfalls of model-dependence. The sensitivity of any new-physics search to a few-parameter simplified model can be studied and presented as a function of these parameters and in particular over the full range of new particle masses. Though defined within a simplified model, these topology-based limits also apply to more general models giving rise to the same topologies.

Lepton simplified models described in this section populate final states with up to 4+ leptons with or without new sources of missing energy.

Multi-lepton signatures arise most commonly in cascade decay scenarios. SUSY type with neutralino or squark decays giving W or Z bosons, multi-leptons from R-parity violation, tri-leptons from scalar diquarks,

Low scale gauge-mediated supersymmetry breaking naturally gives rise to superpartner spectra with nearly degenerate right-handed sleptons playing the role of co-next to lightest superpartner (co-NLSP), with a bino-like neutralino as the next to next to lightest superpartner (NNLSP) [18]. [19] [20] [21] [22] [23] [24]

For spectra of this type, cascade decays from heavier superpartners always pass sequentially through the bino, then to one of the co-NLSP sleptons emitting a lepton, and finally to the un-observed Goldstino, emitting another lepton. Therefore, pair-production of heavier superpartners gives rise to inclusive signatures that include four hard leptons and missing transverse energy, $pp \to l^+ l^- l'^+ l'^- + \not{E}_T$ This signature is best covered by an exclusive hierarchical search for quad-leptons, tri-leptons, and same-sign dileptons, including $\not{E}_T$ in the latter two cases as necessitated by backgrounds. The principal strong production channels that are relevant for early LHC searches are pairs of gluinos and/or squarks. Weak production of chargino, neutralinos, and direct production of sleptons will become relevant in future searches. A reach or upper limit on $\sigma \times$ BR for $pp \to multi - leptons + \not{E}_T$ as a function of the gluino and the chargino masses provides a unified summary of the sensitivity to this topology for both strong and weak production of superpartners.

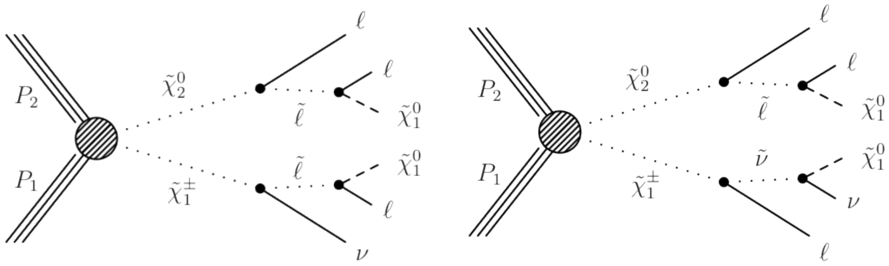

FIGURE 2.1: The simplified model with neutralino-neutralino(chargino) decay to three or four leptons via intermediate slepton(left) or intermediated sneutrino

Multileptons can result from pair-production of electroweakly charged objects that frequently occur in BSM theories as partners of electroweak and Higgs bosons (i.e., MSSM, NMSSM, UED, and some Little Higgs models). This simplified model consists of an electrically charged particle accompanied by two neutral particles, the lighter of which is stable. In particular, the particles have the quantum numbers of the lightest two neutralinos and the lightest chargino. The new particles are produced via Standard Model vector bosons. Several of the production modes and decay spectra result in multilepton topologies [25] [26] [27] [28] [29] [30]

In simplified models [31], a limited set of hypothetical particles and decay chains are introduced to produce a given topological signature. The amplitudes describing the production and decays of these particles are parametrized in terms of the particle masses and their branching ratios to daughter particles. Simplified models provide a benchmark for comparing search strategies which is more sensitive to the choice of kinematic selections and the final state topology than CMSSM. Furthermore, the presentation of signal acceptance and cross section upper limits as a function of the mass parameters of a simplified model can be used as a reference to place limits on different theoretical models.

The simplified model with neutralino-neutralino(chargino) decay to multi-leptons is shown in Fig. 2.1. The production mode involves slepton-slepton($\tilde{l}$) or slepton-sneutrino($\tilde{\nu}$), which decay into massive neutralino LSP($\tilde{\chi}^0$). Neutralino-chargino decays directly to result in our desired multilepton final state.

2.4 The Gauge Mediated Supersymmetry Breaking

As mentioned before section, breaking of the supersymmetry must be soft. However this does not mean it must be broken by the gravitino field. A different way to break the symmetry softly is via gauge interactions of the messenger particles which make the hidden sector communicate with the observable sector: Gauge Mediated Supersymmetry

Breaking (GMSB). The soft supersymmetry breaking masses of SUSY partners of SM particles are thus proportional to the strength of their gauge interactions while the gaugino masses satisfy the grand unification mass relations. The full mass spectrum and couplings are determined by six parameters within the simplest model of this type. The parameters are

- Λ, the effective SUSY breaking scale of sparticles
- M_m, the mass scale of the messengers
- N_5, the number of messenger $SU(5)$ supermultiplets
- $tan\beta$, the ratio of the Higgs field vacuum expectation values
- $sign(\mu)$, the sign of the common higgs mass parameter term
- C_{grav}, the scale factor of the gravitino coupling, partial width constant for sparticle decaying to gravitino, which determines the NLSP lifetime.

The most important parameter of the six is Λ which sets the scale of sparticles. The experimental signature of the model depends on the mass of the NLSP by assuming the LSP escapes from the detector without any footprint. This statement applies to any variant of the MSSM, for example, the mSUGRA as well.

One important difference from the mSUGRA is that the gravitino can be identified as the LSP. In such a case, the decay mode $\tilde{l}_1 \to l\tilde{G}$ can be dominant. This mode is indeed dominant if $m_{\tilde{l}_1} - m_{\tilde{\tau}_1} \leq m_\tau$ and produces electrons and muons copiously as staus are suppressed. Given that high reconstruction efficiencies and low fake rates of electrons and muons with respect to taus, this particular scenario is attractive. In this dissertation, a further simplification is done: the gluino mass fixed and the bino mass varied to scan the parameter space. The strong SUSY breaking scale is set separately from that of weak scale: squarks and gluinos can be much lighter than those sparticles in the mSUGRA. Lighter strongly interacting particles result higher production cross section. The slepton masses are taken to be degenerate within few GeV.

In this particular scenario, we have many leptons in a final state. This model is referred as Multi-Lepton co-NLSP (ML) or the Gauge Mediated Split Messenger (GMSM) model in the result table and exclusion limit plot. The details of the model can be found for instance in references [32] [33].

Since no supersymmetric particles have been found so far, supersymmetry has to be broken, if it exists. Within Gauge Mediated Supersymmetry Breaking (GMSB) models

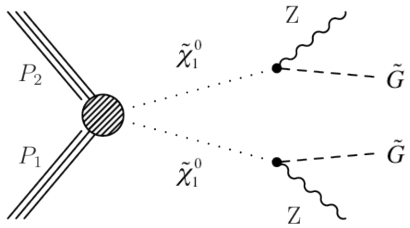

FIGURE 2.2: Higgsino GMSB model with chargino-chargino, neutralino-neutralino, chargino-neutralino production with large branching fraction to ZZ(W)+MET

the breaking in a secluded sector is mediated via gauge interactions to the electroweak scale, such that the superpartners of the standard particles aquire additional masses. If R-parity is assumed to be conserved, the lightest SUSY particle (LSP), which is the goldstino/gravitino, is stable. It is nearly massless, since its mass is proportional to the breaking scale, which usually lies well below the Planck scale. The next-to-lightest SUSY particle (NLSP) is often either the lightest neutralino or the lightest stau, which decay to the LSP and their standard model partners with a lifetime also depending on the breaking scale.

Besides many other measurements, discovering signatures of GMSB and measuring the properties of the NLSP are among the physics goals of the ATLAS and CMS detectors.

The last status of the Tevatron searches for GMSB is given in [34]. GMSB models are a possibility to break SUSY on a low scale compared to generic mSUGRA models. A consequence is that the LSP is typically the gravitino which couples to the NLSP and its Standard Model partner. Superpartners of SM particles are introduced into the theory based on the new symmetry [35]. It remains to be seen if SUSY is a true symmetry of nature.

As shown in Fig. 2.2, Higgsino GMSB model with chargino-chargino, neutralino-neutralino, chargino-neutralino production with large branching fraction to ZZ(W)+MET results in signature with three or four leptons and large missing energy from LSP(χ_1^0). The study in this dissertation is focused on GMSB Higgsino modelwith three or four leptons signatures in final state.

Chapter 3

Experimental Setup

This search for supersymmetry uses data collected from proton-proton collisions obtained at CERN, the worlds largest particle physics laboratory. The accelerator used to achieve these high-energy collisions is the Large Hadron Collider (LHC), and the experiment that detects the products of these collisions is the Compact Muon Solenoid (CMS). This chapter describes the CMS detector and data acquisition system. The discussion that is presented in this chapter can be found in greater detail elsewhere[JINST 0803], and the figures used here are taken from the same source.

3.1 The Large Hadron Collider

The LHC is a particle accelerator that is 27 km in diameter, located at a mean depth of 100 m underground. It is built in the same tunnel as the Large Electron-Positron Collider (the previous accelerator at CERN), the rock layers above providing a natural shielding from incoming (cosmic) and outgoing radiation. It is designed to provide head-on collisions of two proton beams, each at 7 TeV, with an instantaneous luminosity of 1034 cm2 s1. However, due to risks revealed in an accident that occurred on September 19, 2008, the peak energy cannot be reached till repairs have been performed during the long shutdown scheduled at the end of 2012. Hence, during the 2010 and 2011 runs, each proton beam was at 3.5 TeV.

The large center-of-mass energy and instantaneous luminosity place significant challenges on any detector associated with the LHC. The total proton-proton cross-section at $\sqrt{s} = 7$ TeV is roughly 70 mb. This implies inelastic collisions at $\sim 10^9$ Hz. The online event selection process (trigger) must reduce the rate dramatically to $\sim 10^2$ Hz for storage and offline analysis. The time between bunch crossings is a mere 50 ns, placing severe demands on the read-out and trigger systems. During the 2011 run, an average of 7 inelastic collisions were superimposed on the event of interest, referred to as pile-up. Pile-up can cause the products of the interaction being studied to be confused with those from other interactions. This problem is compounded when the response time of a detector element is longer than the interval between bunch crossings. The effect of pile-up can be reduced by using high-granularity detectors with good time resolution, resulting in low occupancy. This requires a large number of detector channels, which must be well-synchronized. The LHC is a high radiation environment, requiring radiation-hard detectors and front-end electronics. Finally, in order to achieve the ambitious physics goals of the LHC, a detector must be able to reconstruct physics objects efficiently, with very good resolution and low probability of mis-identification. The CMS detector, described in depth in the next section, is designed to successfully address these challenges.

3.2 The Compact Muon Solenoid Detector

The CMS detector is 21.6 m long, has a diameter of 14.6 m, and weighs 12.5 kt. Its layout can be seen in Fig. 3.1. A crucial component for the precise momentum measurement of high-energy charged particles is a magnet with a large bending power to deflect the charged particles from a straight line trajectory. This is achieved by a 13 m long, 6 m inner-diameter, 3.8 T superconducting solenoid which is at the heart of the CMS detector. The solenoid provides a bending power of 12 Tm before the muon bending angle is measured by the muon system (Sec. 3.2.4). The strong return field saturates the 1.5 m of iron that interleave the muon detectors. The bore of the magnet coil is large enough to accommodate within it the inner tracker (Sec. 3.2.1) and the calorimetry. The inner tracker consists of a silicon pixel detector and a silicon microstrip detector. The main calorimeters are the electromagnetic calorimeter (ECAL, Sec. 3.2.2) and the hadronic calorimeter (HCAL, Sec. 3.2.3). Additionally, CMS has the forward calorimeters, known as CASTOR and zero degree calorimeter (ZDC), but information from them is not used in this analysis.

The CMS coordinate system is centered at the nominal collision point inside the experiment, with the y axis pointing vertically upward, and the x axis pointing radially inward toward the center of the LHC. Thus, the z axis points along the beam direction. Coordinates in the detector are specified using the azimuth ϕ in the plane transverse to the beam direction and the pseudorapidity $\eta =$ ln $[\tan(\theta/2)]$, where θ is the polar angle relative to the beam axis. The region of the detector with $\mid \eta \mid< 1.5$ is referred to as

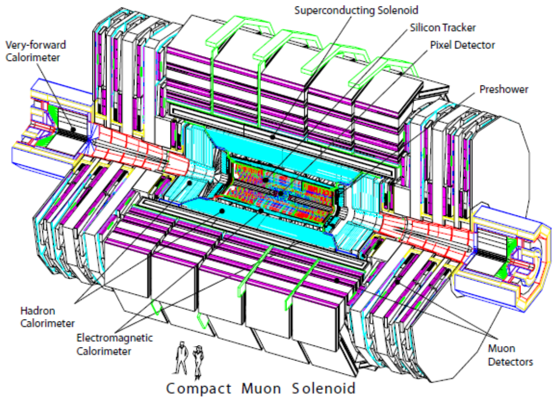

FIGURE 3.1: A perspective view of the CMS detector

the barrel, while the endcap has 1.5 $<|\ \eta\ |<$2.5. Transverse energy is defined as $E_T =$ E sin(θ), and transverse momentum p_T is defined analogously.

3.2.1 Inner tracking system

The inner tracker is used to reconstruct the trajectories of charged particles. It surrounds the interaction point, has a length of 5.8 m and a diameter of 2.5 m. Combined with the ECAL, it is used to identify electrons, and combined with the muon system, it is used for muon identification. It can precisely measure secondary vertices and impact parameters of charged particles, used to identify heavy flavor decays that are characteristic of many interesting physics processes. It satisfies stringent requirements on granularity, speed and radiation hardness by use of silicon detector technology. High granularity and speed imply a high power density of the on-detector electronics, which requires efficient cooling. This is in direct conflict with the aim to keep material budget to a minimum in order to limit multiple scattering, Bremsstrahlung, photon conversion and nuclear interactions. A compromise had to be found in this respect. Consequently, the inner tracker has a fast enough response to be a part of the software-based High Level Trigger, but not fast enough to be a part of the hardware-based Level 1 trigger system (Sec. 3.2.5). Figure 3.2 shows a schematic cross section through the CMS tracker. It is composed of a pixel detector with three barrel layers (BPIX) at radii between 4.4 cm and 10.2 cm and a silicon strip tracker with 10 barrel detection layers (Tracker Inner Barrel, TIB, Tracker Outer Barrel, TOB) extending outwards to a radius of 1.1 m. Each system is completed by endcaps which consist of 2 disks in the pixel detector (FPIX) and 3 plus 9 disks in the strip tracker (Tracker Inner Disk, TID, and Tracker endcap, TEC) on each side of the barrel, extending the acceptance of the tracker up to $|\ \eta\ |<$ 2.5. The pixel detector is designed to precisely measure the impact parameter of charged particles and the position of secondary vertices, and to achieve similar hit resolution in both $r\phi$ and z

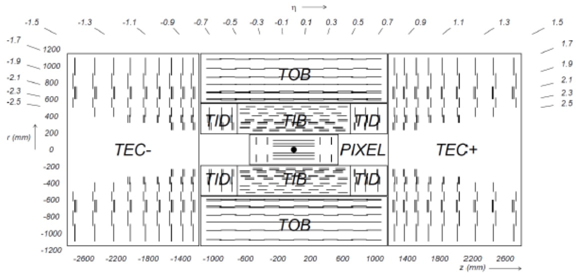

FIGURE 3.2: Schematic cross section through the CMS tracker

directions. It delivers three high precision points on each charged particle trajectory. It covers an area of about 1 m^2 and has 66 million pixels. The spatial resolution is about $15 - 20\mu$m.

The radial region between 20 cm and 116 cm is occupied by the silicon strip tracker, which provides the necessary granularity required to deal with high track multiplicities. It has a total of 9.3 million strips and 198 m^2 of active silicon area. The TIB and TID extend to a radius of 55 cm, and are surrounded by the TOB. The TOB extends in z between ± 118 cm. Beyond this z range, the TEC covers the region 124 cm $<\mid z \mid<$ 282 cm and 22.5 cm $<\mid r \mid<$ 113.5 cm. Some layers of the strip tracker are single-layered, and some double-layered. Double-layered modules, which have a second micro-strip detector module mounted back-to-back with a stereo angle of 100 mrad, allow the z (r) coordinate of a hit to be measured in the barrel (endcap). In the TIB, the strip pitch is 80 μm on layers 1 and 2, and 120 μm on layers 3 and 4; it varies between 100 μm and 141 μm in the TID, and between 97 μm and 184 μm in the TEC. The TOB has strip pitches of 183 μm on the first 4 layers, and 122 μm on layers 5 and 6. The single point resolution of the strip tracker is several tens of microns. TIB and TID in conjunction deliver up to 4 $r\phi$ measurements on a trajectory, the TOB another 6 $r\phi$ measurements, and the TEC up to 9 ϕ measurements.

For single muons (charged particles for which the tracker performance is the best, since muons are minimum ionizing particles), high momentum tracks (100 GeV) have a pT resolution of $1 - 2\%$ for $\mid \eta \mid< 1.6$; for $1.6 <\mid \eta \mid< 2.5$, the resolution is degraded due to the reduced lever arm. The impact parameter resolution reaches 10 m for high pT tracks, dominated by the resolution of the first pixel hit, while at lower momentum it is degraded by multiple scattering. The reconstruction efficiency for muon tracks is about 99% over most of the acceptance. At high η, the efficiency drops mainly due to the reduced coverage by the pixel forward disks. For pions, the efficiency is lower due to material interactions.

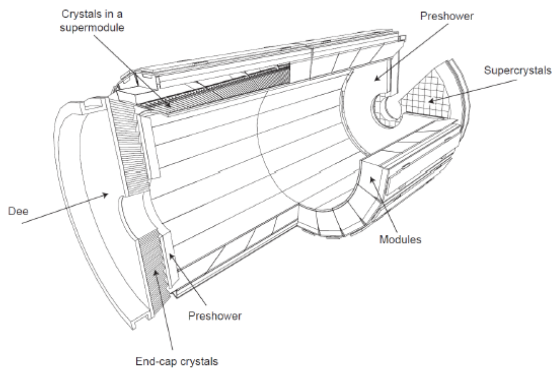

FIGURE 3.3: Layout of the CMS electromagnetic calorimeter showing the arrangement of crystal modules, supermodules and endcaps, with the preshower in front

3.2.2 The electromagnetic calorimeter

The ECAL, illustrated in Fig. 3.3, is a hermetic homogeneous calorimeter made of radiation resistant lead tungstate ($PbWO_4$) crystals. When an electron or photon passes through the ECAL, the result is a cascade or shower of electromagnetic particles that contain the energy of the original particle. The shower continues till the cascade particles no longer have enough energy to produce pairs, and are absorbed into the material of the calorimeter. Pions occasionally interact with the ECAL, but the HCAL usually gets the bulk of their energy deposit. Muons deposit little energy (~ 0.5 GeV) in the ECAL.

The scintillation decay time of the $PbWO_4$ crystals is of the same order of magnitude as the LHC bunch crossing time: about 80% of the light is emitted in 25 ns. There are 61200 crystals mounted in the central barrel (EB), and 7324 crystals in each of the two endcaps (EE). The EB granularity is 360-fold in ϕ and 2×85-fold in η. The EE consists of identically shaped crystals grouped in mechanical units of 5×5 crystals consisting of a carbon-fibre alveola structure. Each endcap is divided into 2 halves, or *Dees*. The nominal operating temperature of the ECAL is 18 °C. The cooling system, which employs flowing water, has to comply with this severe thermal constraint.

The photodetectors used are avalanche photodiodes (APDs) in the EB and vacuum phototriodes (VPTs) in the EE. The photodetectors need to be fast, radiation tolerant and be able to operate in the strong magnetic field. In addition, because of the small light yield of the crystals (about 4.5 photoelectrons per MeV at 18 °C), they should amplify and be insensitive to particles traversing them. The configuration of the magnetic field and the expected level of radiation led to different choices between EB and EE. The lower quantum efficiency and internal gain of VPTs compared to APDs is offset by their larger surface coverage on the back face of the crystals.

A preshower (ES) detector is located in front of the EE. Its main aim is to identify neutral pions in the endcaps within $1.653 <| \eta |< 2.6$. It also helps distinguish electrons from minimum ionizing particles, and improves the position determination of electrons and photons with its high granularity. It is a sampling calorimeter with two layers: lead radiators initiate electromagnetic showers from incoming photons and electrons, while silicon strip sensors placed after each radiator measure the deposited energy and the transverse shower profiles. A major design consideration is that all lead is covered by silicon sensors, taking into account the effects of shower spread, primary vertex spread etc. The lead planes are arranged in two Dees, one on each side of the beam pipe, with the same orientation as the crystal Dees. The total thickness of the ES is 20 cm.

One of the driving criteria in the ECAL design was the detection of the decay of the postulated Higgs boson to two photons. This capability is enhanced by the good energy resolution provided by a homogeneous crystal calorimeter. To achieve the most accurate energy measurements for electrons and photons, the ECAL needs to be well-calibrated. ECAL calibration is composed of a global component, giving the absolute energy scale, and a channel-to-channel relative component, referred to as intercalibration. The ultimate intercalibration precision is achieved with physics events like $W \to e\nu, \pi^0 \to \gamma\gamma$ and $\eta \to \gamma\gamma$. During intercalibration, ECAL response must remain stable to high precision. Changes in crystal transparency due to radiation damage are tracked and corrected using the laser monitoring system. The ECAL is able to accurately measure a wide range of energies, from 2 GeV up to a few TeV. The lower energy is important for the reconstruction of the Higgs boson decaying to b-jets; the upper energy is important for the discovery of new particle resonances. For energies $\sim$ 100 GeV, the energy resolution is better than 1%.

3.2.3 The hadron calorimeter

The HCAL, shown in Fig. 3.4, is crucial for the measurement of hadron jets and apparent missing transverse momentum (due to neutrinos or exotic particles that do not interact with the CMS detector). The HCAL is a hermetic sampling calorimeter, and uses alternating layers of absorber and scintillator. When hadrons pass sufficiently close to the absorber nuclei in the HCAL, there is a strong interaction between the hadrons and the protons and neutrons of the nearby nucleus. These interactions produce additional particles that share the energy of the original high-energy particle, each of which strongly interacts with nearby nuclei, resulting in a cascade of particles similar to an electromagnetic shower. This will continue until the particles all begin to slow down and get absorbed into the HCAL. The HCAL barrel (HB) and endcaps (HE) sit behind the inner tracker and ECAL as seen from the interaction point. The HB is radially

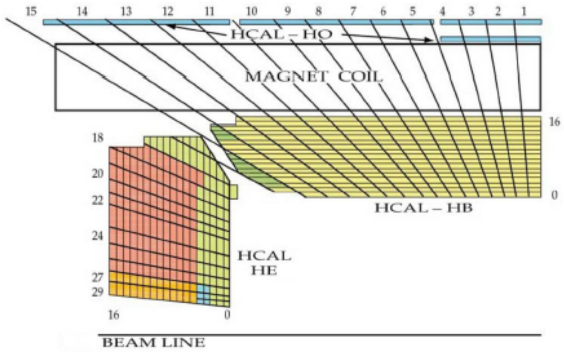

FIGURE 3.4: The HCAL tower segmentation in the rz plane for one-fourth the HB, HO, and HE detectors. The shading represents the optical grouping of scintillator layers into different longitudinal readouts.

restricted between the outer edge of the ECAL (R = 1.77 m) and the inner edge of the magnet coil (R = 2.95 m). This limits the total amount of material which can be put in to absorb the hadronic shower. Therefore, an outer hadron calorimeter (HO) is placed outside the solenoid complementing the barrel calorimeter. Beyond $\mid \eta \mid = 3$, the forward HCAL (HF) placed at 11.2 m from the interaction point extend the coverage to $\mid \eta \mid = 5.2$ using a Cherenkov-based, radiation-hard technology.

The HB is divided into two half-barrel sections, with coverage up to $\mid \eta \mid$ ¡ 1.3. It consists of 36 identical azimuthal wedges constructed out of flat brass absorber plates aligned parallel to the beam axis. The plastic tile scintillator, chosen for its long-term stability and moderate radiation hardness, is divided into 16 η sectors. The HCAL consists of about 70 000 tiles. Light from each tile is collected with a wavelength-shifting fiber. The HE has a coverage of $1.3 <\mid \eta \mid< 3$, a region containing about 34% of the particles produced in the final state. The high luminosity of the LHC requires HE to handle high (MHz) counting rates and have high radiation tolerance. Since the calorimeter is inserted into the ends of the solenoid, the absorber must be non-magnetic, have a maximum number of interaction lengths to contain hadronic showers, have good mechanical properties and be affordable: brass fulfils these criteria. The absorber design is driven by the need to minimize the cracks between HB and HE, and not single-particle energy resolution, since the resolution of jets in HE is limited by pile-up, magnetic field effects, and parton fragmentation.

The HO utilizes the solenoid coil as an additional absorber and is used to identify late starting showers and to measure the shower energy deposited after HB. The mean fraction of energy in HO increases from 0.38% for 10 GeV pions to 4.3% for 300 GeV pions. The HF experiences unprecedented particle fluxes: on average, it gets 760 GeV per proton-proton interaction, compared to only 100 GeV for the rest of the detector. Moreover, this energy is not uniformly distributed, but has a pronounced maximum at

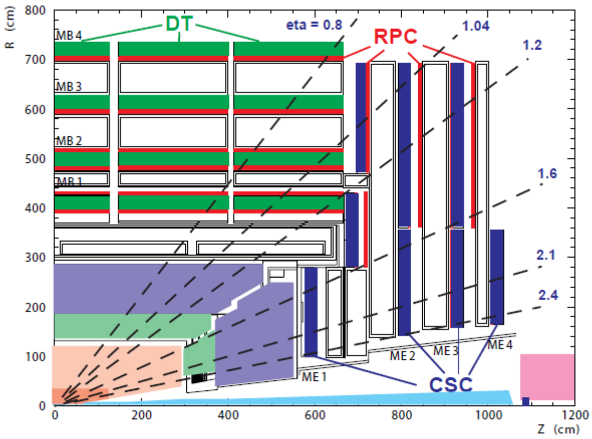

FIGURE 3.5: A view of the CMS muon detector

the highest values of $|\eta|$. The charged hadron rates are also extremely high. Steel interleaved with quartz fibers (as the active medium) was chosen to survive under these harsh conditions. The HCAL energy resolution is about 30% for 10 GeV pions, and about 10% for 100 GeV pions.

3.2.4 Muon detector

High p_T muons provide the cleanest signature for many of the SM processes studied at the LHC, as well as a signature for new discoveries. The muon detector system, shown in Fig. 3.5, must identify muons and trigger on them with large efficiency, even in the presence of multi-muon events, up to $|\eta| = 2.1$ and with no acceptance loss. It should be able to unambiguously assign a bunch crossing to each muon candidate, and correctly assign charge even for low p_T muons. For large p_T tracks (p_T ¿ 200 GeV), the muon p_T determined by measuring the sagitta of the global muon track (obtained by combining the inner tracker information with the muon detector information) should be precise enough to substantially improve the precision of the p_T measured by the inner tracker alone.

Besides the constraints mentioned above, there are two main factors to consider when choosing the type of detector technology: first, the very large surface area to be covered, and second, the different radiation environments involved. For identifying and measuring muons, there are three types of gaseous detectors involved. In the barrel region ($|\eta| <$ 1.2), where the neutron induced background is small, as is the muon rate and the residual magnetic field ($<$ 0.4 T), drift tube (DT) chambers are a good choice. In the two endcaps, where all three of these quantities are high, cathode strip chambers (CSC) are utilized, and cover the region up to $|\eta| < 2.4$. In addition to this, resistive plate chambers (RPC) extend over the barrel as well as the endcap. RPCs have a fast response, with good time resolution, though their position resolution is coarser than the DTs or CSCs. Hence RPCs can unambiguously identify the correct bunch crossing. The DTs or CSCs and the RPCs provide two independent and complementary sources of information, and operate within the Level 1 trigger. The magnet return yoke of the CMS detector is subdivided into 5 wheels and 2×3 endcap discs, and is instrumented with a system of muon chambers. In the Muon Barrel (MB) region, 4 stations of detectors are arranged in cylinders interleaved with the iron yoke. The segmentation along the beam direction follows the 5 wheels of the yoke (labeled YB2 for the farthest wheel in z, and YB+2 for the farthest in +z). In each of the endcaps, the CSCs and RPCs are arranged in 4 disks perpendicular to the beam (ME1 to ME4), and in concentric rings, 3 rings in the innermost station, and 2 in the others. In total, the muon system contains of order 25,000 m^2 of active detection planes, and nearly 1 million electronic channels. DT Chambers in the four different MB stations are staggered so that a high pT muon produced near a sector boundary crosses at least 3 out of the 4 stations. Each station is designed to give a muon vector in space, with a precision better than 100 μm in position in the rϕ plane, and approximately 1 mrad in ϕ. The muon endcap (ME) is arranged in 4 disks (ME1 - ME4), referred to as stations. Each station is subdivided into rings. Each ring is filled with CSCs, which are trapezoidal multiwire proportional chambers. Closely spaced wires make the CSC a fast detector (response time of $\sim$ 4.5 ns),

which is why it is used in the Level 1 Trigger. However, it leads to a coarser position resolution than the DTs: the spatial resolution in the rϕ plane provided by each chamber from the strips is typically about 200 μm, and the angular resolution in ϕ is of order 10 mrad. CSCs can operate in large and non-uniform magnetic field without significant deterioration in their performance. Each RPC detector consists of a double-gap bakelite chamber operating in avalanche mode to ensure good operation at high rates (up to 10 kHz/cm^2). RPCs guarantee a precise bunch crossing assignment thanks to their fast response and good time resolution.

The muon detection system is capable of identifying single and multi-muon events with well determined p_T in the range of a few GeV to TeV. The reconstruction efficiency is greater than 96% if $p_T > 20$ GeV (the range that is relevant for this analysis) and around 80% for $p_T = 5$ GeV. The momentum resolution $\Delta p_T/p_T$ is 1 - 1.5% when $p_T \sim 10$ GeV and 6 - 17% when $p_T \sim 1$ TeV (the large range is due to η dependence). The momentum resolution of muon tracks up to $p_T = 200$ GeV reconstructed in the muon system alone is dominated by multiple scattering. Thus, at low momentum, the best momentum resolution for muons is obtained from the silicon tracker. At higher momentum, the characteristics of the muon system allow the improvement of the muon momentum resolution by combining the muon track from the silicon detector, *tracker track*, with the muon track from the muon system, $stand-alone\ muon$, into a *global*

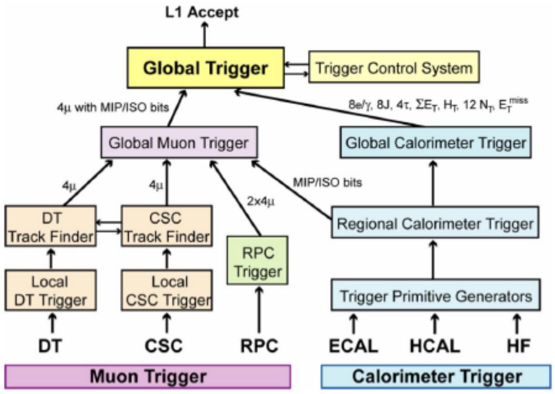

FIGURE 3.6: Trigger architecture

muon track using track matching. A complementary approach to global muons consists of considering all silicon tracker tracks and identifying them as muons by looking for compatible signatures in the calorimeters and in the muon system. Muons identified with this method are called *tracker muons*.

3.2.5 Trigger and data acquisition

As mentioned previously, a reduction by a factor of 10^7 needs to be achieved when going from the inelastic collision rate at the nominal LHC luminosity of 10^{34} cm^{-2} s^{-1} to the rate at which collision data can be stored. CMS does this by using two components: the Level 1 trigger (L1T) system, a fast hardware-based trigger, and the High Level Trigger (HLT) system, which is software-based. The reduction in data is accomplished by triggering on event features that are characteristic of rare and interesting physics processes.

The L1T uses only coarsely segmented data from calorimeter and muon detectors, while holding all the high-resolution data in pipeline memories in the front-end electronics. It forwards no more than 100 kHz of the stored events to the HLT. For an event to pass the L1T, it must meet certain threshold requirements on the p_T or E_T of individual physics objects, or on scalar or vector sums of the same quantities. The L1T is comprised of several subcomponents associated with the different subdetectors: the bunch crossing timing, the L1 muon systems (CSC, DT, RPC) which feed the Global Muon Trigger, and the L1 calorimetry (ECAL, HCAL, HF) which feed the Regional Calorimeter Trigger and then the Global Calorimeter Trigger. All these inputs are passed to the Global Trigger (GT), as shown in Fig. 3.6. The GT has the ability to provide up to 128 trigger algorithms to select an event based on logical combinations of L1 objects, such as muons, jets, or calorimeter energy sums. In addition, there are 64 *technical triggers* that are used for detector diagnostics or monitoring. The L1T has a latency of 3.2 s, after which the detector information from the event must either be dropped or sent to the front-end readout buffers. Events that are retained undergo signal processing, zero-suppression, data compression, and then sent to the HLT.

The HLT is capable of a greater rejection power than the L1T because it has additional time to calculate kinematic variables using complete read-out data from all detector subsystems necessary for a particular reconstruction. It relies upon about a thousand commercial processors to perform complex calculations similar to those made in the the analysis offline software. Since there are timing constraints that the HLT has to satisfy (average execution time for a trigger path should be 10 ms, with an upper limit of 40 ms), the reconstruction algorithms employed online are often simpler than what is used offline, and care has to be taken to ensure that this does not affect the physics analyses.

Events that are accepted by the HLT are sent to the Storage Manager, the last piece of the data-handling chain. The Storage Manager has two principal purposes. The first is to collect the events from the processor farm of HLT, and store the events in files for later transfer and processing. These data files are then assigned to different output streams, each stream being defined as a collection of several HLT trigger paths. The files are routed according to which HLT paths were triggered by a given event, and which streams those paths belong to. The grouping is usually determined based on offline usage (e.g., *physics* stream, *express* stream, *calibration* streams, etc.). The second function of the storage manager is to act as an event server for calibration and monitoring purposes.

Chapter 4

Physical Object Reconstruction

4.1 Luminosity measurement

The $instantaneousluminosity L$ at a collider machine, where one observes a rate of R for a physical process with cross section σ, is defined as:

$$L = \frac{R}{\sigma} \tag{4.1}$$

It depends on machine parameters, such as beam transverse dimensions, number of protons per bunch and number of bunches in the beams. It is a time dependent quantity $L(t)$ (since the beams degrade with time) that integrated over the data-taking period becomes the measurement of collected statistics, called $integratedluminosity$:

$$L_{int} = \int_{time} L(t)dt \tag{4.2}$$

The real-time luminosity monitoring must be based on the measurement of a high, well known, cross section process using as little hardware as possible. One method of luminosity determination [45] is the "zero counting", where the luminosity is derived from the probability that a tower of the hadronic forward calorimeter (HF) sees zero hits in a single collision. Another, more accurate method is "Pixel Cluster counting": there is a good correlation between the luminosity and the number of hit clusters in the Silicon Pixel detector. Due to their tiny size the individual pixels have a small occupancy and this allows to use this method also at very high luminosities. The pixel-based method is used in CMS. The systematic error assigned to the luminosity collected during 2012 is 4.4% [46]. Systematic uncertainties are higher in 2012 data compared to 2.2% from

2011 data. 2012 data are recent and less understood than 2011 ones; in addition the calibrations of detectors are preliminary in many cases.

4.2 Electrons

Electron reconstruction [47] begins with the clustering of ECAL energy deposits. In the absence of material interactions in the beampipe or tracker, approximately 94% of the incident energy of a single electron is contained in 3 × 3 crystals, and 97% in 5 × 5 crystals. Due to the strong magnetic field, and electrons undergoing Bremsstahlung, the energy deposited in the ECAL is spread in ϕ. This energy is clustered by building a group of clusters, a *supercluster*(SC), which is extended in ϕ. Figure 4.1(a) shows the material budget of the CMS detector. Figure 4.1(b) shows an illustration of an electron as it radiates photons when traveling through the tracker layers. CMS employs a *hybrid* algorithm in the EB, and an *island* algorithm in the EE; these are discussed in greater detail elsewhere.

Non-overlapping clusters are grouped into a SC. The procedure is seeded by searching for the most energetic cluster (seed cluster), and then by collecting other clusters in a fixed search area around the seed position. The clusters belonging to radiation from a single electron are aligned in η, but spread in ϕ. By collecting all the clusters in a narrow η window, whose size is dictated by the η resolution of the detector, it is possible to recover most of the radiated energy. The energy of the SC is corrected based on the number of crystals in the seed cluster, and to remove any residual η dependence. The position of the shower is obtained by calculating the energy-weighted mean position of the crystals in the SC. There are two issues with this approach: one is related to the definition of the position of a crystal, the other to the fact that a simple energy-weighted mean is biased towards the center of the crystal containing the largest energy deposit (seed crystal). How these issues are handled is discussed elsewhere [15].

To complete the process of electron reconstruction, the SC needs to be associated with a track in the inner tracker. Electron tracking begins with the formation of a *pixel seed*, which involves finding a pair of hits in the inner tracker consistent with the trajectory of electron: the assumption is that the curvature of the trajectory is given by the E_T of the SC, and that the trajectory comes from the origin. The pixel seed itself is a vector located at the outer hit position, pointing in the direction of the electrons trajectory, and serves as the starting point for tracking. The standard seed-finding process is referred to as pixel-matching, since the hit pair is usually located in the pixel layers.

A major difficulty of electron reconstruction is that electrons can undergo Bremsstrahlung in the tracker material. The radiation affects both the energy and momentum measurement, and this effect depends on the material thickness. To account for Bremsstrahlung losses, CMS employs a Gaussian-Sum Filter (GSF) track fit. This fit uses the Bethe-Heitler model of electron energy loss, and approximates the energy loss distribution as a sum of Gaussian distributions. Different Gaussians model different degrees of hardness of the Bremsstrahlung in the layer under consideration. The GSF fit allows for good momentum resolution at the vertex while also providing a meaningful estimate of the momentum at the outermost part of the tracker.

The matching of the track and SC is based on their angular separation (ΔR):

$$\Delta R = \sqrt{(\eta_1 - \eta_2)^2 + (\phi_1 - \phi_2)^2} \tag{4.3}$$

where (η_1, ϕ_1) and (η_2, ϕ_2) are the coordinates of any two positions (in this case, the track position at the ECAL, and the SC position). The energy of the electron is the errorweighted average of the corrected SC energy and the magnitude of the track momentum (since the mass of the electron is negligible when compared to GeV scale momenta). Figure 4.2(a) shows the improvement to the energy resolution of the electron by combining the track and SC information. Figure 4.2(b) shows the energy resolution of 120 GeV electrons before and after corrections.

We consider electrons over the range $\mid \eta \mid < 2.4$, excluding the overlap between the barrel and endcap ($1.44 < \mid \eta \mid < 1.57$). There are four types of electron candidates: prompt, non-prompt, conversion, and fake. Prompt electrons mainly come from the decay of W and Z bosons, and are of great importance to us. Non-prompt electrons arise from b or c quark decaying to an electron. Although these electrons are usually not isolated within the quark jet, since there is a significant amount of nearby electromagnetic and/or hadronic activity, the kick from the quark decay might knock the electron out of the jet enough for it to appear isolated. Conversion electrons come from a photon producing an electron-positron pair in the tracker. Fake electrons are a result of reconstruction error: a coincidence of a jet depositing a large amount of energy in the ECAL and a nearby (matched) single, high-p_T track is misinterpreted as an electron. Nonprompt, conversion and fake electrons are a background source of electrons that need to be greatly reduced: this is accomplished by placing quality requirements (*cuts*) on the electron candidates. The variables that help distinguish prompt electrons from fake and non-prompt electrons are:

- $\Delta\eta_{in}$ and $\Delta\phi_{in}$: The difference in η and ϕ between the track position at the ECAL extrapolated from innermost track state, and the η and ϕ of the SC. A large difference would indicate a fake electron.

- H/E: The ratio of the hadronic energy in a cone of radius $\Delta R < 0.1$ around electron position in the calorimeter to the electromagnetic energy of the SC. This variable provides useful discrimination between electrons and jets, as electrons deposit little energy (if any) in the hadronic calorimeter, unlike most jets.

- $\sigma_{\eta\eta}$: A measure of the η spread of the electrons energy deposit in the 5×5 block centered on the ECAL seed crystal. A large spread in the energy deposition by the electron candidate indicates that the candidate was most likely a jet.

- Impact parameters: An impact parameter is the distance of closest approach of the electron trajectory to a certain point. The two impact parameters we use are d_0, measured in the transverse plane with respect to the beam spot, and d_z, measured along the beam direction with respect to the primary vertex.

- $I^{combined}/p_{T,lepton}$: Combined relative isolation. $I^{combined}$ is the sum of the transverse energy E_T (as measured in the electromagnetic and hadron calorimeters) and the transverse momentum p_T (as measured in the silicon tracker) of all reconstructed objects within a cone of $\Delta R < 0.3$ around the electron direction, excluding the electron.

Table 4.1 lists the requirements on these quantities. Conversion electrons are rejected by requiring that:

- There are no hits that are expected but missing in the inner tracker.

- The distance between possible conversion tracks is at least 0.02 cm.

- $\Delta(cot\theta)$ between possible conversion tracks at the conversion vertex is at least 0.02.

Additionally, the electron must satisfy $\Delta R > 0.3$ with respect to all jets with p_T ¿ 40 GeV and $\mid \eta \mid < 2.4$. This is used to distinguish jets from electrons.

4.3 Muons

Muon reconstruction [48] involves the inner tracker, combined with the muon system (DT, CSC, RPC). This was discussed in some detail in Chapter 3. Track reconstruction in the muon system makes use of the track hits and track segments (set of aligned hits) from the muon subdetectors. The algorithm starts from a locally-reconstructed muon track segment in one of the innermost detector stations; it is used as a seed for a Kalman filter which builds trajectories going radially outward. A χ^2 cut rejects hits unlikely to be associated with the track. The trajectory is propagated using a detailed map of the magnetic field and taking account of energy loss in the detector material (mainly the steel of the magnet return yoke), until the outermost detector layer of the muon system is reached. An outside-in Kalman filter is then applied, and the track parameters are defined at the innermost muon station. Finally, the track is extrapolated to the nominal interaction point and a vertex-constrained fit to the track parameters is performed. The muons used in this analysis are reconstructed by combining fitted trajectories in the silicon tracker and the muon chambers (*global* muons). Muons are reconstructed over the range $\mid \eta \mid < 2.4$, but we only use muons with $\mid \eta \mid < 2.1$ in this analysis.

Muon reconstruction is easier than electron reconstruction in many ways. Muons are minimum ionizing particles, so they are much less prone to ionizing or exciting atoms/ molecules in material that they encounter. They are also much less susceptible to Bremsstrahlung than electrons. This is because the total power radiated by a particle in this situation is proportional to γ^4 (γ is is the Lorentz factor), and for the same energy, the more massive a particle, the smaller its Lorentz factor ($E = \gamma mc^2$). Because of the muon chambers, a high p_T muon track consists of about 30 hits, compared only 10 hits for a high p_T electron track, so muon tracks have better p_T resolution.

Like electrons, muons suffer from background in the form of non-prompt and fake muons. The nature of fake muons is different from that of fake electrons: they are hadronized quark jets that penetrate through the HCAL (the $punch - through$ effect). The HCAL, and especially the HO, is designed to prevent this from happening: the total depth of the calorimeter system is a minimum of 11.8 interaction lengths, where one interaction length reduces the number of particles by $1/e$. However, not all jets can be stopped. For a fixed lepton efficiency, reducing muon backgrounds is easier than reducing electron backgrounds, since punch-through muons are rarer than fake electrons. A number of quality cuts are applied to reject fake and non-prompt muons. Muon candidates must have:

- a χ^2 per degree of freedom (of the global fit) less than 10, and at least one muon chamber hit used in the fit ($GlobalMuonPromptTight$).
- at least 11 hits in the inner tracker (with at least one hit in the pixel system) and 2 matched segments in the muon system.
- an uncertainty in the fitted inverse transverse momentum of $\sigma(p_T)/p_T^2 < 0.001$ GeV^{-1}.

- $I^{combined}/p_{T,lepton} < 0.1$. electron.

In addition, the candidates must pass the same impact parameter cuts as electrons, and qualify as a tracker muon. Finally, like electrons, muons must satisfy $\Delta R > 0.3$ with respect to all jets with $p_T > 40$ GeV and $\mid \eta \mid < 2.4$.

4.4 Taus

The tau, as the heaviest lepton, can decay into lighter leptons as well as hadrons. The reconstruction of taus therefore is far more complicated than electron and muon reconstruction. And achieving a high purity (real taus divided by all reconstructed taus) is rather difficult in contrast to lighter leptons. Due to this complexity, it is sometime ignored completely in a clean leptonic analysis, or restricted to only the single charged pion mode. In the SM, heavy particles exhibit lepton universality in the BR (*i.e.*, BRs are the same for all lepton families). If the physics beyond the SM also has such a universality, then the muon channel is the golden mode of discovery in terms of its high purity and precise p_T measurements. Interestingly, in the MSSM, the heaviest slepton (squarks) have heavier masses among sleptons (squark) in higher tanβ parameter space, resulting higher BRs for those heavier particles. Suppose the muon channels are checked first and no excess found beyond the SM. Yet, the physics beyond the SM is lurking in the tau channels if tau BR is significantly enhanced. Therefore, it is worth analyzing taus even given its challenging nature.

About two thirds of tau decays are hadronic, and the other one third is leptonic. As long as the decay is leptonic, it can be reconstructed as lighter leptons. The challenging decays are the hadronic ones. Henceforth, taus refer to hadronic decaying taus. The cross section of the QCD processes are the largest at pp colliders. In the calorimeters, there are not much difference between QCD jets and hadronic tau decays. This poses the first and the biggest challenge to hadronic tau reconstruction.

This section follows reference [49]. The first half of this section is devoted to the reduction of QCD backgrounds, and the latter half describes electron and muon rejection. The algorithm used in this analysis is a cut-based shrinking cone, and assumes taus originating from a heavy particle, like Z, W, and $Higgs$. In other words, a narrow signal cone contains all tau decay products (due to Lorentz boost).

4.4.1 Particle flow

The reconstruction uses Particle-Flow (PF) techniques, which has been validated with the early data in 2010. The particle-flow algorithm aims at providing a global event description at the level of individually reconstructed particles with a combination of information coming from all the CMS detector components. The reconstructed and identified individual particles are muons, electrons, photons, charged hadrons, and neutral hadrons. The complete list of particles may then be used to derive composite physics objects such as clustering into jets with standard jet algorithms. The algorithms discussed in this analysis use this list of particles both for reconstruction and identification of taus. Specifically, all reconstructed particles in the event including charged pions and photons from any possible hadronic tau decay products are clustered into jets with the AK algorithm.

The tau algorithm benefits from both the improved energy and angular resolution available describing each individual particles in the jet. The benefits of using it can be summarized in three points:

- First, better energy and momentum resolution from the inner tracker and ECAL for charged hadrons and neutral pions
- Second, no azimuthal angle bias for charged hadrons because the momenta are determined. at the primary vertex where the axial magnetic field has no effect.
- Third, not affected by the JES correction tuned for QCD jets.

4.4.2 Base reconstruction

The baseline of tau selection requires that a minimum transverse momentum is required to each jet and only those satisfying it are further considered as a possible tau candidate. A narrow signal cone is defined around the direction of the leading object, and an isolation annulus expected to contain little activity is defined as a cone larger than but excluding the signal cone. At least one charged hadron with $p_T > 5$ GeV/c is required to be found within a distance from the jet axis < 0.1 in R.

Default isolation requires no reconstructed charged hadron with p_T above 1 GeV/c and no photon with E_T above 1.5 GeV inside the isolation annulus. In this analysis, a shrinking cone algorithm, which defines its signal cone size as 5.0 GeV/pT, is used.

4.4.3 High level reconstruction

The base reconstruction successfully rejects most QCD jets. However,it does not reject most electrons and muons, which are the perfect tau candidates as it provides a good track and energy deposits in the calorimeters.

The electron pre-identification algorithm uses a multivariate analysis of the tracker and calorimeter information which provides efficient seeds for full electron reconstruction. The electron pre-identification achieves 90-95% efficiency across the entire tracker acceptance, with about 5% pion efficiency. In order to optimize the electron rejection efficiency beyond 95%, two additional variables are formed.

The first variable E/P is defined as the summed energy of all ECAL clusters in a narrow strip $\mid \Delta\eta \mid < 0.04$ with respect to the extrapolated impact point of the leading track on the ECAL surface divided by the momentum of leading track inside the jet. This variable is expected to cluster around unity for electrons and to be scattered around smaller values for charged pions from tau decays.

The second variable, H_{33}/P is defined as the summed energy of all the HCAL clusters within $\Delta R < 0.184$ around the extrapolated impact point of the leading track on the HCAL surface divided by the momentum of the leading track inside the jet. This variable is expected to cluster around zero for electrons and to be somewhat randomly distributed for charged pions from tau decays.

The high efficiency of the standard muon reconstruction and identification in the CMS provides optimal rejection of muons in the reconstruction if the muon information is used. Tau candidates are rejected if their leading track matches to a global muon, or the matched muon has at least one muon chamber segment, as real pions usually are not reconstructed as global muons.

4.5 Jets

The typical jet energy fractions carried by charged particles, photons, and neutral hadrons are 65%, 25%, and 10%, respectively. This means that 90% of the jet energy (the fraction from charged particles and photons) can be reconstructed with good precision by the PF algorithm, both in magnitude and direction; only the remaining 10% of the energy (the fraction from neutral hadrons) is affected by the poor HCAL resolution, and by calibration corrections of about 10 to 20% (a source of uncertainty that that ECAL does not suffer from). Consequently, jets made of reconstructed particles are much closer to jets made of generated particles than jets reconstructed using only calorimeter information, in energy, direction, and content.

Jet clustering is performed using the anti-kT clustering algorithm. Particles reconstructed with the PF algorithm (as explained in Sec. 4.3.1.3) that are above a certain energy threshold and within a ΔR cone of 0.5 are clustered into PF jets. All PF jets below 10 GeV are considered to represent unclustered energy. Applied jet energy corrections include: offset (L1FastJet with active area calculation), relative (L2), and absolute (L3). The purpose of the offset term is to correct for pile-up; the relative corrections smooth out any η dependence, and the absolute corrections relate to the overall energy scale. Additionally, jets in data have residual corrections applied to them to account for data-simulation discrepancies, since the other corrections are based on simulation. Jet candidates are required to satisfy loose quality criteria that suppress noise and spurious energy deposits:

- at least two particles (at least one of them charged) in the jet.
- energy fraction of neutral hadrons < 0.99.
- both charged and neutral electromagnetic energy fractions < 0.99.

Jets must have $p_T > 40$ GeV and $\mid \eta \mid < 2.4$. We form $H_T = \Sigma p_T$, where the sum is taken over all jets passing the selection just described.

4.6 Missing Transverse Energy

We define $\vec{\not{E}_T} = -\Sigma \vec{p_T}$, where the sum is over PF objects reconstructed offline, and $\not{E}_T = \mid \vec{\not{E}_T} \mid$. In CMS, the $\not{E}_T$ used by us is referred to as *uncorrected* $PFMET$. An alternative is to use $type - I$ *corrected* $PFMET$, a propagation of the jet energy corrections to $\not{E}_T$. However, there are no existing studies showing that the use of $type - I$ *corrected* $PFMET$ provides any benefit, hence we use *uncorrected* $PFMET$.

Chapter 5

Data and Simulation

The Monte Carlo simulation samples for SM background and signal are centrally produced and distributed. But a few signal samples are produced centrally. There is a best bookkeeping tool to locate available copies of samples from all over the world to the location to be moved. That an easy way is the CMS Data Bookkeeping System.

5.1 The CMS software

The event generation is done by Pythia alone or a combination of Pythia and supported external event generators. The CMS software (CMSSW) serves that event generation. To make use of the CMSSW, IOMC provides such an interface for the format to be adapted to the specifications of CMSSW. The output file is consequently converted to a ROOT [50] file ready to be passed through all the steps of the CMSSM. First, the cmsdriver tool automatically generates configuration file from the database, and produces a collection of all generation steps. That specified generation steps are GEN, SIM, and RECO. The GEN step puts all generated particles into the GenParticle collection and subsequently the detector simulation is performed. This simulates the detector responses for all particle trajectories resulting in hits and energy deposits. That is just the way a real collision would produce particles traversing through the detectors. This step has DIGI, L1, DIGI2RAW, and HLT process, where DIGI digitizes simulated hits, L1/HLT performs the L1/HL trigger decision, DIGI2RAW coverts the digitized hits to the RAW format. The RAW format is equivalent to the data coming from the CMS detector with real collisions. The data format contains all hits and energy deposits is called SIM. There is a Fast Sim, a faster version of SIM, although which is less precise in terms of detector response, it is faster than full Sim by a factor of 10. Full Sim is used for background and benchmark signal points(lm9) in this analysis, and fast Sim is used for SUSY parameter space scan. And then, the reconstruction is performed. The reconstruction section describes more the methods of reconstruction. The data format after the reconstruction is RECO format. That contains high level physics objects (*i.e.*, particle types and 4-vectors). That RECO data format is already ready to be used by analyzer. And the users are encouraged to reduce further the amount of data size by converting RECO to AOD format, Analysis Object Data. The AOD data format is a CMSSW Data Format, which is proper subset of the RECO data formats and sufficient for a large set of CMS analyses. the users are able to apply basic cuts on particle properties by using the Physics analysis Tool Kit(PAT), that create ntuple files with smail size.

5.2 Monte Carlo samples

The Simulated samples with Monte Carlo (MC) used for this analysis is fully from 2012 8 TeV production. Those samples are reconstructed in CMSSW release 54X. The NLO cross sections are used for all SM background and SUSY signal processes. The k-factors for signal samples are computed with PROSPINO [51]. SUSY parameter space scan samples are produced with CMSSW54X, the GMSM points produced by the SUSY group are used as well.

$SMMCSamples$	$Generator$	$\sigma(pb)$
TTJets MassiveBinDECAY TuneZ2star 8TeV	madgraph	225.2
DYJetsToLL M-50 TuneZ2Star 8TeV	madgraph	3532.8
DYJetsToLL M-10To50filter 8TeV	madgraph	228.735
ZZJetsTo4L TuneZ2star 8TeV	madgraph	0.1769
WZJetsTo3LNu TuneZ2 8TeV	madgraph	1.0575
WWWJets 8TeV	madgraph	0.08217
WWJetsTo2L2Nu TuneZ2star 8TeV	madgraph	5.8123
WJetsToLNu TuneZ2Star 8TeV	madgraph	37509
ZG Inclusive 8TeV	madgraph	123.9
$SUSYMCSamples$	$Generator$	$\sigma(pb)$
LM9 SUSY	Pythia6	9.287
TChiWZ	Pythia6	1.0
TChiSlepSnu	Pythia6	1.0
Higgsino GMSB	Pythia6	1.0

TABLE 5.1: Simulated event samples used in this analysis. The cross section and generator information is given above.

5.3 Data

The data used for this analysis have been collected by CMS detector during the 2012 period. That corresponds to an integrated luminosity of 19.5 fb^1 with a center of mass energy of 8 TeV, which is based on the certified JSON as in Table 5.2.

Data sample	Integrated luminosity [fb^{-1}]
/DoubleMu/Run2012A-13Jul2012-v1	0.809
/DoubleMu/Run2012A-recover-06Aug2012-v1	0.082
/DoubleMu/Run2012B-13Jul2012-v4	4.43
/DoubleMu/Run2012C-24Aug2012-v1	0.49
/DoubleMu/Run2012C-PromptReco-v2	6.40
/DoubleMu/Run2012D-PromptReco-v2	7.27
Total Integrated luminosity	19.5 fb^{-1}

Table 5.2: List of data samples and the corresponding integrated luminosity.

Chapter 6

Background Estimation

6.1 Signal Signature and Background

6.1.1 Background

In general, backgrounds to this topology are relatively small, while come from a variety of sources. We can separate these into two categories: 1) backgrounds with one or more fake lepton, electron, muon and hadronic tau, which is non-prompt lepton. 2) backgrounds with three or more prompt leptons. Several methods are employed to predict the background contamination from the Standard Model from each of these sources. Many of those are derived partially or fully from data. We rely on simulation for the background expectation for the rarest Standard Model processes. The expected contribution from each source of background is estimated from Monte Carlo simulations.

6.1.2 Drell-Yan

It is an important type of background with the multi-lepton signal which comes from topologies which produce two prompt leptons (i.e. decay products of W or Z bosons) and a third lepton originating from a heavy-flavor (or a light-flavor) jet.

The dominant background for this study is diboson + jets production. If there is at least one fake lepton in the event, Drell-Yan processes include two prompt leptons in the final state can only contribute to three lepton channels. The events with three and four muons or electrons come from WZ, ZZ production. Because that backgrounds are irreducible with quality selection, that should be predicted by data driven technique. Non prompt but isolated leptons come from the decay of heavy flavor mesons, which is plagued by rather uncertain cross sections. so the fake lepton rate must be controlled from data.

The diboson events produce two or three prompt and isolated leptons similar to SUSY multi-leptonic signatures, but the main source of missing transverse energy is from neutrinos. Contrast to that diboson events, the lightest SUSY particle(LSP) makes large missing transverse energy. Therefore, the difference ratio shows good shape information for signal regions compared to SM sideband including two tight leptons and at least one fake lepton. All three prompt and isolated leptons can be selected by requiring two tight opposite sign same flavor leptons and an additional tight lepton. The tight leptons has the tight selection criteria an relative isolation requirement $PFRiso > 0.15$.

6.1.3 $t\tilde{t}$

$t\tilde{t}$ processes are the next important dilepton process. An additional fake lepton is present can contribute to the signal region. Top quark production as well as Z+jets, WW+jets constitute the main processes that contribute to this background. The event selection to have at least three tight leptons with high p_T suppress the $t\tilde{t}$ background well. The b-jet veto reduces the top background significantly, leaving a small fraction due to b jets out of acceptance or inefficiencies of the b-tagging algorithm. In contrast to $Z/\gamma*$ +Jets processes, $t\tilde{t}$ events with two prompt leptons contain two associated neutrinos in the final state leading to two b-jets and missing transverse energy.

If an additional fake lepton contributes to signal region, this combination of dileptons with missing energy leads to SUSY-like trilepton signatures. The production mechanism for fake leptons in $t\tilde{t}$ is similar to $Z/\gamma*$ +Jets, but the b-jet density varies in the processes. The determination from $Z/\gamma*$ +Jets events can not be used for $t\tilde{t}$. A fake lepton enriched $t\tilde{t}$ sample with opposite flavor leptons one has to suppress the dominant process $Z/\gamma* \rightarrow \tau\tau$, where each tau decays leptonically $\tau \rightarrow l\nu_l\nu_\tau$. Requirement on at least one b-tagged jet is required to enhance $t\tilde{t}$ processes. However, the requirement on b-tagged jet is not considered for this analysis.

6.2 Preselection

The preselection is to reduce the SM background contributions to the negligible level of the SUSY signal events. The quantities which have been cut on are explained in reconstruction sections. There are many study to apply common preselection for multilepton analysis [52] [53].

6.2.1 Trigger selection

In this analysis we select events triggered by double lepton trigger. The threshold on leading particle is 17 GeV and that on the next to the leading particle is 8 GeV. All the triggered data used for this analysis is based on the certificated datasets The trigger paths used for this analysis are following;

- HLT_Mu17_Mu8

6.2.2 Muon selection

A primarily study of the muon identification efficiency has used the official Tag and Probe tool for the datasets from Run A to Run D. Overall the agreement is good, and the muon reconstruction in the CMS-Detector is understood well. Muons are selected by a simple set of cuts to suppress the fake muons in the signal region. Requirements on the muon track are applied to select only well reconstructed muons. Those are the quality of the global fit χ^2 and the number of hits in the tracker $NTrackHits$. All selection requirements are listed in Table 6.1.

The selection criteria on the relative isolation PFRiso is effective to suppress fake leptons from jets. The applied cut variable, PFRiso, is defined as the sum of all photons, charged and neutral hadrons in a cone $\Delta R < 0.3$ around the muon candidate relative to the transverse momentum of the muon as following:

$$PFRIso = \frac{[\Sigma p_T^{chargedHad} + max(0.0, \Sigma p_T^{neutralHad} + \Sigma p_T^{photons} - \rho A_{eff}(NH+PH)]}{p_T}$$

The PFRiso is corrected using the Delta Beta corrections. Additional also a requirement on the impact parameter in the xy-plane with respect to the primary vertex d_{xy}(PV) is applied. The well reconstructed muons are selected by 'isGlobalMuonPromptTight' and Particle-Flow muon id ='isPF'. The valid number of hits is greater than 10 in tracker. The requirement of relative isolation is smaller than 0.15 around the muon candidate. The impact parameter in the xy-plan with respect the primary vertex d_{xy} is required to be smaller than 0.02 to suppress fake leptons from jets.

6.2.3 Electron selection

The electron selection is based on a set of simple cuts, which is similar to muons. The identification requirements follow the loose WP recommendation [54]. Fake electrons are dominated by fakes from jets and fakes from asymmetric photon conversion. To suppress fake electrons from jets, requirements on the transverse impact parameter d_{xy} and the relative isolation $PFRiso$ are applied. In case of electrons the PFRiso is corrected according to the so called $\rho 25$ corrections.

A symmetric photon conversion occurs in the detector material (beam pipe or tracker layers), and the d_{xy} requirement is quite sufficient ($\sim$ 50% suppression). So electrons from photon conversion have a displaced secondary vertex. And Further suppression also can be achieved by using the number of missing hits and the conversion vertex fit probability.

To avoid electrons radiated from muons, the selection with at least a $\delta R = \sqrt{\Delta\eta^2 + \Delta\Phi^2}$ >0.1 of the electron with respect to the nearest tight muon is applied.

All selection requirements for electrons are summarized in Table 6.2. The official Tag and Probe tool is used for a study of the electron identification and isolation efficiency. The result is split into the RunA, RunB, RunC and RunD datasets. The electron identification and isolation efficiency is understood well.[58] An the differences are covered by the systematic uncertainties.

6.2.4 Jet and $\not{E}_T$ selection

Jets are reconstructed using particle flow objects clustered with the anti-kt algorithm with 100 a distance parameter of δ = 0.5. And The missing transverse energy is also calculated by the PF algorithm. SUSY signal is usually originated from heavy gluino

Observable	Selection creteria
Identification	isGlobalMuonPromptTight
Particle-flow muon id	isPF
Transverse momentum p_T	$>$ 10 GeV
Pseudo rapidity $\lvert\eta\rvert$	$<$ 2.4
Number of hits in the tracker	NTrackHits $>$ 10
Global χ^2_{ndof} of the fit	$\chi^2_{ndof} < 10$
Muon chamber hits	numberOfValidMuonHits$>$ 0
Muon segments	numberOfMatchedstations$>$ 1
Number of pixel hits	numberOfValidPixelHits$>$ 0
Number of tracker layers with hits	trackerLayersWithMeasurement$>$ 5
Longitudinal impact parameter $\lvert d_z\rvert$	$\lvert d_z(PV)\rvert < 0.5$
Transverse impact parameter $\lvert d_{xy}\rvert$	$\lvert d_{xy}(PV)\rvert$< 0.02
Relative isolation PFRiso	PFRiso< 0.15

Table 6.1: The selection requirements on muon. A small impact parameter cut in applied to suppress fake muons. The well isolated muon information is required with relative isolation.

and/or squarks, resulting high hadronic activities in the events. While some SM processes like diboson productions have well isolated multiple leptons but less hadronic activities. As the isolated leptons are concerned, such events could be the main background to the analysis for isolated leptons. To remove most of those events, the scalar sum of energy of jets, H_T , is used. Only jets with a transverse momentum $p_T > 30$ GeV, pseudo rapidity $\mid \eta \mid < 2.5$ and passing the loose PFJetID critera are used for the $H_T = \Sigma_{jets} p_T^{jet}$ calculation. The distance between jets and selected electrons, muons and taus is required to be above $\Delta R > 0.4$. Jets are corrected according to the latest correction factors.[65]

6.3 Event Selection

The amount of background decreases with increasing number of prompt leptons per event, but so does the signal cross section. Hence, the cuts to suppress the SM background, like missing transverse energy and transverse energy can change with the number of prompt leptons.

The signal efficiency of the selection cuts are model dependent, e.g. an $\not{E}_T$ based analysis is more appropriate for models, where the direct chargino neutralino production is dominant and H_T is more appropriate for squark/gluino production, which results in cascade decays leading to higher jet multiplicities and so higher H_T.

Observable	Selection creteria
Transverse momentum p_T	> 10 GeV
Pseudo rapidity $\|\eta\|$	< 2.4
Transverse shape of the electromagnetic cluster	$\sigma_{\eta\eta} < 0.01$
Spatial(Φ) matching between track and supercluster	$\Delta\Phi < 0.15$
Spatial(η) matching between track and supercluster	$\Delta\eta < 0.007$
Hadronic leakage variable	HoE < 0.12
Longitudinal impact parameter $\|d_z\|$	$\|d_z(PV)\| < 0.2$
Transverse impact parameter $\|d_{xy}\|$	$\|d_{xy}(PV)\| < 0.02$
Relative isolation PFRiso	PFRiso< 0.15
Vertex fit probability	vertex fit probability $< 1e-6$
Number of missing hits in the tracker	NumberOfLostHits < 2
δR to nearest muon	$\delta R > 0.1$
Vete electrons in gap region	Vete: $1.44 <\mid \eta \mid< 1.566$

Table 6.2: Summary of the PFElectron selection requirements. Several electron ID criteria are different for the barrel ($\mid \eta \mid< 1.44$) and endcap ($1.56 <\mid \eta \mid< 2.4$) region. The latter are given in brackets. The requirements corresponds to the loose WP working point.

This study concentrates on models with dominant direct neutralino/chargino strong production with the subsequent decay of neutralino/chargino to multiple leptons(muons, electrons) in the final state.

In context of the direct neutralino/chargino production is getting the dominant process for large m_0 values, which corresponds to large squark masses. These processes are characterized by a high jet activity and high missing transverse energy. As a baseline selection we require at least three tight leptons.

6.3.1 Threshold of the triggers

The threshold of the triggers define the lower p_T cuts for the leading leptons and so each event has to pass the following requirements:

- leading muon with $p_T > 20$ GeV with next to leading muon with $p_T > 10$ GeV

where the individual thresholds were set slightly above the actual trigger thresholds to ensure a selection on the efficiency plateaus.

6.3.2 Selection of three isolated leptons

After the OSSF lepton pair has been selected, the presence of at least 3 leptons is required. As a third lepton, the muon or electron not being part of the OSSF pair and with the highest p_T is chosen. There are very few significant backgrounds from the SM with three prompt leptons originating from the hard matrix element, they all come from diboson production. However, there is a possibility that backgrounds with less than three prompt leptons pass the selection, where the third lepton comes from a misidentification of a light jet, or if a secondary lepton from a semileptonic $c-$ or $b-$quark decay passes the isolation requirements.

Considering the above, $t\tilde{t}$ and Zb are the most important backgrounds in the trilepton channel due to their high cross sections and the presence of 2 leptons plus one ore more $b-$jets. In order to select against secondary leptons from heavy quark decays, the calorimeter and track isolation have been considered to be included. In this analysis, the only event with three tight leptons in signal regions are considered, which effectively suppress the $t\tilde{t}$ background.

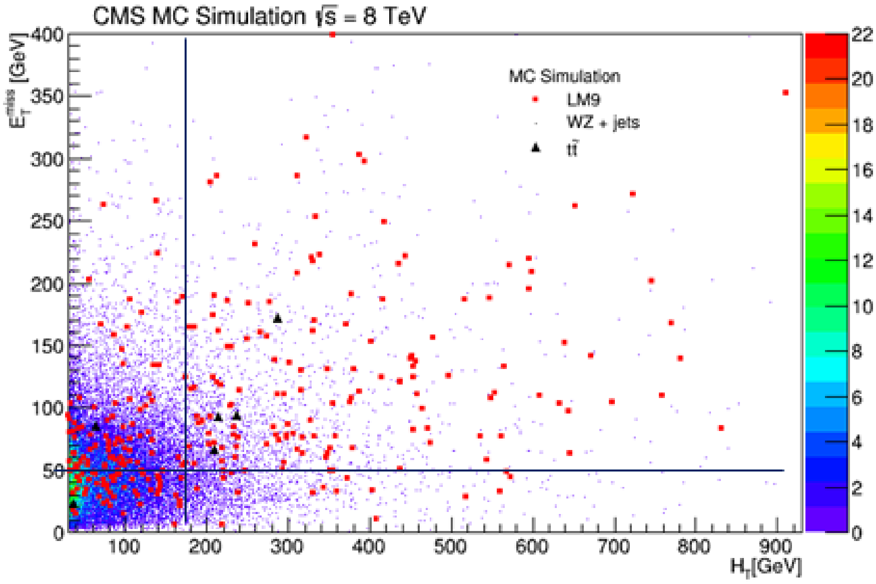

FIGURE 6.1: Distribution of missing transverse energy versus H_T for WZ, $t\tilde{t}$ and LM9 SUSY reference samples.

6.3.3 Oppeosite sign same flavour lepton pair, charge conservation

Once we have a sample of clean tri-leptons, we further require that the pairs is composed of opposite sign same flavour leptons and form zero charge in total, which helps suppress lepton pairs from heavy-flavor decays. That requirement also helps mitigate the background from low-mass Drell-Yan, a process that is not very amenable to simulation, cause of the enormous production cross-sections. After the dilepton with OSSF lepton pair is selected, only the events with three or four tight leptons is required to serve charge conservation of neutralino and chargino(neutralino) in final state. On the SUSY side, an OSSF lepton pair from neutralino decay is expected.

6.4 Data Driven Analysis

6.4.1 Search regions

The dominant SM backgrounds is from WZ, ZZ and $t\bar{t}$. The requirement on tight leptons effectively suppress the backgroud from $t\bar{t}$, but did not do that from WZ, ZZ. Therefore the data driven technique has been used to predict standard model background on large MET and various jet activity regions. Figure 6.1 shows the distribution of missing transverse and the jet activity as a function of sum of jet p_T.

6.4.2 The Un-Balanced Momentum Method

The Supersymmetry events are characterized by the large missing energy from the lightest and stable SUSY particle called LSP. That characteristics give relatively large missing transverse momentum with respect to leptons momenta. So the difference ratio of momenta between the missing transverse energy to leptons gives asymmetric distribution. The observable variable, called by ' Un-Balanced Momentum', can be simply defined as a function of the difference as following;

$$UBM = \mid E_T^{miss} \mid - \mid \Sigma p_T^l \mid \tag{6.1}$$

where p_T is the transverse memeontum of a lepton(μ, e).

The um-balanced momentum effect is shown as a distribution of UBM variable in Figure 6.2, which is from the events with $\mu\mu + \mu$. The region of under $UBM < 0$ is used to predict the SM background as a control sample, which is dominant with WZ+jets. That control region goes through the low jet activity window with $H_T < 200$ GeV. The region with $UBM > 0$ is the search regions to see SUSY signal with suppressed WZ, ZZ, $t\bar{t}$.

Similarly to $\mu\mu + \mu$ events, the UBM distributions from $\mu\mu + e$, $\mu\mu + \mu\mu$ and $\mu\mu + ee$ channels are shown in Fig 6.3, 6.4, 6.5.

6.4.2.1 Response correction

In the Un-Balanced Momemntum analysis, the response is defined as $\not{E}_T/p_T(lll)$ and is plotted as a funcion of $p_T(lll)$. The response, the ratio observation to prediction, is shown in Figure 6.6 for $\mu\mu + \mu$. The response is about 25% for MC and data. The response ratio is calibrated by weight for prediction.

This correction has a negligible effect on the final event yields, but it allows to recover the p_T variance of the UBM peak position. The effect was corrected only at the distribution level and not event by event, by finding the peak and correcting for the non-zero offset. There is 25% calibration on the effect of response between $\not{E}_T$ and p_T for $\mu\mu + \mu$. And there is 25% response calibration from $\mu\mu + e$ for MC and data. In case of four leptons, there is 0.05%(0.05%) for data, 0.09%(0.09%) for MC from $\mu\mu + \mu\mu(\mu\mu + ee)$ signatures.

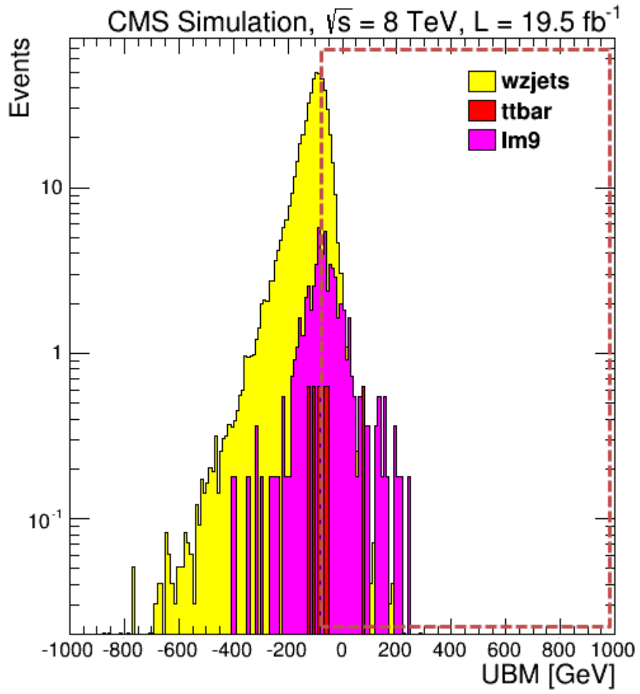

FIGURE 6.2: UBM distribution with $\mu\mu + \mu$ in WZ+jets, $t\tilde{t}$ and SUSY MC simulation, scaled to 19.5 fb^{-1}. The asymmetric distribution shows the SM dominant regions on left side and the signal dominant region on right side.

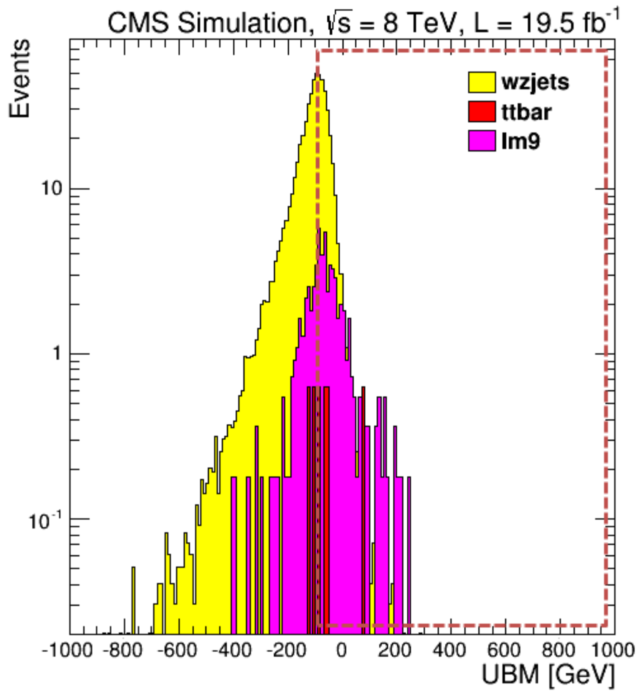

FIGURE 6.3: UBM distribution with $\mu\mu + e$ in WZ+jets, $t\tilde{t}$ and SUSY MC simulation, scaled to 19.5 fb^{-1}. The asymmetric distribution shows the SM dominant regions on left side and the signal dominant region on right side.

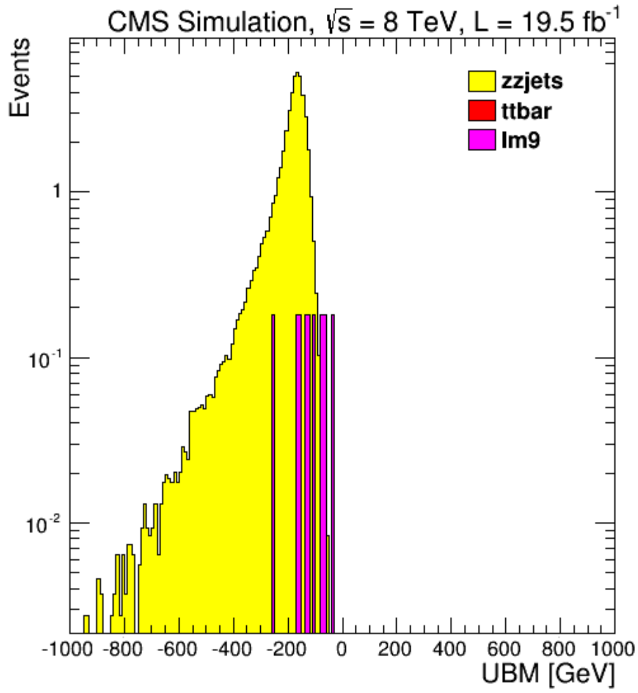

FIGURE 6.4: UBM distribution with $\mu\mu + \mu\mu$ in ZZ+jets, $t\tilde{t}$ and SUSY MC simulation, scaled to 19.5 fb−1. The asymmetric distribution shows the SM dominant regions on left side and the signal dominant region on right side.

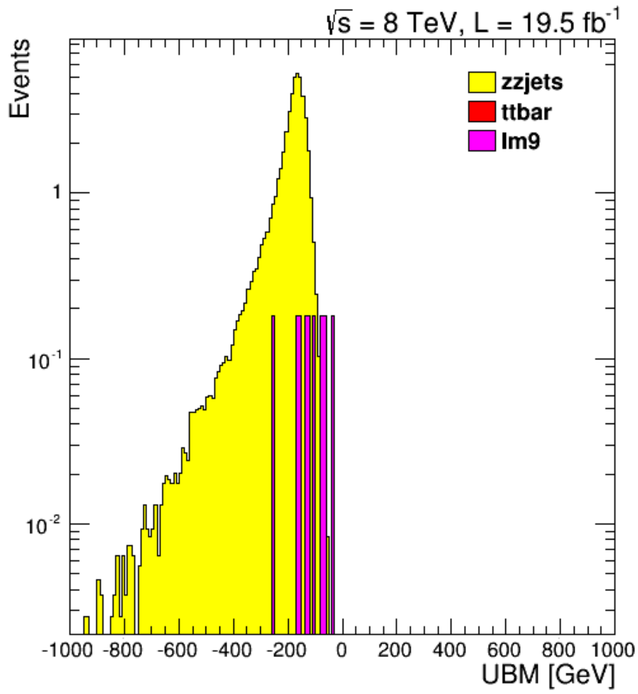

FIGURE 6.5: UBM distribution with $\mu\mu + ee$ in ZZ+jets, $t\tilde{t}$ and SUSY MC simulation, scaled to 19.5 fb−1. The asymmetric distribution shows the SM dominant regions on left side and the signal dominant region on right side.

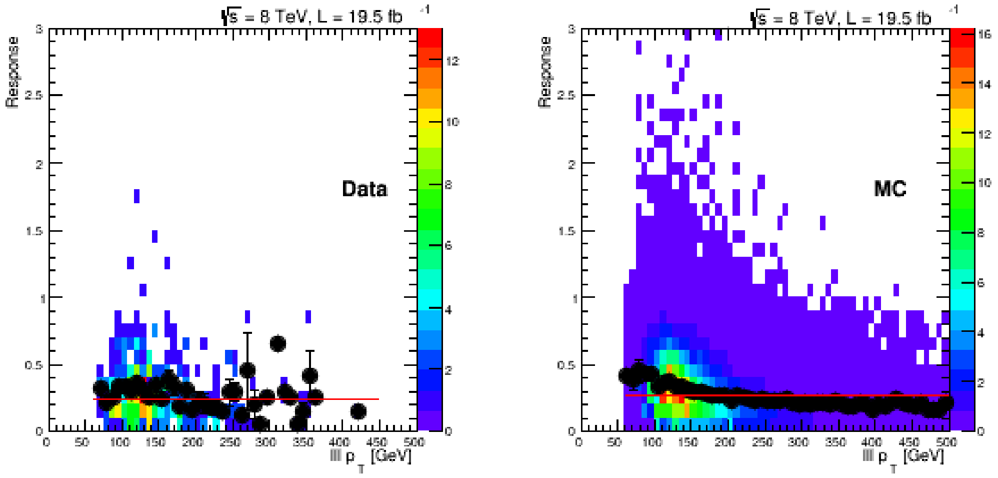

FIGURE 6.6: Response measured in data (left) and Monte Carlo simulation (right) with $\mu\mu + \mu$. 25% effect to predict the SM background.

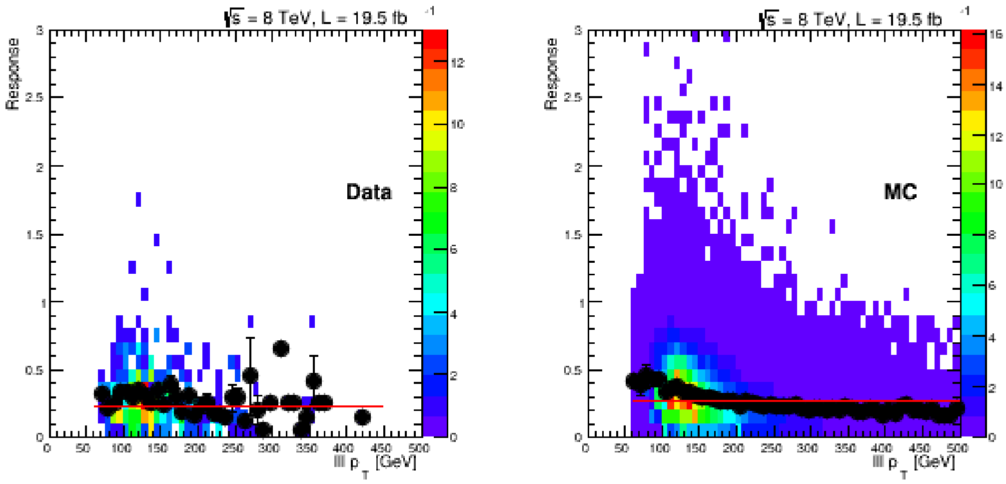

FIGURE 6.7: Response measured in data (left) and Monte Carlo simulation (right) with $\mu\mu + e$. 25% effect to predict the SM background.

The calibrated response is in Figure 6.14 $\sim$ 6.17 each for $\mu\mu + \mu(e)$, $\mu\mu + \mu\mu(ee)$. And the distribution of calibrated UBM variable has the median on zero value as shown in Figure 6.10 $\sim$ 6.13.

6.4.3 Control and signal regions

The samples are divided into $UBM < 0$ and $UBM > 0$. With these conventions, the signal region is with positive UBM to observe signal, and one control regions to predict SM background is with negative UBM. And the region with positive UBM but with low jet activity, $H_T < 200$ GeV, is the another control region to predict additional SM background.

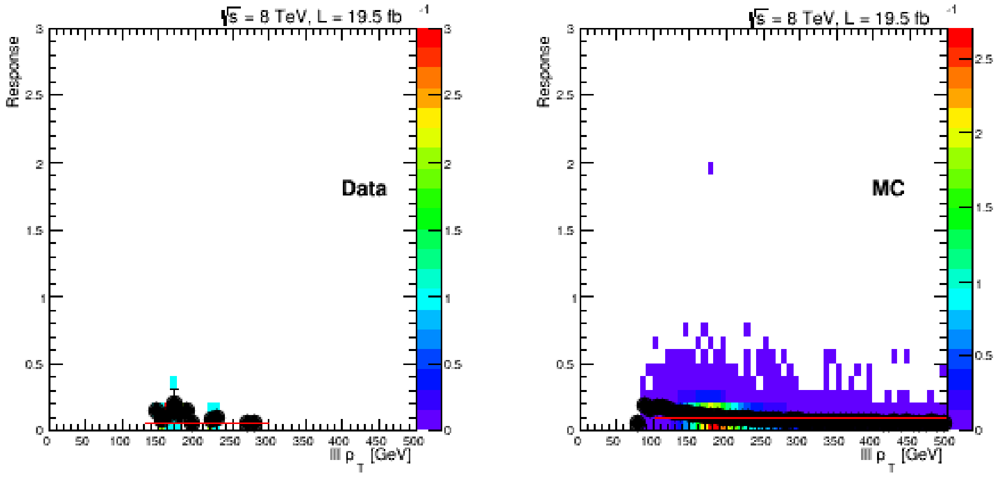

FIGURE 6.8: Response measured in data (left) and Monte Carlo simulation (right) with $\mu\mu + \mu\mu$. 25% effect to predict the SM background.

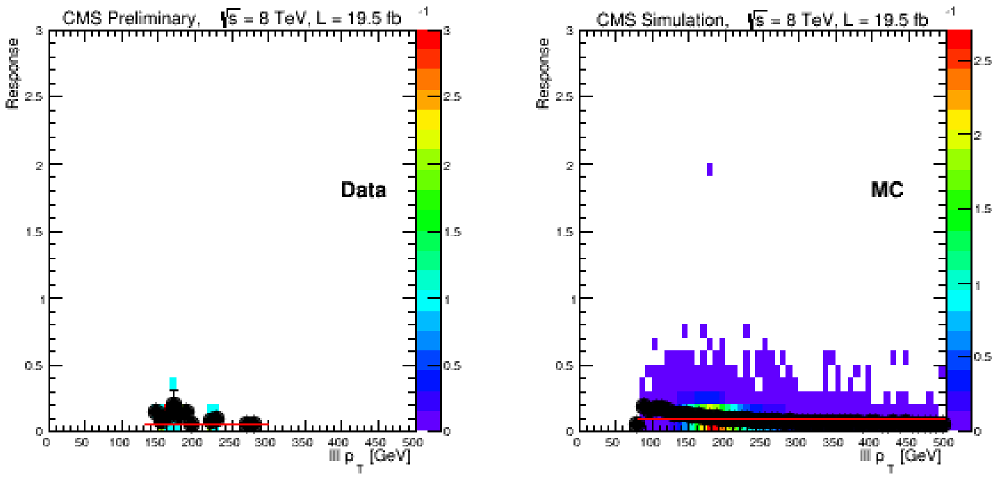

FIGURE 6.9: Response measured in data (left) and Monte Carlo simulation (right) with $\mu\mu + ee$. 25% effect to predict the SM background.

An averaged background estimation from control regions is formed as following;

$$UBM_{bkgd}^{predicted} = \mid UBM_{negative} \mid + \mid UBM_{positive}^{lowH_T} \mid, \tag{6.2}$$

And the signal observation from signal region is formed as following;

$$UBM_{signal}^{observed} = \mid UBM_{positive} \mid . \tag{6.3}$$

6.4.4 Uncertainties

The WZ(ZZ) + jets background is estimated by flipping the negative part of the UBM distribution to the positive part as described before. The main source of systematic

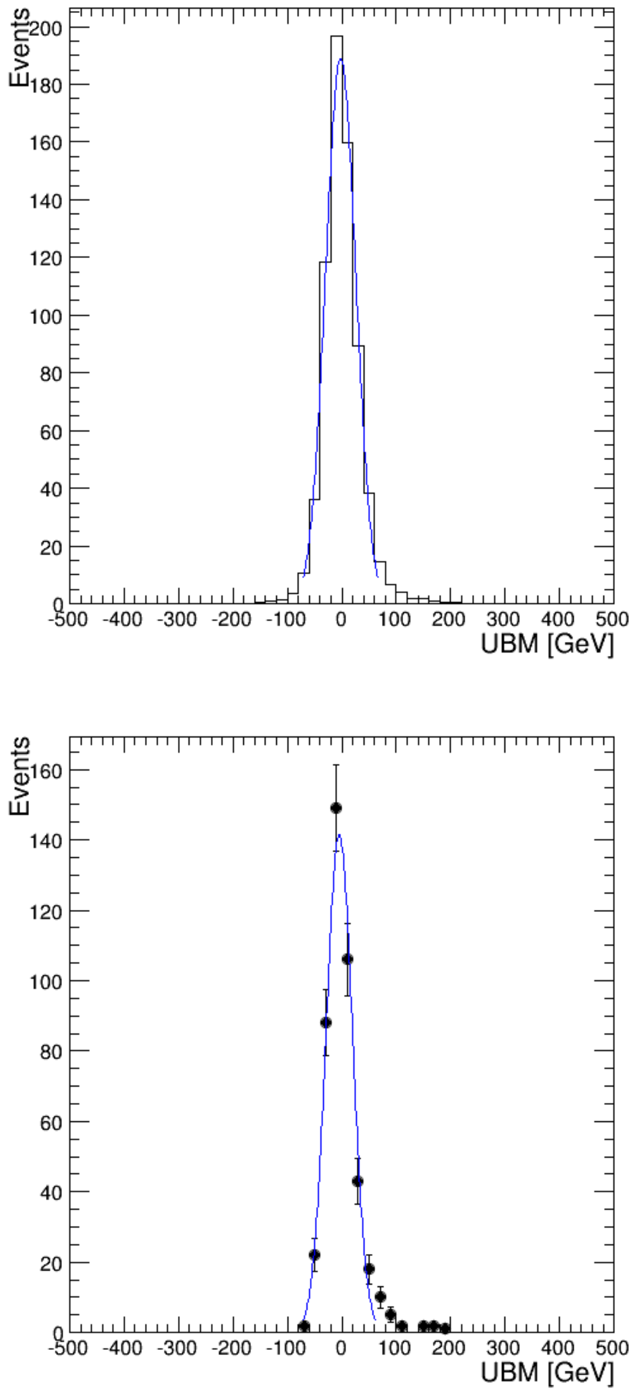

FIGURE 6.10: $\mu\mu + \mu$ channel. Calibrated UBM distribution to get Gaussian distribution with the median of distribution on zero value. The response is calibrated to be the same amount of variables met, $p_T(lll)$ for 25%.

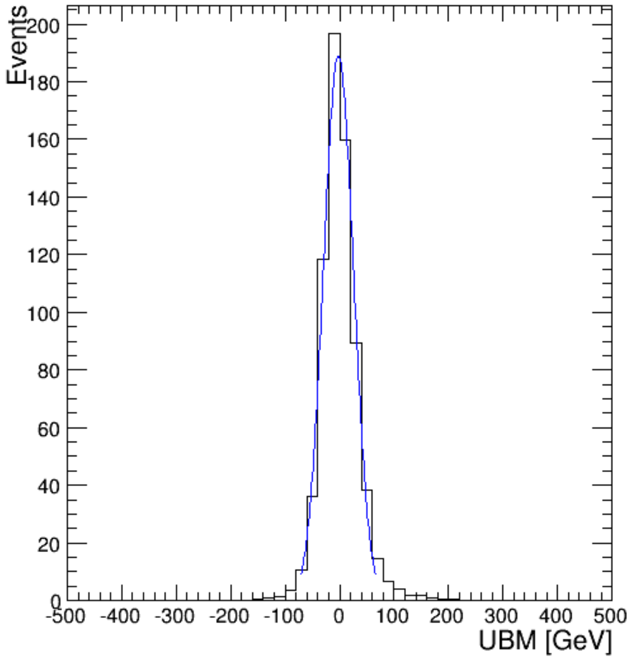

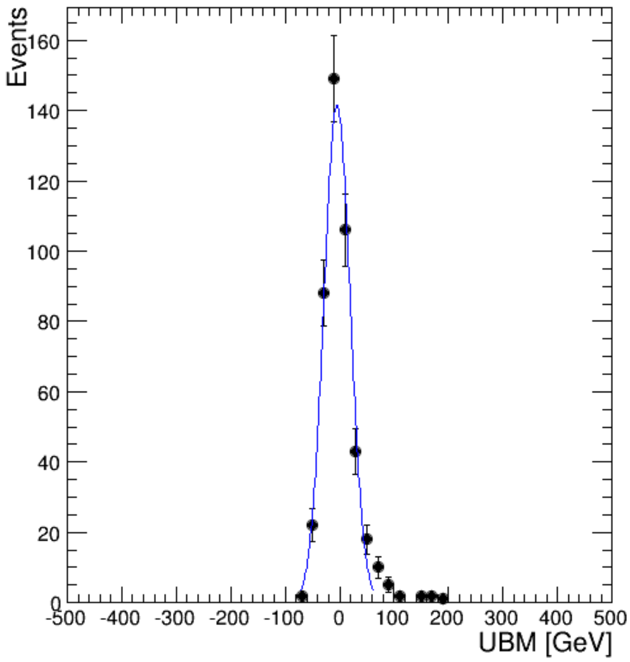

FIGURE 6.11: $\mu\mu + e$ channel. Calibrated UBM distribution to get Gaussian distribution with the median of distribution on zero value. The response is calibrated to be the same amount of variables met, $p_T(lll)$ for 25%.

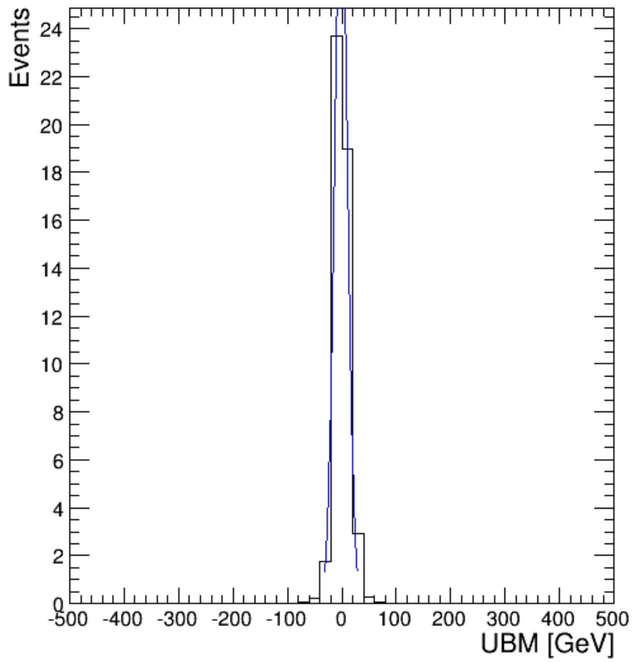

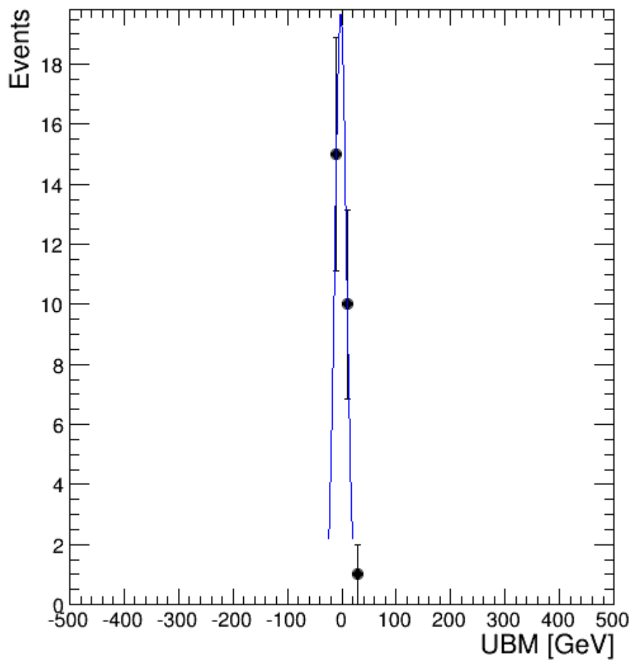

FIGURE 6.12: $\mu\mu + \mu\mu$ channel. Calibrated UBM distribution to get Gaussian distribution with the median of distribution on zero value. The response is calibrated to be the same amount of variables met, $p_T(lll)$ for 25%.

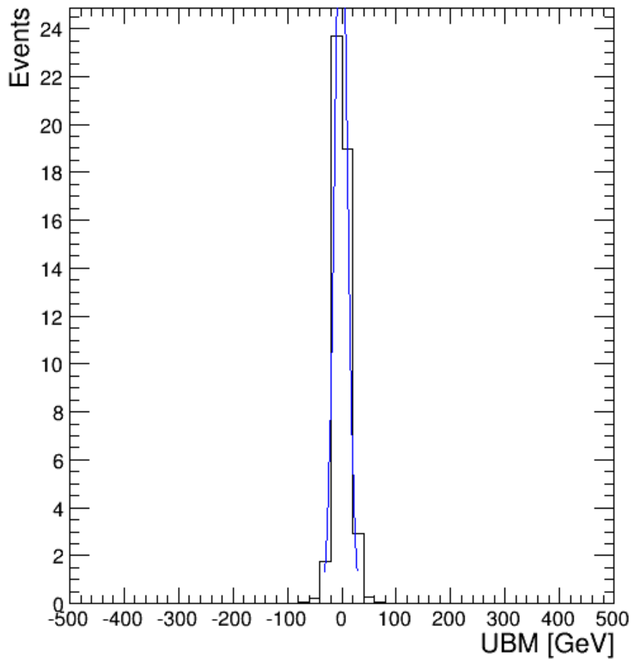

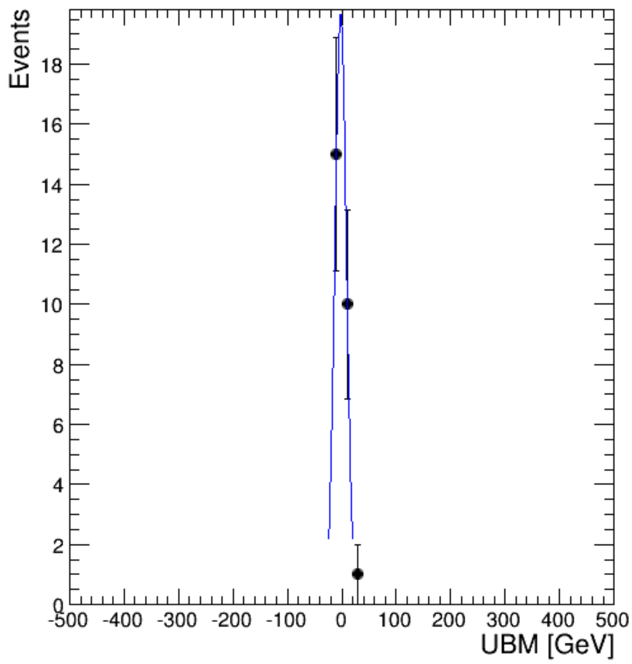

FIGURE 6.13: $\mu\mu + ee$ channel. Calibrated UBM distribution to get Gaussian distribution with the median of distribution on zero value. The response is calibrated to be the same amount of variables met, $p_T(lll)$ for 25%.

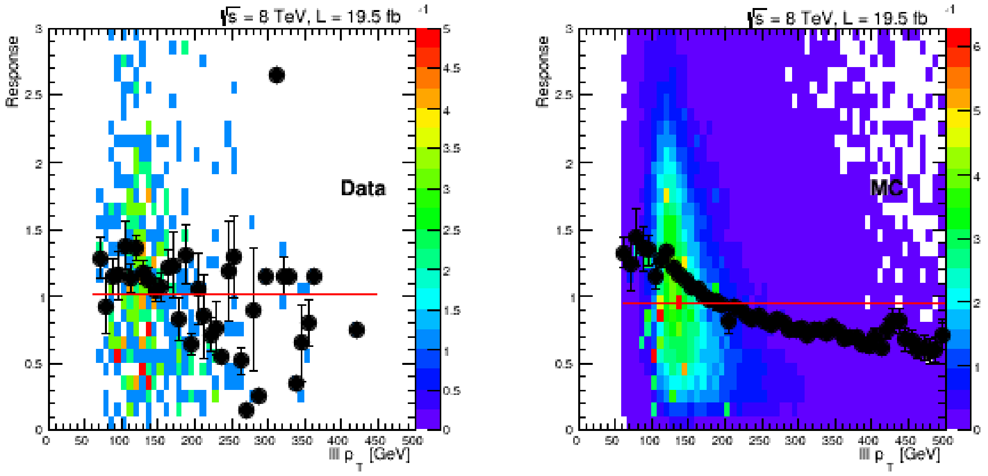

FIGURE 6.14: $\mu\mu+\mu$ channel. Calibrated response for about 25% for both of data and MC.

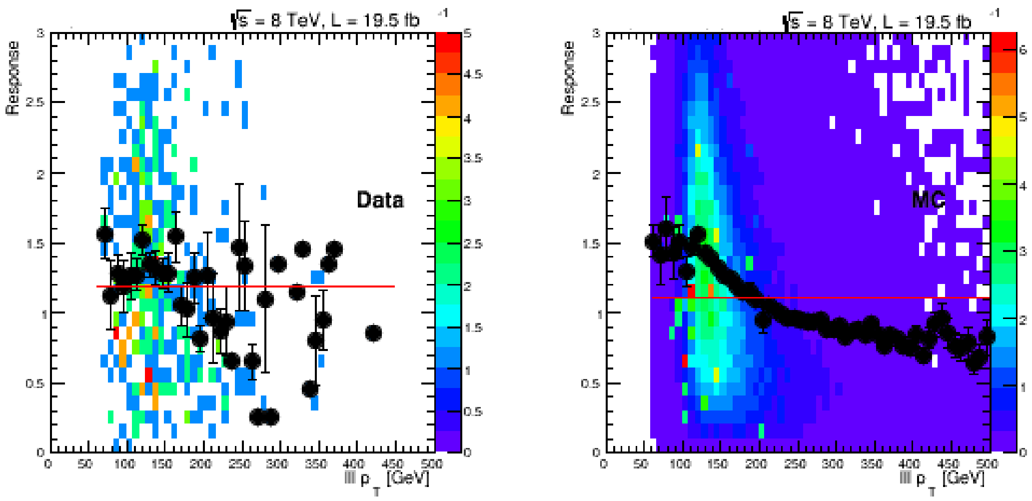

FIGURE 6.15: $\mu\mu+e$ channel. Calibrated response for about 25% for both of data and MC.

uncertainty in this method is related to asymmetries in the UBM distribution, mainly to the fact that the negative part of the UBM could be more populated due to the higher probability of undermeasureing than overmeasureing the missing energy, resulting in an overprediction of the background. To estimate this systematic uncertainty, the bin by bin ratio between the number of events in the positive and negative regions of the UBM distribution is considered in a Monte Carlo WZ(ZZ)+jets sample.

Figure 6.18 shows the comparison between the negative and the positive sides of the UBM distribution for $\mu\mu+\mu$ events and their ratio as a function of the value of UBM in the range[0,300] where Monte Carlo statistics is sufficiently high. A systematic uncertainty is the corresponding predicted number of events in order to account for the observed differences. We assign $\pm 20\%$ for $\mu\mu+\mu$ channel on the systematic uncertainties

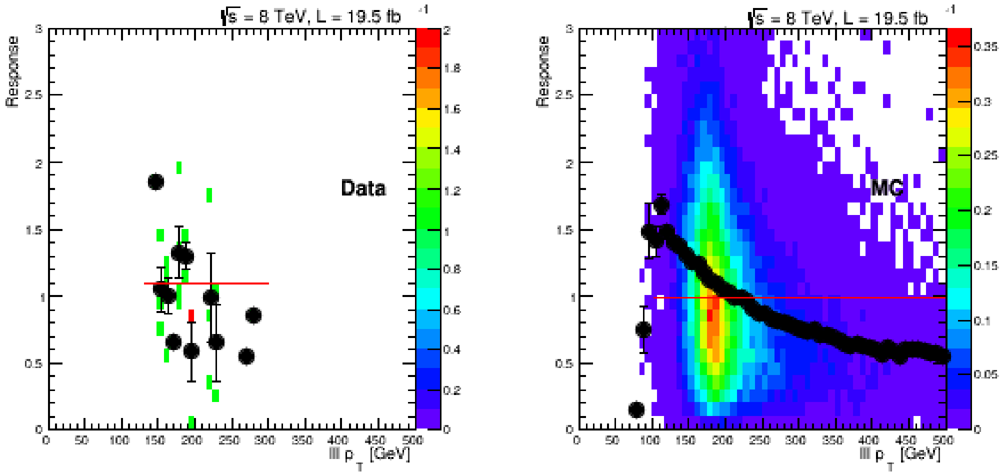

FIGURE 6.16: $\mu\mu + \mu\mu$ channel. Calibrated response for about 25% for both of data and MC.

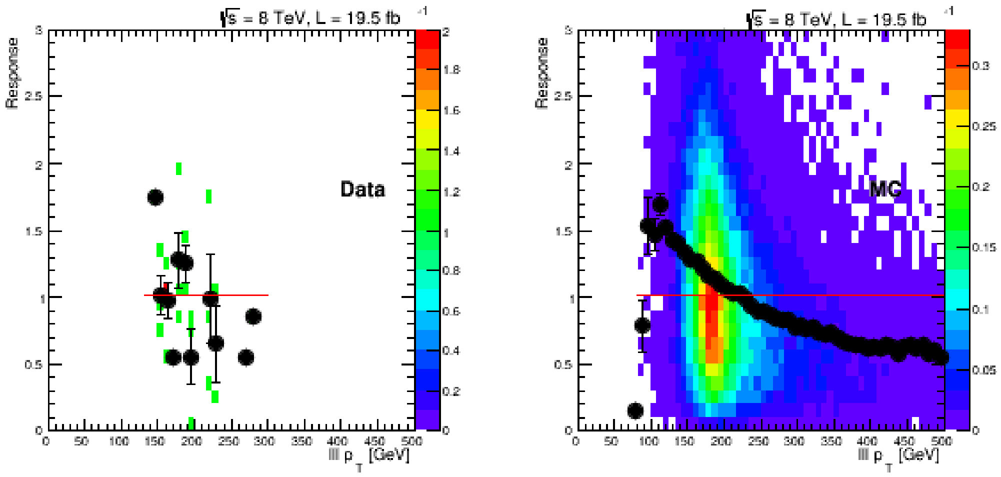

FIGURE 6.17: $\mu\mu + ee$ channel. Calibrated response for about 25% for both of data and MC.

from various UBM requirements with the data driven background estimation technique. And the systematic uncertainties for $\mu\mu + e$, $\mu\mu + \mu\mu$ and $\mu\mu + ee$ are assigned each about 20% shown in Figure 6.19 $\sim$ 6.21.

The $t\tilde{t}$ background is negligible suppressed well by quality and event selection, as shown in Fig. 6.2 before. So the background estimation is considered the most dangerous WZ, ZZ backgrounds.

6.4.5 Closure and application Test

A high-statistics Monte Carlo simulation sample is used to determine the systematic uncertainty of the background estimates. An averaged background estimation formed

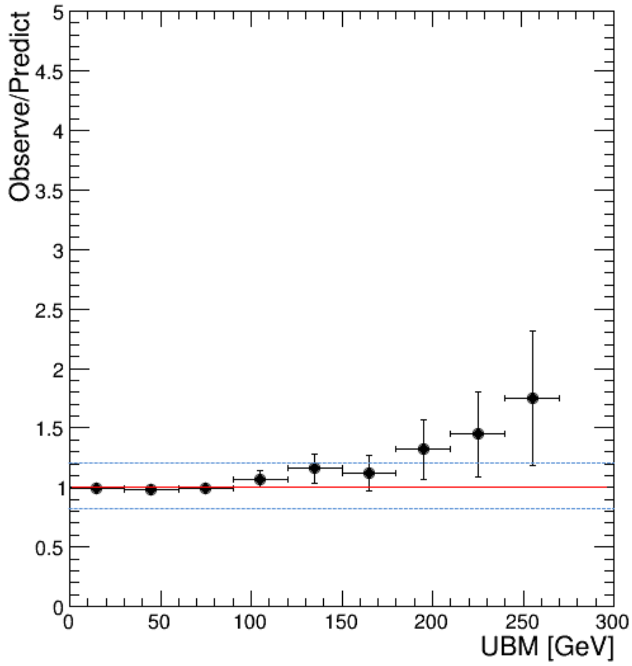

FIGURE 6.18: $\mu\mu + \mu$ channel. Systematic uncertainty is set with 20% to predict the SM background with various UBM requirements.

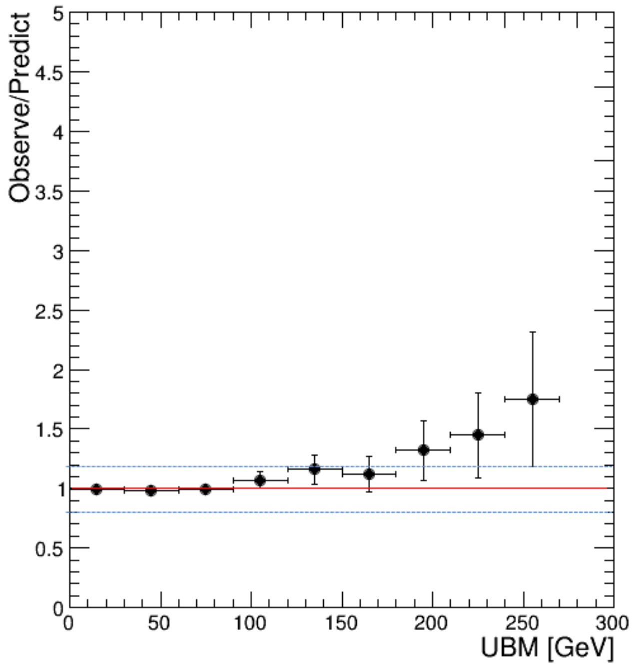

FIGURE 6.19: $\mu\mu + e$ channel. Systematic uncertainty is set with 20% to predict the SM background with various UBM requirements.

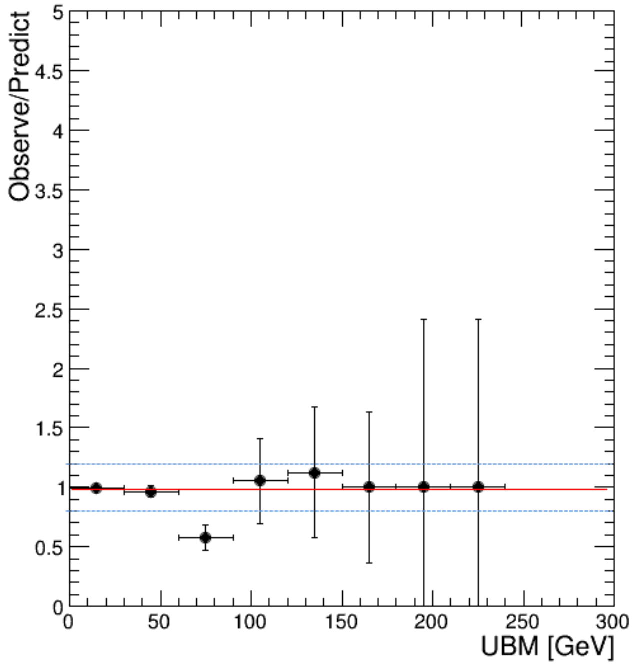

FIGURE 6.20: $\mu\mu + \mu\mu$ channel. Systematic uncertainty is set with 20% to predict the SM background with various UBM requirements.

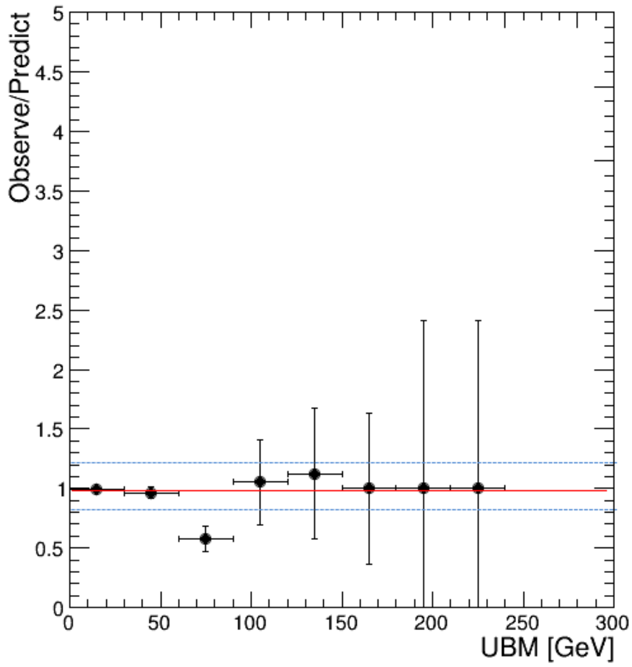

FIGURE 6.21: $\mu\mu + ee$ channel. Systematic uncertainty is set with 20% to predict the SM background with various UBM requirements.

as

$$UBM_{bkgd}^{pred} = \mid UBM_{negative} \mid + \mid UBM_{positive}^{lowH_T} \mid \tag{6.4}$$

is accompanied with a 20% systematic uncertainty assessed from Monte Carlo simulation as discussed on section before.

The comparison between the SM prediction,

$$UBM_{bkgd}^{predicted}, \tag{6.5}$$

and the signal observation,

$$UBM_{signal}^{observed}, \tag{6.6}$$

shows how the data-driven technique works for Standard Model and Supersymmetry scenarios.

The predicted SM background from the control region with $UBM < 0$ is estimated with varying UBM requirement and the comparison with the observed SM background is shown as Table 6.3 from the $\mu\mu + \mu$ channel. The table presents the integrated numbers in the SM background only hypothesis. The uncertainties on the MC expectations reflect the limited Monte Carlo statistics.

The agreement of the individual background predictions gives confidence in the final background estimation. A complete SM Monte Carlo closure test is performed using the total background estimation. Fig. 6.22 from the $\mu\mu + \mu$ channel shows the comparison between predicted and observed distributions in Monte Carlo simulation samples in the SM background only hypothesis. And the bottom plots show the ratio between observed and predicted distributions. Additional closure tests for $\mu\mu + e$, $\mu\mu + \mu\mu$ and $\mu\mu + ee$ channels shows that the method UBM works well for Standard Model as in the result Table 6.4 $\sim$ 6.6, and in Figure 6.23 $\sim$ 6.25.

Region(SM only)	MC predicted	MC observed
UBM > 0	318.4 ± 94.3	318
UBM > 10	225.3 ± 67.9	225.6
UBM > 20	158.6 ± 44.7	159.0
UBM > 30	104.8 ± 26.0	105.9
UBM > 40	67.9 ± 15.7	69.8
UBM > 60	29.9 ± 7.0	31.6
UBM > 90	11.3 ± 3.6	13.3

TABLE 6.3: $\mu\mu + \mu$ channel. Result table of comparison of predicted and observed distributions in only SM MC simulation without SUSY signal sample.

As the data driven technique using UBM variable works well to predict SM background as discussed before. The closure test is also repeated by mixing the LM9

SUSY(mSUGRA) benchmark signal and performing a signal+background hypothesis test in order to demonstrate that a signal will not be missed and calibrated away by the control regions. The results of closure test for MC with signal sample are shown in Fig. 6.23 for $\mu\mu + \mu$ The UBM method predict also well signal events with three($\mu\mu + \mu(e)$) and more leptons($\mu\mu + \mu\mu(ee)$) as shown in Fig. 6.23 $\sim$ 6.29. The observed events are much more than the predicted on large UBM regions.

Region(SM only)	MC predicted	MC observed
UBM $>$ 0	1319.93 $\pm$ 344.669	1319.02
UBM $>$ 10	742.254 $\pm$ 182.27	753.914
UBM $>$ 20	368.038 $\pm$ 72.7379	371.711
UBM $>$ 30	135.547 $\pm$ 32.0787	134.353
UBM $>$ 40	77.1345 $\pm$ 18.9388	73.2452
UBM $>$ 60	24.1254 $\pm$ 9.28153	24.4744
UBM $>$ 90	7.02689 $\pm$ 3.74826	7.94786

Table 6.4: $\mu\mu + e$ channel. Result table of comparison of predicted and observed distributions in only SM MC simulation without SUSY signal sample)

Region(SM only)	MC predicted	MC observed
UBM $>$ 0	22.4525 $\pm$ 7.96712	22.2697
UBM $>$ 10	10.4571 $\pm$ 4.0265	10.8826
UBM $>$ 20	4.25819 $\pm$ 2.15699	4.73166
UBM $>$ 30	2.02946 $\pm$ 1.4637	2.50293
UBM $>$ 40	0.421751 $\pm$ 0.660136	0.365456
UBM $>$ 60	0.113513 $\pm$ 0.342323	0.0802896
UBM $>$ 90	0.0313775 $\pm$ 0.181958	0.0332233

Table 6.5: $\mu\mu + \mu\mu$ channel. Result table of comparison of predicted and observed distributions in only SM MC simulation without SUSY signal sample)

Region(SM only)	MC predicted	MC observed
UBM $>$ 0	22.4958 $\pm$ 7.95745	11
UBM $>$ 10	9.54615 $\pm$ 3.8602	9.44556
UBM $>$ 20	3.33986 $\pm$ 1.91139	3.2891
UBM $>$ 30	1.11483 $\pm$ 1.08155	2.50478
UBM $>$ 40	0.416214 $\pm$ 0.656307	0.365456
UBM $>$ 60	0.102438 $\pm$ 0.326281	0.0793667
UBM $>$ 90	0.0304547 $\pm$ 0.179403	0.0332233

Table 6.6: $\mu\mu + ee$ channel. Result table of comparison of predicted and observed distributions in only SM MC simulation without SUSY signal sample)

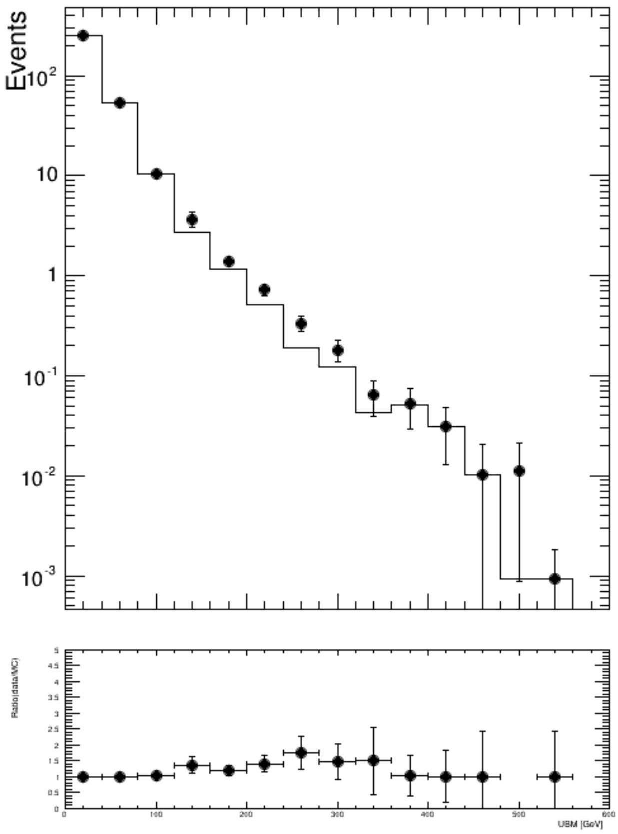

FIGURE 6.22: $\mu\mu + \mu$ channel. MC closure test with signal events. The method with UBM variable works well to predict the SM background corresponding observation. The difference between observation and SM prediction remains as a signal on search region.

Region(LM9)	MC predicted	MC observed
UBM > 0	348.8 ± 97.5	368
UBM > 10	249.1 ± 69.6	269.2
UBM > 20	176.7 ± 45.9	196.3
UBM > 30	119.5 ± 26.7	136.9
UBM > 40	79.5 ± 16.2	97.5
UBM > 60	35.8 ± 7.4	50.9
UBM > 90	15.1 ± 4.1	26.9

TABLE 6.7: Result table of comparison of predicted and observed distributions in SM MC simulation with SUSY signal sample)

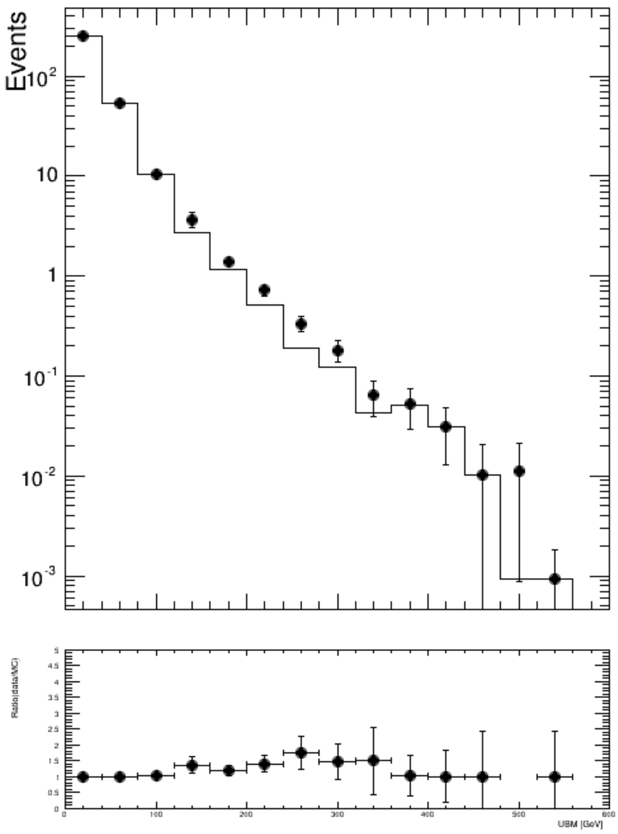

FIGURE 6.23: $\mu\mu + e$ channel. MC closure test with signal events. The method with UBM variable works well to predict the SM background corresponding observation. The difference between observation and SM prediction remains as a signal on search region.

6.5 Systematic uncertainties

The systematic uncertainties are considered in two main categories of theoretical and instrumental sources.

The main contributions to theoretical uncertainties are associated with the QCD coupling scale and the protons parton distribution function(PDF). These uncertainties can affect the cross-section calculation, also do the expected signal acceptance. Generally we will ultimately constrain models of new physics in terms of $\sigma \times BR$, and we are absolved from having to evaluate the cross-section uncertainties. The uncertainties leading to changes are expected to be very small in the signal acceptance. And that can be estimated using an ensemble of different theory PDFs to generate the signal models. This has been done on previous SUSY analyses based on strong production, and found to range from 0 to 2% [55]. Therefore we take 2% as a conservative upper bound.

The theoretical uncertainties mainly come from:

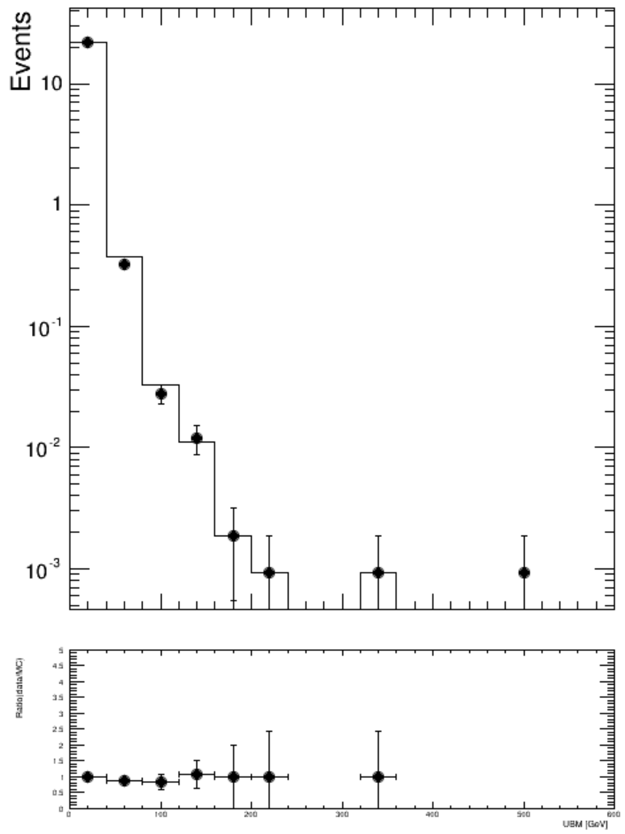

FIGURE 6.24: $\mu\mu + \mu\mu$ channel. MC closure test with signal events. The method with UBM variable works well to predict the SM background corresponding observation. The difference between observation and SM prediction remains as a signal on search region.

- PDF $+\alpha_S$, on the parton distribution functions $f_{p_i}(x_i, M^2)$ and in the coupling $\alpha_S(M^2)$

- QCD scal uncertainty, linkded to the choice of QCD renomalization and factorization scales(μ_R and μ_F)

The instrumental uncertainties are considered as follows:

- integrated luminosity: 4.5% for 8 TeV data. We conform to the standard from the official luminosity measurement on CMS.

- Trigger Uncertainties: 2% for dilepton trigger. There are many studies on trigger uncertainties. The dilepton triggers from the Higgs study were used in this analysis. We assume 100% efficiency with a 2% uncertainty on this for the three-lepton case. In the three-lepton case, there are 3 objects to fire the two parts of the

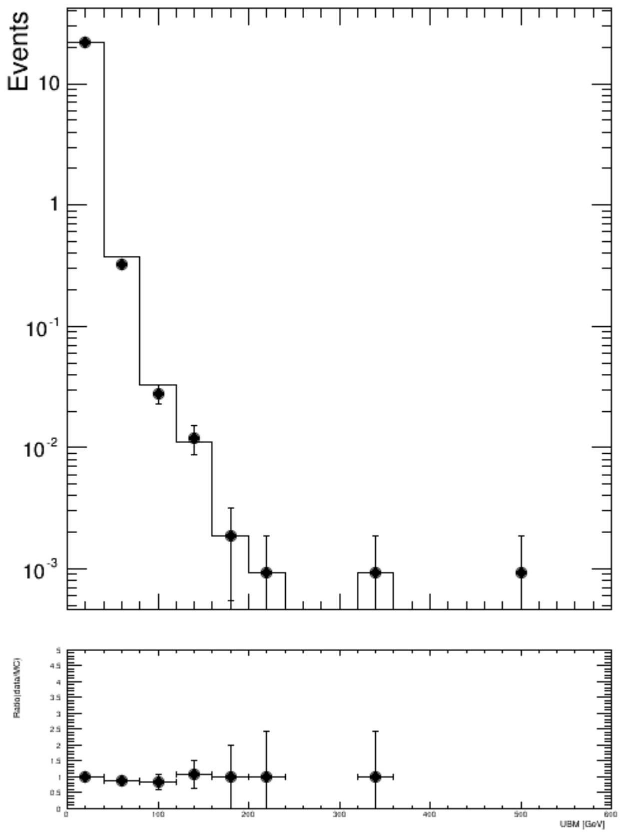

FIGURE 6.25: $\mu\mu + ee$ channel. MC closure test with signal events. The method with UBM variable works well to predict the SM background corresponding observation. The difference between observation and SM prediction remains as a signal on search region.

trigger. The probability that the dilepton trigger is fired in a trilepton event is:

$$P(trigger) = pass^3 + 3 \times pass^2 \times (1 - pass), \tag{6.7}$$

with pass the per-leg trigger efficiency, 95% for muons and 98% electrons [61]. The per-leg trigger efficiency 95%(98%) gives 99.3%(99.9%), so we assume 100% efficiency with a 2% uncertainty for the three-lepton case.

- ID/isolation: 9%. The identification and isolation efficiency is calculated in data in $Z \to l^+l^-$ events as a function of p_T and h using the tag and probe method. The reconstruction efficiency is measured by the EGamma [58] and Muon POG [59][60].

  The identification and isolation efficiencies for data and MC are shown in Figure 6.30 and Figure 6.31, 6.32 for electrons and muons respectively. All of the efficiencies agree within 2% between data and MC.

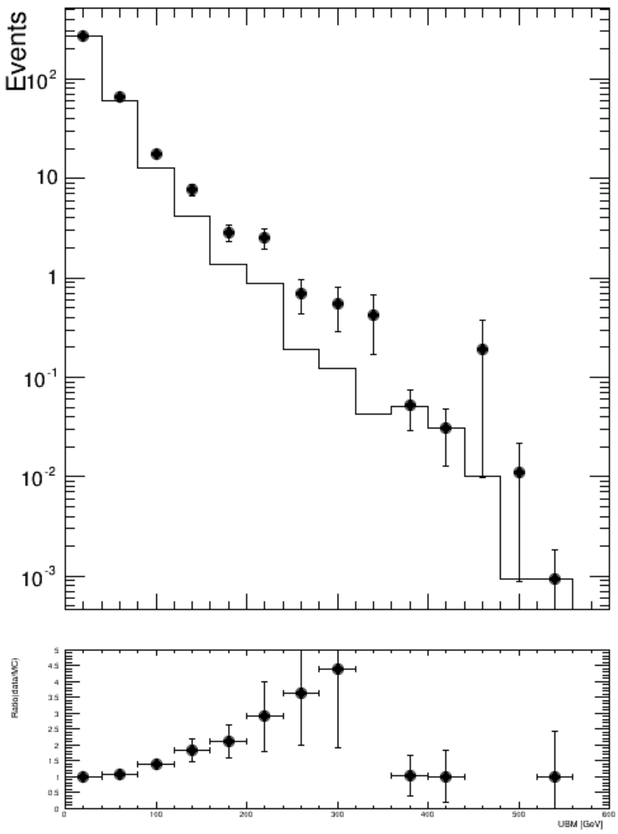

FIGURE 6.26: $\mu\mu + \mu$ channel. Application with signal events. The method with UBM variable works well to predict the SM background corresponding observation. The difference between observation and SM prediction remains as a signal on search region.

Due to possible background contamination, imperfect choice of signal and background shapes, and possible misunderstanding of the correlation between the identification and isolation variables, a 3% systematic uncertainty per lepton is assigned to the efficiency measurement. This will lead to a 9% uncertainty on the signal yield since this uncertainty is taken correlated for the same lepton flavor.

- Jet Energy Scale: 10%, for the uncertainty in the hadronic energy scale affects jet counting. The effect on the jet selection is estimated by varying the jet energy scale by a conservative ±5% [65] and taking the variation in the selection efficiency as a systematic uncertainty. So the uncertainty 10% is considered in this study. The effect of the energy scale uncertainty is ±5%, corresponds to the $\not{E}_T$ resolution difference between data and MC simulation [66].

A summary of the systematic uncertainties associated with the signal acceptance for this analysis is provided in Table 6.8. When a signal model of interest, the final state

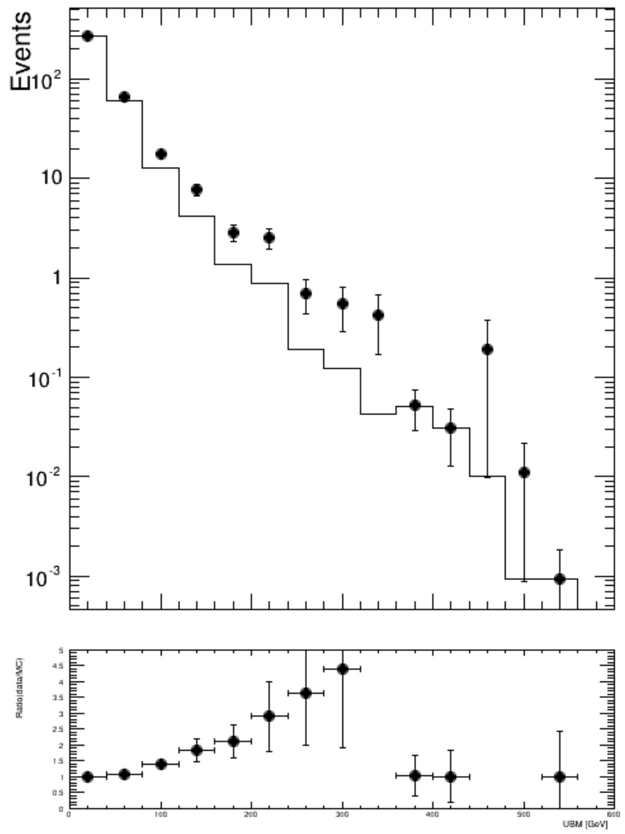

FIGURE 6.27: $\mu\mu + e$ channel. Application with signal events. The method with UBM variable works well to predict the SM background corresponding observation. The difference between observation and SM prediction remains as a signal on search region.

topologies and kinematics are specified, a few uncertainties can only be quantified. A lower bound on the signal acceptance uncertainty of 15% is given for this analysis.

Source	Uncertainty
Theoretical Uncertainty	2%
Luminosity	4.5%
Triger	2%
Modeling of lepton reco, Id, isolation based on Z-events	9%
Jet Energy Scale	10%
Min. Systematic Error	15%

TABLE 6.8: Summary of systematic uncertainties for the signal acceptance

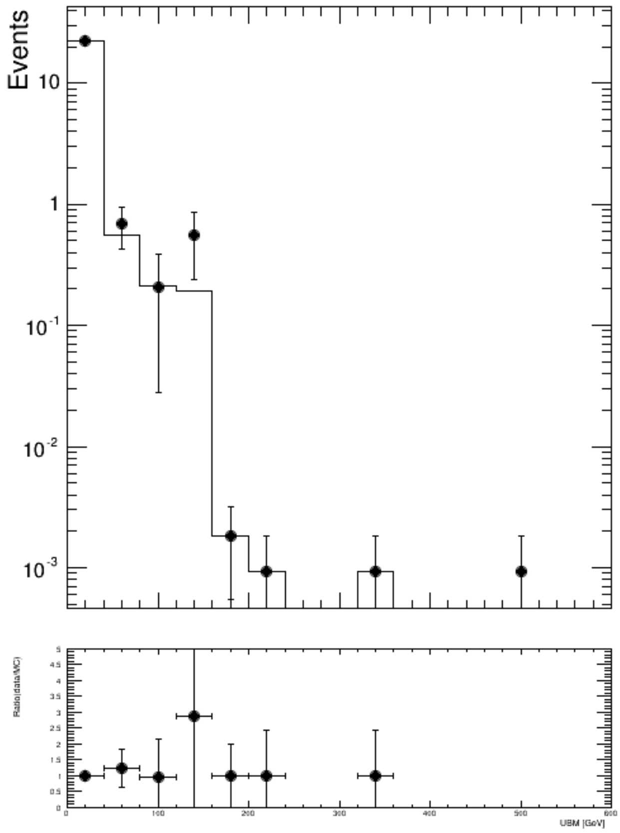

FIGURE 6.28: $\mu\mu + \mu\mu$ channel. Application with signal events. The method with UBM variable works well to predict the SM background corresponding observation. The difference between observation and SM prediction remains as a signal on search region.

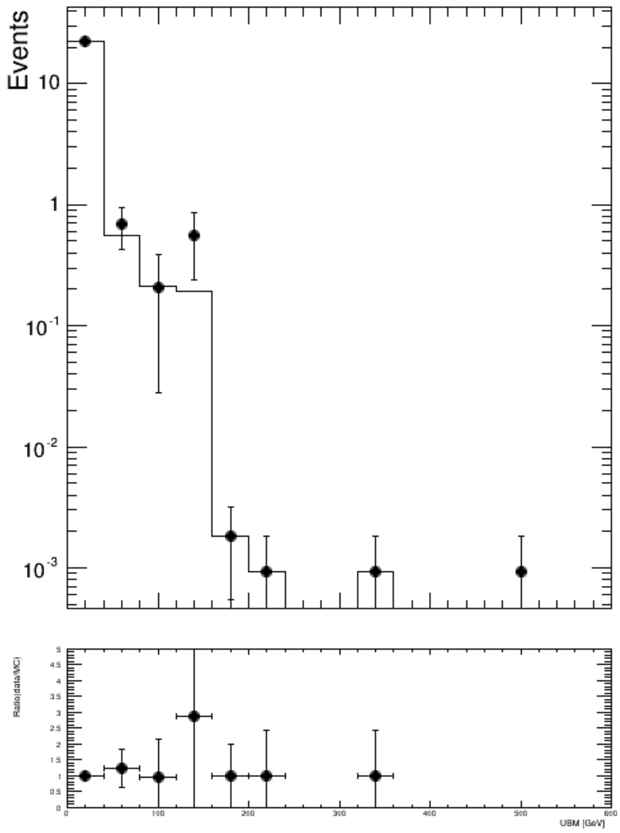

FIGURE 6.29: $\mu\mu + ee$ channel. Application with signal events. The method with UBM variable works well to predict the SM background corresponding observation. The difference between observation and SM prediction remains as a signal on search region.

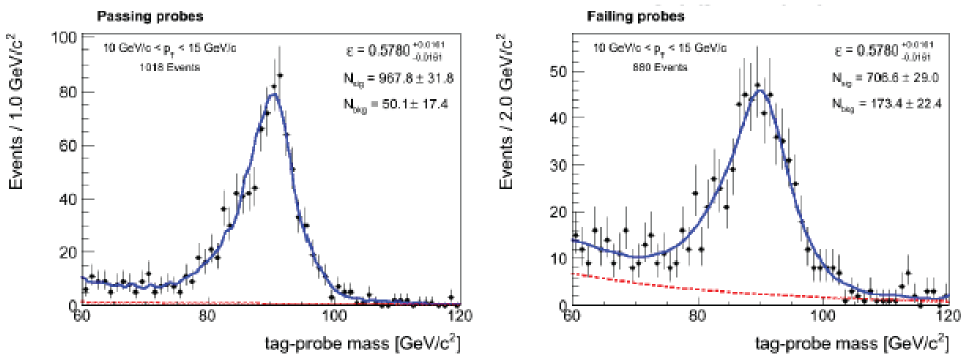

FIGURE 6.30: Fit to the passing (left) and failing (right) sample for the electron identification efficiency with 10 GeV $< p_T <$ 15 GeV.

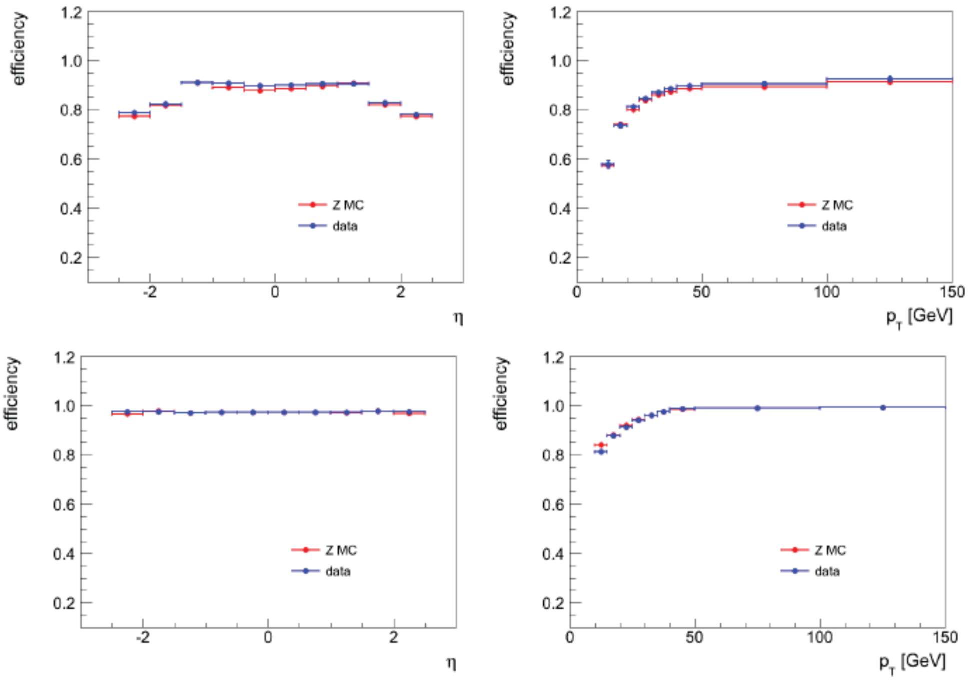

FIGURE 6.31: Identification (top) and isolation (bottom) efficiency for electrons as a function of pseudo-rapidity (left) and transverse momentum (right).

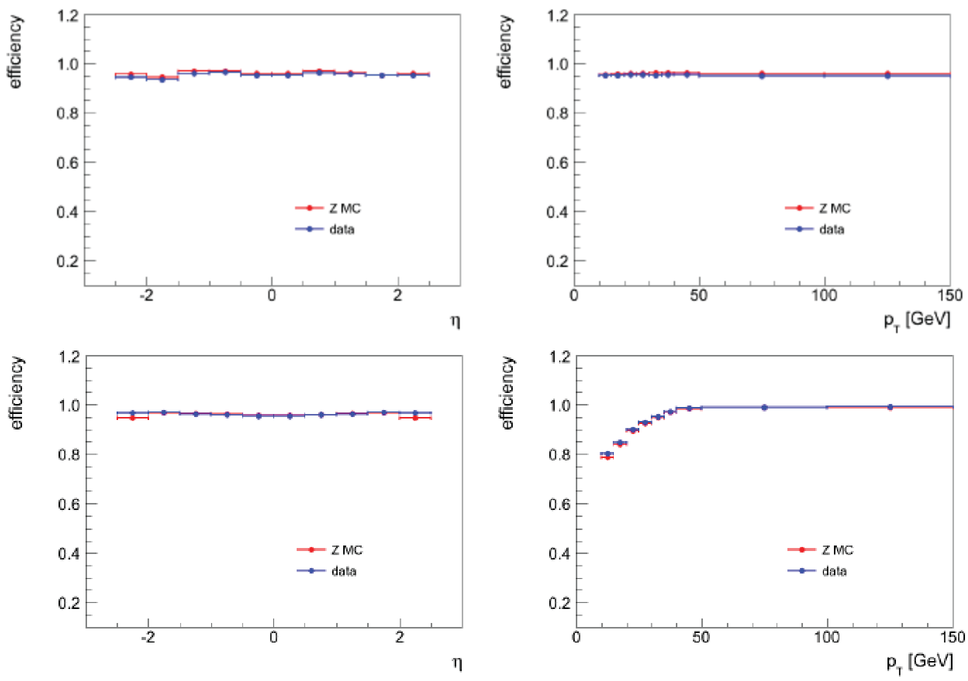

FIGURE 6.32: Identification (top) and isolation (bottom) efficiency for muon as a function of pseudo-rapidity (left) and transverse momentum (right).

Chapter 7

Results of the Search

7.1 Results

The UBM distribution for the tri-leptons signatures, $\mu\mu + \mu(e)$ is shown in Fig. 7.1. The characteristic UBM shape of WZ+jets processes is clearly visible. The observed UBM distribution in the search region is compared to that expected from Monte Carlo simulation. Results of comparison between the predicted events from control region and the observed events from signal region is shown in Table 7.1 $\sim$ 7.4. The results from collision data includes four leptons as well as three leptons.

Jet inclusive	$\mu\mu + \mu$	
Region($\mu\mu + \mu$)	Predicted	Observed
UBM > 0	186 $\pm$ 13.6382(stat) $\pm$ 65.2141(syst)	189 $\pm$ 113.7477(stat)
UBM > 10	119 $\pm$ 10.9087(stat) $\pm$ 46.2054(syst)	124 $\pm$ 11.1355(stat)
UBM > 20	78 $\pm$ 8.83176(stat) $\pm$ 27.962(syst)	83 $\pm$ 9.11043(stat)
UBM > 30	52 $\pm$ 7.2111(stat) $\pm$ 11.7633(syst)	58 $\pm$ 7.61577(stat)
UBM > 40	33 $\pm$ 5.74456(stat) $\pm$ 6.04669(syst)	40 $\pm$ 6.32456(stat)
UBM > 60	16 $\pm$ 4(stat) $\pm$ 1.06066(syst)	22 $\pm$ 4.69042(stat)
UBM > 90	4 $\pm$ 2(stat) $\pm$ 0.5(syst)	8 $\pm$ 2.82843(stat)

TABLE 7.1: Result table for $\mu\mu + \mu$ signature, jet inclusive from data. Total number of events observed in the search regions, and corresponding background predictions. The uncertainty includes the statistical and systematic.

And Table 7.5 shows the comparison between predicted and observed events with at least three jets, by which requires varying UBM value from 0 to 90.

As a results from the data-driven background prediction method, there is no excess beyond the standard model. So the data gives agreement to the expectation of the Standard Model.

Jet inclusive	$\mu\mu + e$	
Region($\mu\mu + \mu$)	Predicted	Observed
UBM > 0	573 ± 23.9374(stat) ± 159.987(syst)	568 ± 23.8328(stat)
UBM > 10	324 ± 18(stat) ± 87.241(syst)	318 ± 17.8326(stat)
UBM > 20	165 ± 12.8452(stat) ± 35.5202(syst)	157 ± 12.53(stat)
UBM > 30	74 ± 8.60233(stat) ± 14.2872(syst)	67 ± 8.18535(stat)
UBM > 40	40 ± 6.32456(stat) ± 7.78621(syst)	37 ± 6.08276(stat)
UBM > 60	15 ± 3.87298(stat) ± 2.79508(syst)	14 ± 3.74166(stat)
UBM > 90	6 ± 2.44949(stat) ± 0.866025(syst)	5 ± 2.23607(stat)

Table 7.2: Result table for $\mu\mu + e$ signature, jet inclusive from data. Total number of events observed in the search regions, and corresponding background predictions. The uncertainty includes the statistical and systematic.

Jet inclusive	$\mu\mu + \mu\mu$	
Region($\mu\mu + \mu$)	Predicted	Observed
UBM > 0	10 ± 3.16228(stat) ± 3.7081(syst)	11 ± 3.31662(stat)
UBM > 10	4 ± 2(stat) ± 1(syst)	4 ± 2(stat)
UBM > 20	3 ± 1(stat) ± 0.25(syst)	1 ± 1(stat)
UBM > 30	1 ± 1(stat) ± 0.25(syst)	1 ± 1(stat)
UBM > 40	0	0
UBM > 60	0	0
UBM > 90	0	0

Table 7.3: Result table for $\mu\mu + \mu\mu$ signature, jet inclusive from data. Total number of events observed in the search regions, and corresponding background predictions. The uncertainty includes the statistical and systematic.

Jet inclusive	$\mu\mu + ee$	
Region($\mu\mu + \mu$)	Predicted	Observed
UBM > 0	10 ± 3.16228(stat) ± 3.7081(syst)	11 ± 3.31662(stat)
UBM > 10	4 ± 2(stat) ± 1(syst)	4 ± 2(stat)
UBM > 20	3 ± 1(stat) ± 0.25(syst)	1 ± 1(stat)
UBM > 30	1 ± 1(stat) ± 0.25(syst)	1 ± 1(stat)
UBM > 40	0	0
UBM > 60	0	0
UBM > 90	0	0

Table 7.4: Result table for $\mu\mu + ee$ signature, jet inclusive from data. Total number of events observed in the search regions, and corresponding background predictions. The uncertainty includes the statistical and systematic.

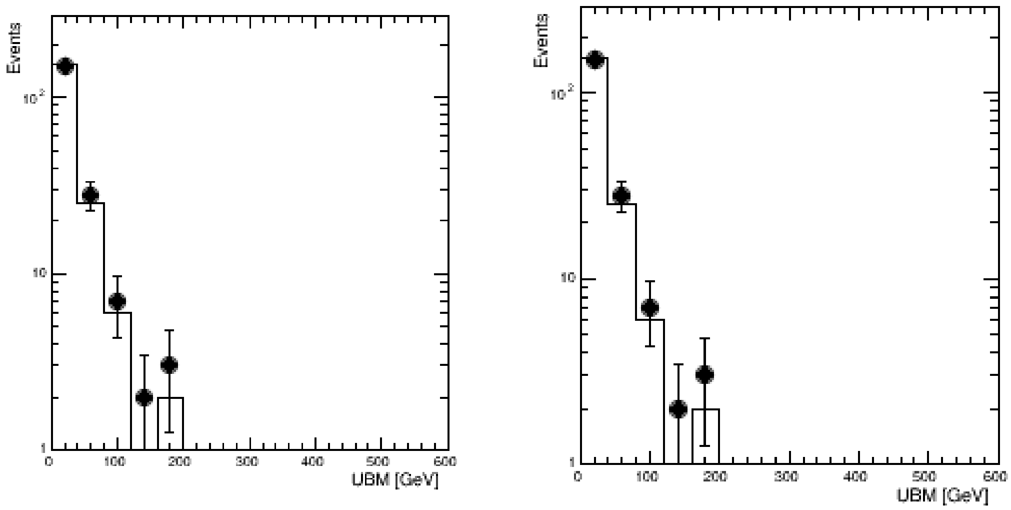

FIGURE 7.1: $\mu\mu + \mu$ channel(left), $\mu\mu + e$ channel(right). Result for SM prediction from control region and observation from signal region from data.

7.2 Limits on physics beyond the standard model

We calculate upper limits on the cross sections for the pair production of charginos, neutralinos, and sleptons. The 95% confidence level (CL) upper limits are computed by using the CLs method [67][68][69]. And we use the NLO cross section from Ref. [70][71][72] to evaluate 95%CL exclusion curves and their standard deviation(s) uncertainty. In addition, we display the median expected exclusion limits on the $\mu\mu + \mu(e)$ and $\mu\mu + \mu\mu(ee)$for GMSB higgsino.

N Jet ≥ 3	$\mu\mu + \mu$		$\mu\mu + e$	
Region($\mu\mu + \mu$)	Predicted	Observed	Predicted	Observed
UBM > 0	14 ± 5.6(tot)	16	38 ± 8.3(tot)	39
UBM > 10	12 ± 4.3(tot)	15	24 ± 5.9(tot)	24
UBM > 20	8 ± 3.2(tot)	11	16 ± 4.3(tot)	15
UBM > 30	2 ± 1.5(tot)	6	9 ± 3.1(tot)	8
UBM > 40	0	3	5 ± 2.3(tot)	5
UBM > 60	0	0	2 ± 1.5(tot)	2
UBM > 90	0	0	0	0

TABLE 7.5: Result table for $\mu\mu + \mu$ (left) and $\mu\mu + e$ (right) signature, with at least three jets from data. Total number of events observed in the search regions, and corresponding background predictions. The uncertainty includes the statistical and systematic.

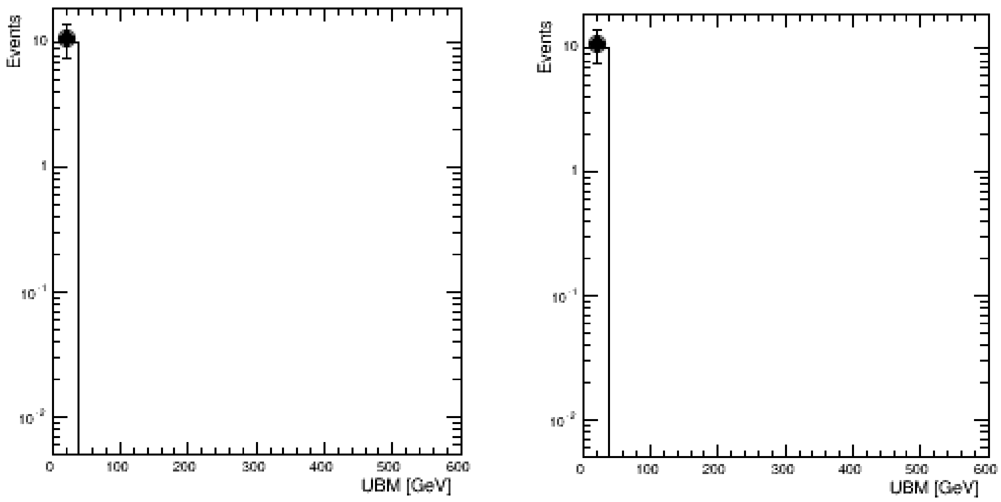

FIGURE 7.2: $\mu\mu + \mu\mu$ channel(left), $\mu\mu + ee$ channel(right). Result for SM prediction from control region and observation from signal region from data.

7.2.1 Limits on mSUGRA benchmark model

The observed number of events in the search region is compared to that expected from Monte Carlo simulation. We observed good agreement with the SM expectation. Total number of observed in the search regions, and corresponding background predictions are shown in Table 7.6 with various UBM requirements. The observed events in the signal region is in the range of 1 sigma uncertainty. The exclusion is confirmed in the context of the SUSY benchmark model, where the parameter space with the common gaugino mass $m_{1/2}$ = 175 GeV/c^2, the common scalar mass $m_0 = 1,450$ GeV/c^2, tan$\beta = 50$, $A_0 = 0$ in mSUGRA.

LM9	UBM > 0	10	20	30	40	60	90
Observed Limit	52.4329	49.7505	49.5824	61.7874	63.6583	71.2048	96.4578
Expected Limit	51.7069	49.2638	49.2779	60.5624	62.4752	68.28	95.5687
Expected $-\sigma$	39.0769	31.2661	40.6294	44.4737	45.168	53.1	79.1973
Expected $+\sigma$	73.2502	69.1255	67.2747	81.1776	79.93	91.7327	130.011

TABLE 7.6: 95% C.L. CLs observed limits and Expected limits for LM9, jet inclusive from data.

7.2.2 Limits on Simplified Models with trilepton signature

The results of the three-lepton search are displayed in Figure 7.3, 7.4. We set limits on SMS model with m(chi1+) = m(chi20) : 100 $\sim$ 500 GeV, m(chi10): 0 $\sim$ 400 GeV.

The efficiency and observed cross section times branching fraction is shown in Figure 7.3, and the limits of the three muon search is displaced in Figure 7.4.

The figure describes the 95% CL upper limit on the cross section times branching fraction in the $m_{\tilde{\chi}_1^0}$ versus $m_{\tilde{\chi}_2^0}$ (= $m_{\tilde{\chi}_1^\pm}$) plane in the described in the introduction. The sensitivity for the values of $\chi_{\tilde{l}}$ is not considered here, so there is no limit curve for this search. That results indicates no excess and the 95% CL upper limit on the chargino-neutralino production NLO cross section times branching fraction in the scenario for the three-lepton search.

7.2.3 Limits on Simplified Models with on-shell W and Z

The second results of scenario for limits is SMS, m(chi1+) = m(chi20) : 100 $\sim$ 1000 Gev, m(chi10) : 0 $\sim$ 975 GeV. The Figure 11, 12 display the efficiencies and cross section, limits from on-shell W and Z analysis. The efficiency and observed cross section is shown in Figure 7.3, and the limits of the three muon search is displaced in Figure 7.4.

We calculated the limits on the three-lepton analysis with CLs method to evaluate upper limits on the process of on-shell W and Z. Assuming 100% branching fractions of the chargino to $W + \tilde{\chi}_1^0$ and neutralino to $Z + \tilde{\chi}_1^0$, we calculate upper limits on the cross section for chargino-neutralino production times branching fractions into the WZ + $\not{E}_T$T final state as a function of the chargino and neutralino masses. There is no excess for new physics of this scenario here. The sensitivity of the three-lepton and WZ/ZZ + $\not{E}_T$ analyses are complementary, with the three-lepton results, which dominates the sensitivity in the region where the difference between the neutralino masses is small. And the WZ/ZZ + $\not{E}_T$ results dominating the sensitivity in the region where $m_{\tilde{\chi}_2^0} = m_{\tilde{\chi}_1^\pm}$ is large. The observed and expected limits are shown in Figure 7.5, 7.6.

7.2.4 Limits on GMSB Higgs boson

We set the limits on the third scenario, gauge-mediated symmetry breaking(GMSB) higgsino model[84][85][86], which has a large branching fraction to the ZZ + E_T^{miss} final state. An almost massless gravitino is the LSP in this model, and the next-to-lightest neutralino is a Z-enriched higgsino. The LSP in this model is an almost massless gravitino, the next-to-lightest SUSY particle is a Z-enriched higgsino $\tilde{\chi}_1^0$, and the $\tilde{\chi}_1^\pm$ is nearly degenerate in mass with the $\tilde{\chi}_1^0$. The branching fraction to the multilepton final state varies from 100% at m = 130 GeV to 85% at m = 410 GeV.

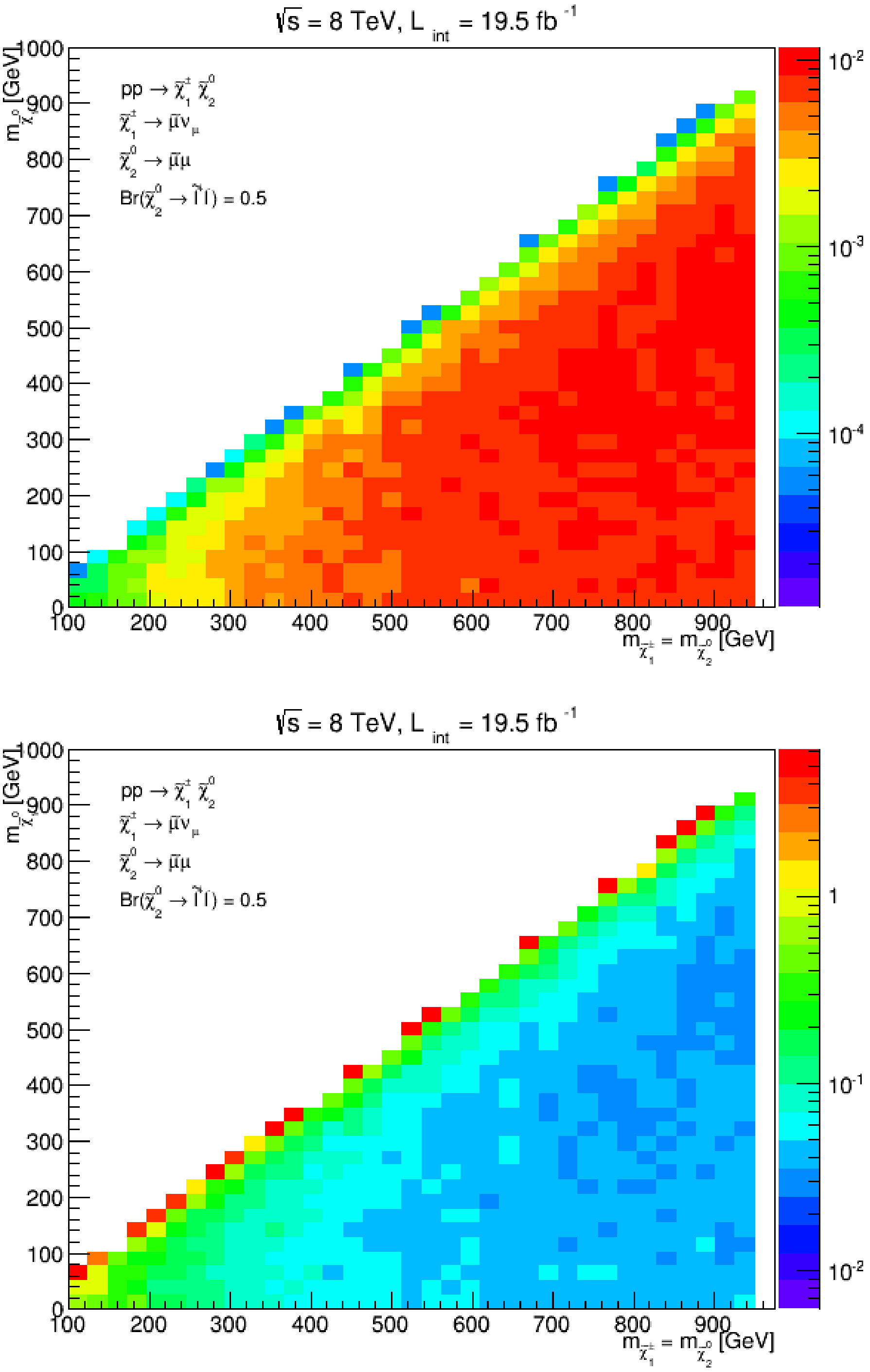

FIGURE 7.3: The efficiency(left) and measured cross section(right) for TChiSlepSnu. The effective cross section is the production cross section times BR=0.5.

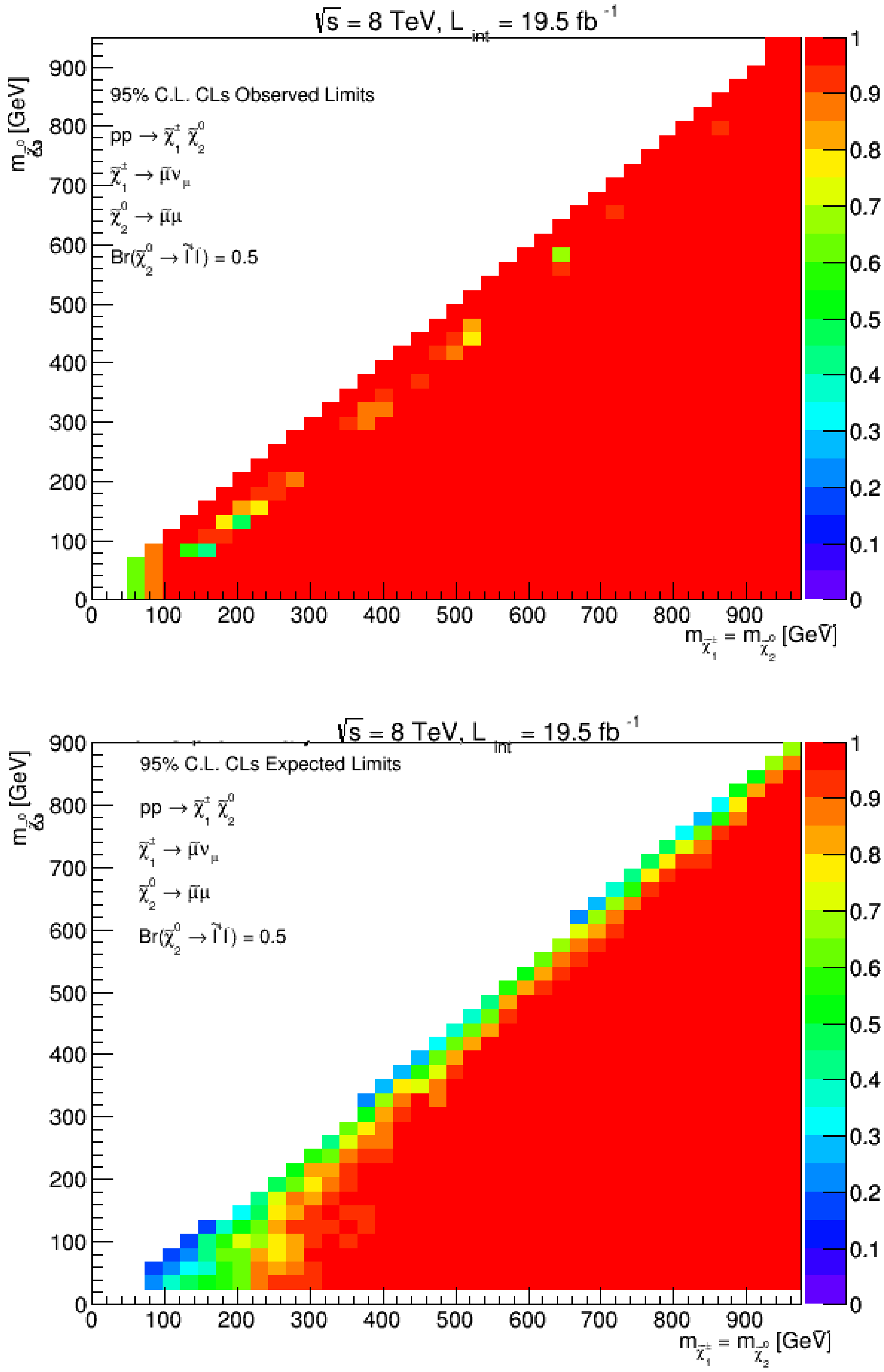

FIGURE 7.4: The 95% C.L. CLs observed limits(left) and expected limits(right) for TChiSlepSnu from data.

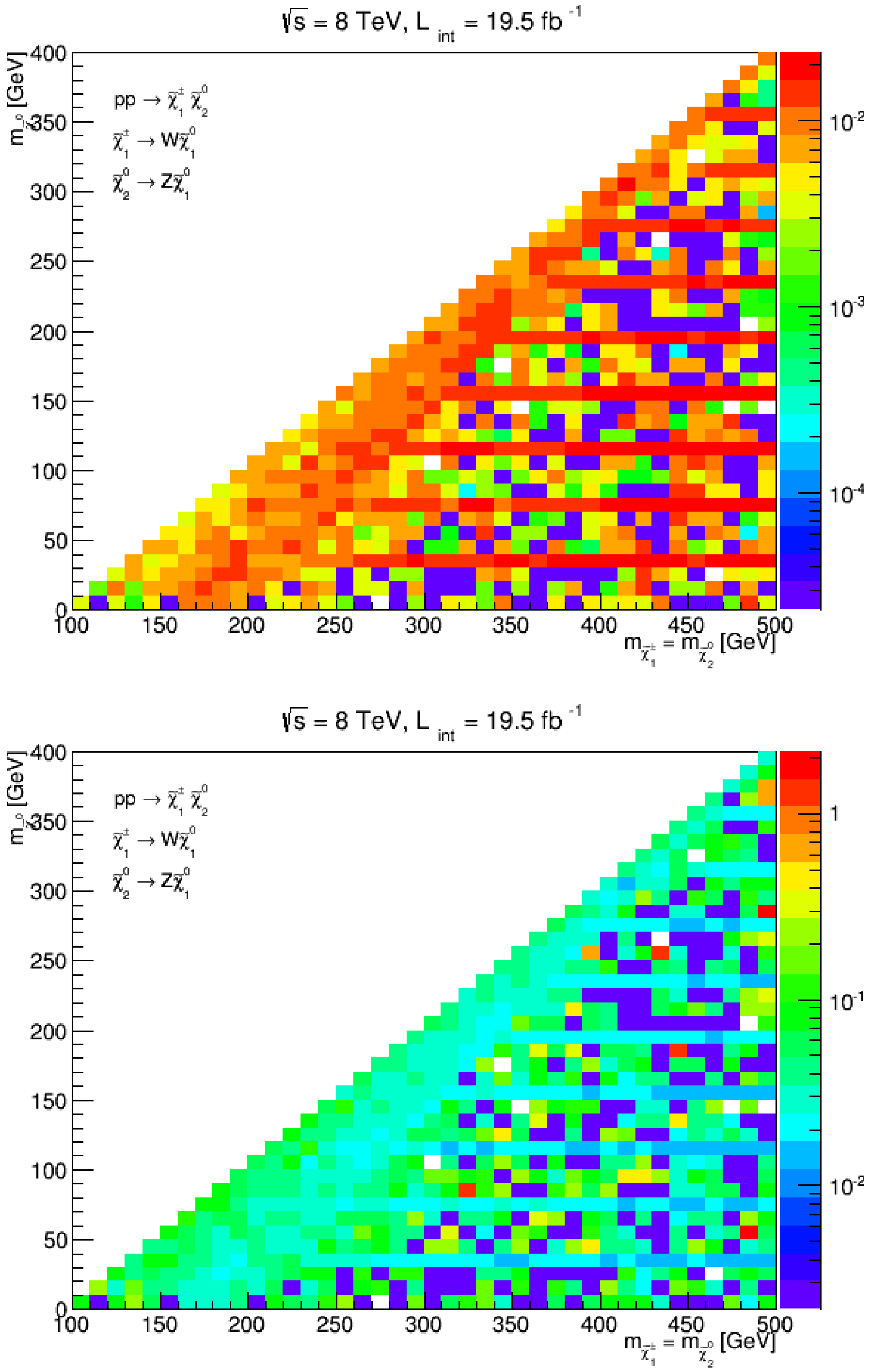

FIGURE 7.5: The efficiency(left) and measured cross section(right) for TChiWZ.

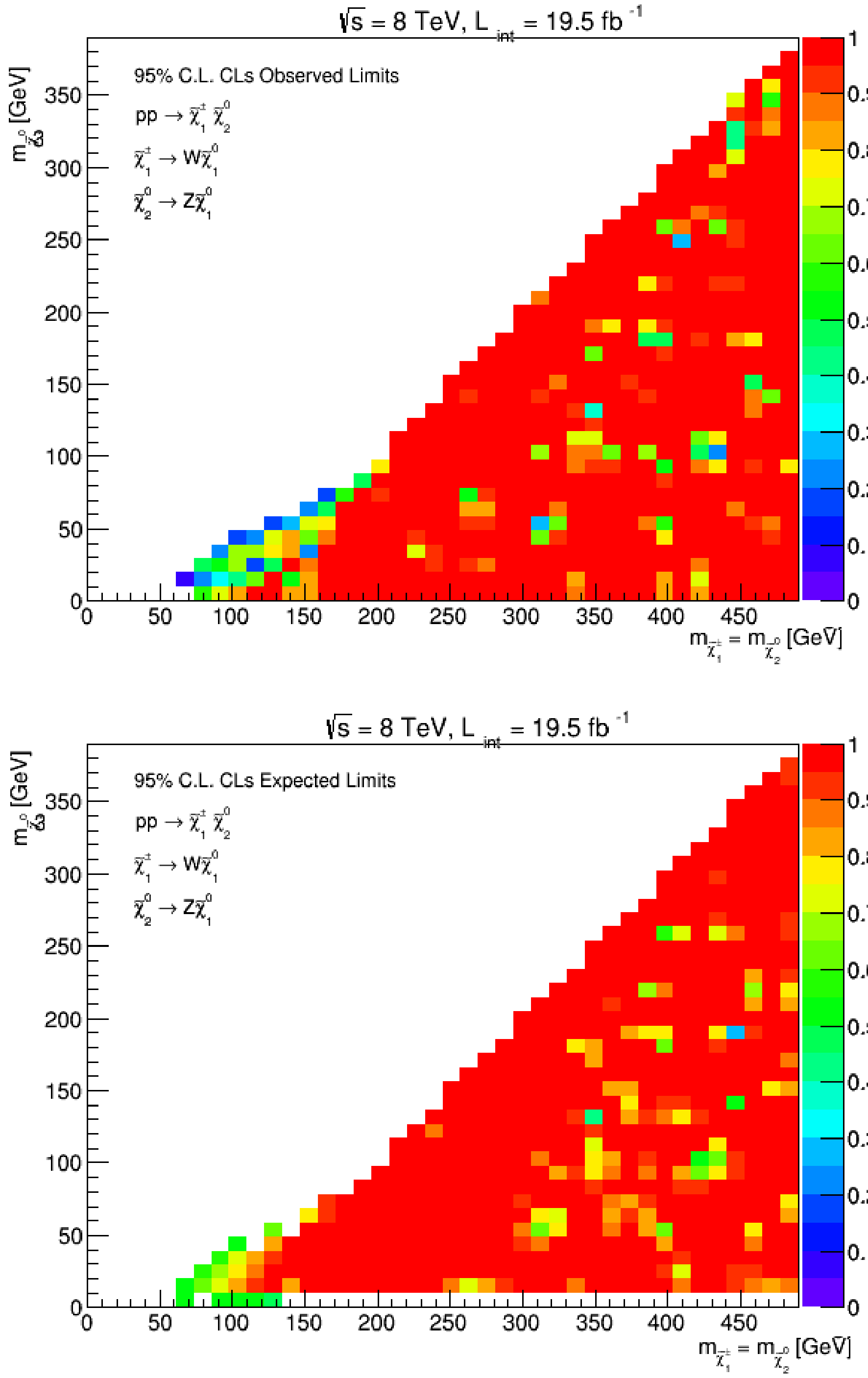

FIGURE 7.6: The 95% C.L. CLs observed limits(left) and expected limits(right) for TChiWZ from data.

Table 7.7 lists the signal efficiency for $\mu\mu+\mu$, and the Table 7.8, 7.9, 7.10 shows that for $\mu\mu+e$, $\mu\mu+\mu\mu$, $\mu\mu+ee$. The results for the three muons channel is shown in Figure 7.7 as a function of the gaugino mass parameter μ, where $\tilde{\chi}_1^0 \sim \tilde{\chi}_2^0 \sim \tilde{\chi}_1^0 \sim \mu$ to within typical mass differences of a few GeV. The calculated limits are listed in Table 7.11 $\sim$ 7.14.

The 95% C.L. upper limits were set on the gaugino mass parameters $M_1 = M_2 = 1$ TeV , the ration of Higgs expectation values tan β up to 2. The results of the GMSB analysis are displayed in Figure 7.7 $\sim$ 7.10 including the three and four leptons signature, $\mu\mu+\mu$, $\mu\mu+e$, $\mu\mu+\mu\mu$, $\mu\mu+ee$. In this analysis, the region $\mu < 330$ GeV is excluded at 95% confidence level for $\mu\mu+\mu$ channel. And the region $\mu < 310$ GeV is excluded at 95% confidence level for $\mu\mu+e$ channel.

And the GMSB models with regions of μ between 330 and 370 for $\mu\mu+\mu$ and over 310 for $\mu\mu+e$ has the theoretical cross section out of the expected limit with two sigma at 95% confidence level as shown in Figure 7.7, 7.8. Therefore the models with that excess is proposed to check across with other relevant study.

For the GMSB with four leptons search, the region $\mu < 410$ GeV is excluded at 95% confidence level for both of $\mu\mu+\mu\mu$ and $\mu\mu+ee$ scenarios.

parameter μ	signal efficiency	total error
110	3.33332e-06	± 4.54606e-07
130	0	± 0
150	3.33332e-06	± 4.54606e-07
170	6.66667e-06	± 9.09213e-07
190	2.00001e-05	± 2.72765e-06
210	1.33333e-05	± 1.81842e-06
230	1.66667e-05	± 2.27303e-06
250	1.66667e-05	± 2.27303e-06
270	4.33333e-05	± 5.90988e-06
290	5.66666e-05	± 7.7283e-06
310	6.66667e-05	± 9.09212e-06
330	4.33333e-05	± 5.90987e-06
350	2.33333e-05	± 3.18224e-06
370	7e-05	± 9.54672e-06
390	8.66667e-05	± 1.18198e-05
410	8.33333e-05	± 1.13651e-05

TABLE 7.7: Table of signal efficiency for GMSB $\mu\mu+\mu$ channel. $tan\beta = 2, M_1 = M_2 =$ 1 TeV.

parameter μ	signal efficiency	total error
110	0	$\pm$ 0
130	3.33334e-06	$\pm$ 4.54607e-07
150	0	$\pm$ 0
170	6.66667e-06	$\pm$ 9.09213e-07
190	1e-05	$\pm$ 1.36382e-06
210	1.33333e-05	$\pm$ 1.81842e-06
230	2.33333e-05	$\pm$ 3.18224e-06
250	4e-05	$\pm$ 5.45527e-06
270	2.66667e-05	$\pm$ 3.63685e-06
290	5e-05	$\pm$ 6.81909e-06
310	5.66667e-05	$\pm$ 7.7283e-06
330	2e-05	$\pm$ 2.72764e-06
350	7e-05	$\pm$ 9.54673e-06
370	5.33334e-05	$\pm$ 7.2737e-06
390	8e-05	$\pm$ 1.09105e-05
410	8.66667e-05	$\pm$ 1.18198e-05

TABLE 7.8: Table of signal efficiency for GMSB $\mu\mu$+e channel. $tan\beta = 2, M_1 = M_2 = 1$ TeV.

parameter μ	signal efficiency	total error
110	0	$\pm$ 0
130	0	$\pm$ 0
150	0	$\pm$ 0
170	0	$\pm$ 0
190	1e-05	$\pm$ 1.36382e-06
210	1.66667e-05	$\pm$ 2.27303e-06
230	6.66668e-06	$\pm$ 9.09214e-07
250	6.66666e-06	$\pm$ 9.09211e-07
270	3.33333e-05	$\pm$ 4.54606e-06
290	2e-05	$\pm$ 2.72764e-06
310	2.66667e-05	$\pm$ 3.63685e-06
330	2e-05	$\pm$ 2.72764e-06
350	4.33333e-05	$\pm$ 5.90988e-06
370	5.33333e-05	$\pm$ 7.2737e-06
390	5.66667e-05	$\pm$ 7.7283e-06
410	5e-05	$\pm$ 6.81909e-06

TABLE 7.9: Table of signal efficiency for GMSB $\mu\mu + \mu\mu$ channel. $tan\beta = 2, M_1 = M_2 = 1$ TeV.

parameter μ	signal efficiency	total error
110	0	$\pm$ 0
130	0	$\pm$ 0
150	0	$\pm$ 0
170	6.66666e-06	$\pm$ 9.09211e-07
190	6.66668e-06	$\pm$ 9.09214e-07
210	1.33333e-05	$\pm$ 1.81842e-06
230	3.33333e-06	$\pm$ 4.54605e-07
250	0	$\pm$ 0
270	1.33333e-05	$\pm$ 1.81842e-06
290	1.33333e-05	$\pm$ 1.81842e-06
310	1.66667e-05	$\pm$ 2.27303e-06
330	6.66667e-06	$\pm$ 9.09212e-07
350	1.66667e-05	$\pm$ 2.27303e-06
370	2e-05	$\pm$ 2.72764e-06
390	1.66667e-05	$\pm$ 2.27303e-06
410	2.33333e-05	$\pm$ 3.18224e-06

TABLE 7.10: Table of signal efficiency for GMSB $\mu\mu + ee$ channel. $tan\beta = 2, M_1 = M_2 = 1$ TeV.

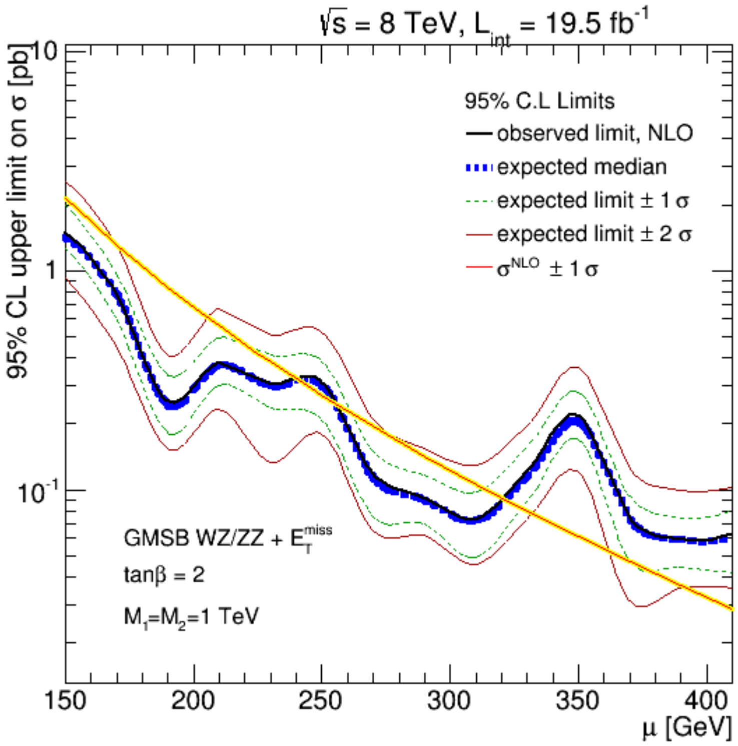

FIGURE 7.7: $\mu\mu + \mu$ channel. The observed limits and expected limits for GMSB higgsino model decaying three muons.

parameter μ	theoretical cs	95% C.L upper limit	-2 sigma	-1 sigma	expected limit(median)	+1 sigma	+2 sigma
110	7,288	-	-	-	-	-	-
130	3,764	-	-	-	-	-	-
150	2,141	1483.83	921.376	1266.87	1421.92	1994.99	2554.85
170	1,304	774.452	443.619	593.894	771.141	953.255	1293.68
190	837	252.702	153.384	181.959	244.636	333.228	412.678
210	558	376.261	232.442	674.303	370.741	493.709	674.303
230	382	303.292	133.12	237.67	297.424	409.708	509.533
250	271	309.491	179.286	208.267	299.672	386.2	525.587
270	195	117.874	64.8236	75.4351	113.439	149.299	208.923
290	142	91.4555	61.7728	69.55	89.6244	116.826	153.886
310	106	73.136	45.6516	49.2273	72.4249	97.2609	129.617
330	79.8	120.427	73.4193	88.7725	114.468	157.283	195.589
350	60.8	216.991	120.019	169.212	204.852	278.252	360.162
370	46.8	73.7471	31.0615	47.3307	72.5988	93.0427	123.08
390	36.6	59.0769	35.5878	44.3648	59.1029	74.5297	99.9335
410	28.7	62.1997	35.6715	41.9857	60.6599	80.9422	102.241

TABLE 7.11: Table of production cross section(fb) for GMSB $\mu\mu + \mu$ channel. $tan\beta = 2, M_1 = M_2 = 1$ TeV.

parameter μ	theoretical cs	95% C.L upper limit	-2 sigma	-1 sigma	expected limit(median)	+1 sigma	+2 sigma
110	7,288	-	-	-	-	-	-
130	3,764	3771.13	2450.35	2890.04	3747.75	4710.77	6294.46
150	2,141	-	-	-	-	-	-
170	1,304	1896.7	1054.53	1429.51	1902.52	2461.41	3133.16
190	837	1208.73	690.819	928.244	1201.44	1632.48	2112.45
210	558	914.381	647.645	718.421	912.143	1210.41	1578.28
230	382	522.151	279.476	339.028	523.588	713.258	948.263
250	271	292.837	198.2	234.85	292.341	428.599	522.573
270	195	468.798	194.774	356.772	467.189	598.08	783.483
290	142	244.258	150.6	190.865	247.081	319.16	413.142
310	106	213.647	120.011	173.855	202.529	270.148	384.742
330	79.8	616.777	282.136	500.121	629.97	845.891	1053.97
350	60.8	171.533	111.405	134.664	168.542	242.198	299.671
370	46.8	231.251	95.7232	171.945	233.683	317.069	395.14
390	36.6	158.705	89.909	120.026	159.229	201.387	262.199
410	28.7	139.007	52.7605	119.17	141.881	193.543	239.018

TABLE 7.12: Table of production cross section(fb) for GMSB $\mu\mu + e$ channel. $tan\beta = 2, M_1 = M_2 = 1$ TeV.

parameter μ	theoretical cs	95% C.L upper limit	-2 sigma	-1 sigma	expected limit(median)	+1 sigma	+2 sigma
110	7,288	-	-	-	-	-	-
130	3,764	-	-	-	-	-	-
150	2,141	-	-	-	-	-	-
170	1,304	-	-	-	-	-	-
190	837	61.4773	29.6278	37.1175	57.6233	75.3585	106.053
210	558	93.6828	44.4417	63.0784	85.323	112.3	152.774
230	382	88.5277	48.9925	58.3022	76.3463	112.57	159.421
250	271	86.4469	45.1654	55.3106	79.4788	119.601	164.846
270	195	18.5035	8.74723	11.3236	17.7675	22.2786	31.8574
290	142	29.7705	15.6129	19.2237	28.2469	39.9829	54.5949
310	106	23.8414	12.851	16.3081	21.5816	27.2649	40.2659
330	79.8	29.4071	15.6506	17.6845	26.5686	37.4626	52.2354
350	60.8	13.5414	7.68617	9.70345	12.4386	16.9226	23.538
370	46.8	11.0128	7.25897	7.65999	9.42254	14.1666	19.1069
390	36.6	10.263	5.65546	7.22778	9.66451	13.5885	18.9586
410	28.7	11.7513	7.05421	9.07268	11.3349	15.7285	21.507

TABLE 7.13: Table of production cross section(fb) for GMSB $\mu\mu + \mu\mu$ channel. $tan\beta = 2, M_1 = M_2 = 1$ TeV.

parameter μ	theoretical cs	95% C.L upper limit	-2 sigma	-1 sigma	expected limit(median)	+1 sigma	+2 sigma
110	7,288	-	-	-	-	-	-
130	3,764	-	-	-	-	-	-
150	2,141	-	-	-	-	-	-
170	1,304	89.1883	33.0406	60.5851	75.6628	112.106	164.526
190	837	91.6269	56.479	65.1831	85.4675	114.483	152.114
210	558	43.4142	23.2116	28.5303	41.3711	56.557	76.1972
230	382	166.96	79.1461	104.606	150.19	234.2	335.149
250	271	-	-	-	-	-	-
270	195	45.0077	25.2589	33.0653	40.4937	56.7397	82.4787
290	142	45.8766	20.1813	30.9676	40.3889	56.1192	79.1754
310	106	34.6166	14.629	22.126	30.5308	46.5736	65.1796
330	79.8	91.9235	41.9317	67.0738	84.0506	121.512	153.498
350	60.8	34.8904	19.6008	24.0378	32.9379	47.7968	64.1884
370	46.8	29.2825	18.2597	21.9651	25.378	36.5704	51.237
390	36.6	35.647	18.2583	21.8969	33.0293	44.2858	65.928
410	28.7	25.9598	10.36	18.4575	22.6298	32.6797	43.1452

TABLE 7.14: Table of production cross section(fb) for GMSB $\mu\mu + ee$ channel. $tan\beta = 2, M_1 = M_2 = 1$ TeV.

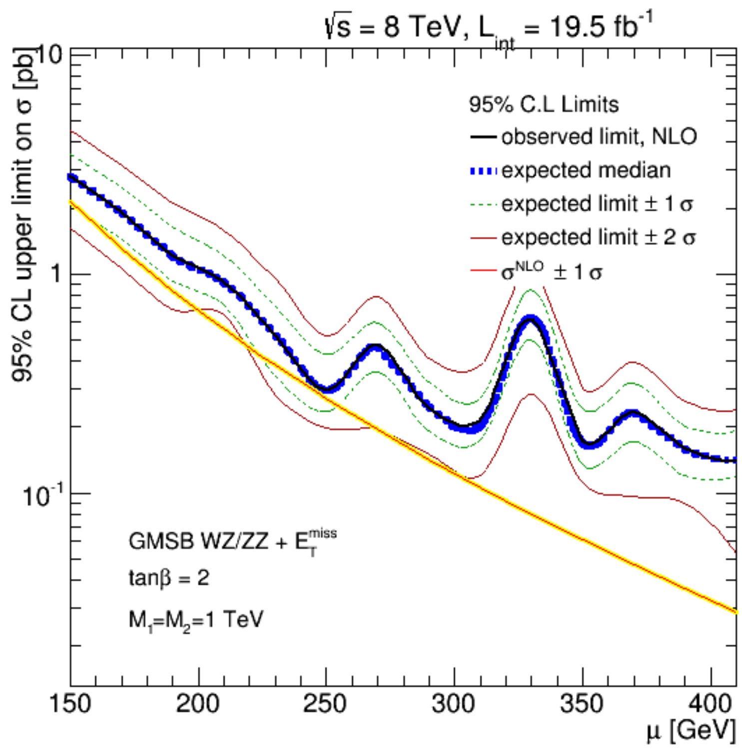

FIGURE 7.8: $\mu\mu + e$ channel. The observed limits and expected limits for GMSB higgsino model decaying three muons and one electron.

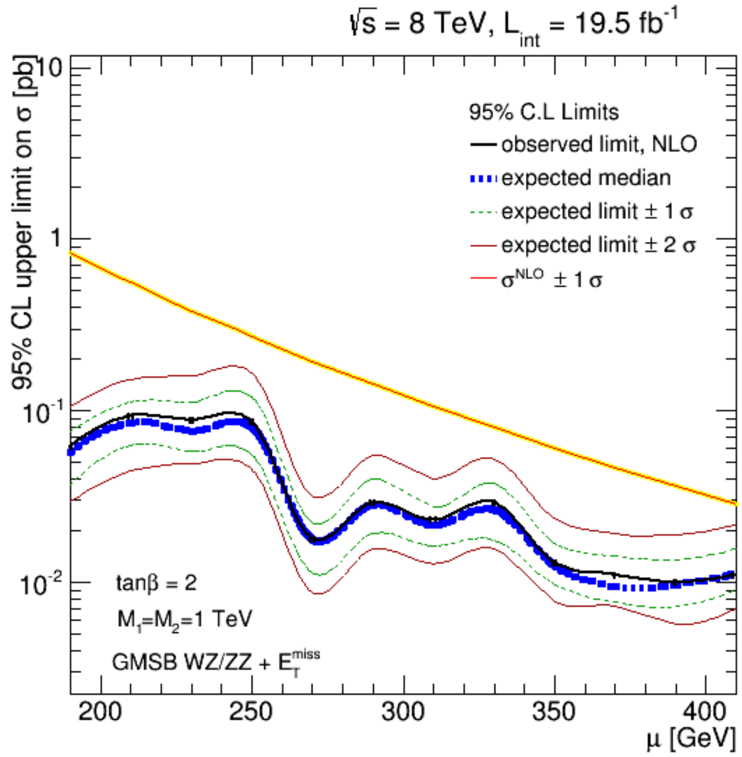

FIGURE 7.9: $\mu\mu + \mu\mu$ channel. The observed limits and expected limits for GMSB higgsino model decaying four muons.

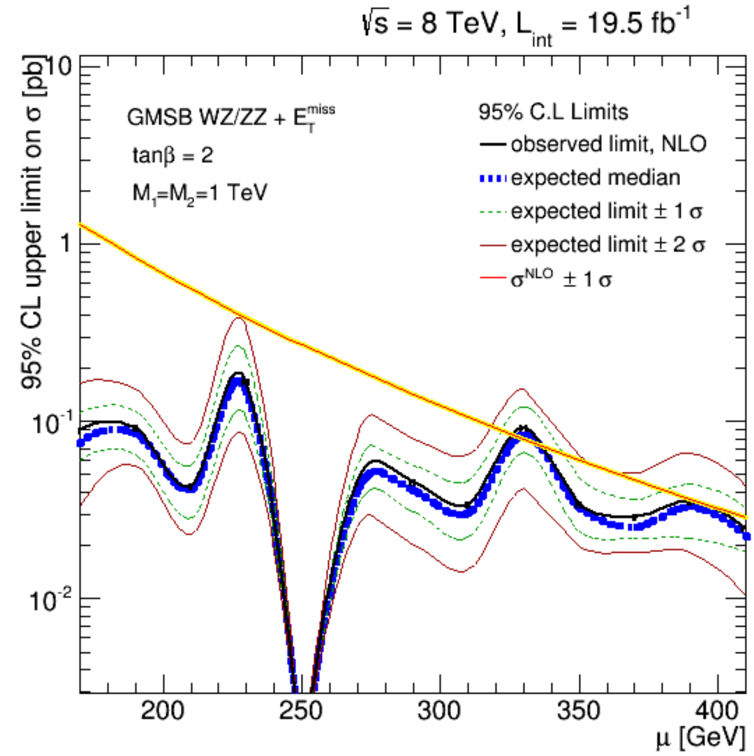

FIGURE 7.10: $\mu\mu + ee$ channel. The observed limits and expected limits for GMSB higgsino model decaying two muons and tow electrons.

Chapter 8

Conclusion

We present the results of searches for supersymmetric charginos, neutralinos, and sleptons decaying to three leptons, four leptons and missing transverse energy. The results agree the standard model and there is no excess for the Simplified Model of SUSY. The results display the exclusion result from SMS models with charginos, neutralinos, and sleptons.

The GMSB Higgsino model is excluded the region with the mass parameter $\mu < 330$ for signature with $\mu\mu + \mu$ and $\mu < 310$ for $\mu\mu + e$, the 95% C.L. Limits were set as a function of gaugino mass parameter. The model is also excluded the region under the higgs mass parameter μ of 410 for both of $\mu\mu + \mu\mu$ and $\mu\mu + ee$ channels.

And the GMSB models with region of μ between 330 and 370 for $\mu\mu + \mu$ and over 310 for $\mu\mu + e$ has the theoretical cross section out of the 95% C.L expected limit with two sigma, so that is proposed to check across with relevant study repeatedly.

Bibliography

[1] D. Griffiths, "Introduction to Elementary Particles, 2nd Ed.". Wiley, 2008.

[2] M. Veltman, "Facts and Mysteries in Elementary Particle Physics". World Scientific, 2003.

[3] P.W. Higgs, Phys. Lett. 12, 132 (1964).

[4] P.W. Higgs, Phys. Rev. Lett. 13, 508 (1964).

[5] F. Englert and R. Brout, Phys. Rev. Lett. 13, 321 (1964).

[6] G. Guralnik, C. Hagen, and T. Kibble, Phys. Rev. Lett. 13, 585 (1964).

[7] P.W. Higgs, Phys. Rev. 145, 1156 (1966).

[8] E. Witten, Phys. Lett. B 105, 267 (1981).

[9] http://indico.cern.ch/contributionDisplay.py?contribId=77&sessionId=15&confId=24657

[10] S. L. Glashow, Partial Symmetries of Weak Interactions, Nucl. Phys. 22, 579-588 (1961).

[11] S.Weinberg, A Model of Leptons, Phys. Rev. Lett. 19, 1264-1266 (1967).

[12] A. Salam, Elementary Particle Physics, N. Svartholm ed., Almquvist and Wiksell, Stockholm (1968).

[13] M.E. Peskin, D.V. Schroeder, An Introduction To Quantum Field Theory, Westview Press, (1995).

[14] S. Weinberg, The Quantum Theory of Fields, Cambridge University Press, vol. 1,2,3 (1995, 1996, 2000).

[15] Particle Data Group http://pdg.lbl.gov/ Phys Rev D86, 010001 (2012).

[16] H. Murayama. Supersymmetry Phenomenology. arXiv:hep-ph/0002232v2, (2000).

[17] 2012 J. Phys. G: Nucl. Part. Phys. 39 105005.

[18] P. Meade, N. Seiberg, and D. Shih, Prog. Theor. Phys. Suppl. 177, 143, 0801.3278 (2009).

[19] P. Meade, N. Seiberg, and D. Shih, Prog. Theor. Phys. Suppl. 177, 143, 0801.3278(2009).

[20] L. M. Carpenter, M. Dine, G. Festuccia, and J. D. Mason, Phys. Rev. D79, 035002, 0805.2944 (2009).

[21] L. M. Carpenter, 0812.2051 (2008).

[22] M. Buican, P. Meade, N. Seiberg, and D. Shih, JHEP 03, 016, 0812.3668 (2009).

[23] A. Rajaraman, Y. Shirman, J. Smidt, and F. Yu, Phys. Lett. B678, 367, 0903.0668 (2009).

[24] J. T. Ruderman and D. Shih, JHEP 11, 046, 1009.1665 (2010).

[25] H. Baer, K. Hagiwara, and X. Tata, Phys. Rev. D35, 1598 (1987).

[26] H. Baer and X. Tata, Phys. Rev. D47, 2739 (1993).

[27] H. Baer, C. Kao, and X. Tata, Phys. Rev. D48, 5175, hep-ph/9307347 (1993).

[28] H. Baer, C.-h. Chen, F. Paige, and X. Tata, Phys. Rev. D50, 4508, hep-ph/9404212 (1994).

[29] K. T. Matchev and D. M. Pierce, Phys. Lett. B467, 225, hep-ph/9907505 (1999).

[30] K. T. Matchev and D. M. Pierce, Phys. Rev. D60, 075004, hep-ph/9904282 (1999).

[31] The CMS Collaboration, Interpretation of Searches for Supersymmetry with Simplified Models, CMS Physics Analysis Summary CMS-PAS-SUS-11-016 (2011).

[32] H. Baer et al. The Reach of the CERN Large Hadron Collider for Gauge-Mediated Supersymmetry Breaking Models. FSU-HEP-000328 (2000).

[33] R. L. Culbertson et al. Low scale and gauge mediated supersymmetry breaking at the Fermilab Tevatron Run II. arXive:hep-ph/0008070 (2000).

[34] Yurii Maravin, Tevatron Searches for GMSB and RPV SUSY, these proceedings.

[35] H. Baer et al. Weak Scale Supersymmetry. Cambridge University Press (2006).

[36] R. Haag et al. All possible generators of supersymmetries of the S-matrix. Nucl. Phys. B 88. 257 (1975).

[37] S. Coleman et al. All Possible Symmetries of the S Matrix. Phys. Rev. 159. 1251 (1967).

[38] The CMS Coooaboration, "Observation of a new boson at a mass of 125 GeV with the CMS experiment at the LHC", arXiv:1207.7214v1 (2012).

[39] Avishek Chatterjee, "SEARCH FOR SUPERSYMMETRY IN EVENTS WITH A SINGLE LEPTON, JETS, AND MISSING TRANSVERSE MOMENTUM USING A NEURAL NETWORK", Ph.D. Thesis. Cornell University: USA (2013).

[40] Sho Maruyama, "Supersymmetry Search in Multilepton Final States with Taus Using the CMS Detector at the LHC", Ph.D. Thesis. University of California: USA (2011).

[41] Gruttola Michele, "The $Z \rightarrow \mu^+\mu^-$ decay channel in the CMS experiment at LHC: from cross section measurement with the 2010 7 TeV collision dataset to offline machine luminosity monitor", Ph.D. Thesis, Universita degli Studi di Napoli: Italy (2010).

[42] Abdelhamid Albaid, "Higgs boson Mass in GMSB with Messenger-Matter mixing", Nuclear Physics B Proceedings Suppllement 00 1-8 (2012).

[43] Marco Meneghelli, "Evidence for a new boson in the search for the Standard Model Higgs particle decaying to four leptons at CMS", Ph.D. Thesis, Universita di Bologna: Italy (2013)

[44] Oleg Brandt, "Search for Supersymmetry in Trilepton Final States with the ATLAS Detector and the Alignment of the ATLAS Silicon Tracker", Ph.D. Thesis, University of Oxford: U.K (2009).

[45] CMS Physics Technical Design report, Vol I: Detector Performance and Software, CERN/LHCC 2006-001, CMS TDR 8.1, Cap 8.

[46] The CMS Collaboration, Absolute Calibration of the Luminosity Measurement at CMS: Winter 2012 Update, CMS PAS SMP-12-008.

[47] The CMS Collaboration, Electron reconstruction and identification at $\sqrt{s} = 7$ TeV, CMS Physics Analysis Summary CMS-PAS-EGM-10-004 (2010).

[48] The CMS Collaboration, Performance of muon identification in pp collisions at $\sqrt{s}$ = 7 TeV, CMS Physics Analysis Summary CMS-PAS-MUO-10-002 (2010).

[49] The CMS Collaboration. CMS Strategies for tau reconstruction and identification using particle-flow techniques. CMS PAS PFT-08-001, (2008).

[50] The ROOT team. The ROOT Users Guide, 2009. URL http://root.cern.ch/drupal/.

[51] W. Beenakker et al. PROSPINO: A Program for the Production of Supersymmetric Particles in Next-to-leading Order QCD. arXiv:hep-ph/9611232v1 (1996).

[52] The CMS Collaboration, Multileptonic SUSY searches, CMS Physics Analysis Summary CMS-PAS-SUS-11-013 (2011).

[53] The CMS Collaboration, A Search for Supersymmetry with three or more leptons using 4.7 fb^{-1} of $sqrts = 7$ TeV CMS data., CMS Physics Analysis Summary CMS-PAS-SUS-11-020 (2011).

[54] https://twiki.cern.ch/twiki/bin/view/CMS/SimpleCutBasedEleID

[55] The CMS Collaboration, Search for new physics with same-sign isolated dilepton events with jets and missing energy, CMS Physics Analysis Summary CMS-PAS-SUS-11-010 (2011).

[56] The CMS Collaboration, CMS Luminosity Based on Pixel Cluster Counting - Summer 2012 Update, CMS PAS LUM-12-001 (2012)

[57] The CMS Collaboration, Absolute luminosity normalization, CMS Detector Performance Summary CMS-DP-2011-003 (2011).

[58] The CMS Collaboration, Electron reconstruction and identification at $\sqrt{s}$=7 TeV, CMS Physics Analysis Summary CMS-PAS-EGM-10-004 (2010).

[59] The CMS Collaboration, Performance of muon identification in pp collisions at $\sqrt{s}$ = 7 TeV, CMS Physics Analysis Summary CMS-PAS-MUO-10-002 (2010).

[60] The CMS Collaboration, Performance of muon reconstruction and identification in pp collisions at $\sqrt{s} = 7$ TeV, CMS Physics Analysis Summary CMS-PAS-MUO-10-004 (2010).

[61] E. Di Marco et al., Search for Higgs Boson Decays to TwoWBosons in the Fully Leptonic Final State with Full 2011 pp Dataset at p s = 7 TeV, CMS Analysis Note AN-2011/432 (2011).

[62] S. Arora et al., A Search for Direct Chargino Neutralino production with three or more leptons using 9.5 fb^{-1} of $\sqrt{s}$=8 TeV CMS data, CMS Analysis Note AN-2012/256, (2012).

[63] Missing transverse energy performance of the CMS detector, JINST 6 P09001 doi:10.1088/1748-0221/6/09/P09001 (2011).

[64] Performance of Missing Transverse Momentum Reconstruction Algorithms in Proton-Proton Collisions at $\sqrt{s} = 8$ TeV with the CMS Detector, CMS PAS JME-12-002.

[65] The CMS Collaboration, ‘’Jet Energy Corrections determination at $\sqrt{s} = 7$ TeV, CMS-PAS JME 10-010 (2010).

[66] The CMS Collaboration, "Missing Transverse energy Performance in Minimum-Bias and Jet Events from Proton-Proton Collisions at $\sqrt{s} = 7TeV$", CMS-PAS JME 10-004 (2010).

[67] A. L. Read, Presentation of search results: The CLs technique, J. Phys. G 28, 2693, doi:10.1088/0954-3899/28/10/313 (2002).

[68] T. Junk, Confidence level computation for combining searches with small statistics,Nucl. Instrum. Meth. A 434, 435, doi:10.1016/S0168-9002(99)00498-2 (1999).

[69] ATLAS and CMS Collaborations, Procedure for the LHC Higgs boson search combination in summer 2011, Technical Report ATL-PHYS-PUB-2011-11, CMS-NOTE-2011-005, Geneva (2011).

[70] W. Beenakker et al., Production of charginos, neutralinos, and sleptons at hadron colliders, Phys. Rev. Lett. 83, 3780, doi:10.1103/PhysRevLett.83.3780 (1999).

[71] W. Beenakker et al., Erratum: production of charginos, neutralinos, and sleptons at hadron colliders, Phys. Rev. Lett. 100, 029901, doi:10.1103/PhysRevLett.100.029901 (2008).

[72] M. Kramer et al., Supersymmetry production cross sections in pp collisions at $\sqrt{s}$ = 7 TeV, (2012). arXiv:1206.2892.

[73] The CMS Collaboration, "Search for Physics Beyond the Standard Model Using Multilepton Signatures in $\sqrt{s} = 7$ TeV pp Collisions with the CMS Detector at the LHC", CMS PAS SUS-10-008 (2011).

[74] Mark Terwart, "Searches for GMSB at the LHC", arXiv:0805.2524v2 (2008).

[75] Daniele Alves et al., "Simplified Models for LHC New Physics Searches", arXiv:1105.2838v1 (2011).

[76] The CMS Collaboration, "Search for Physics Beyond the Standard Model in $Z + jets + \not{E}_T$ events at the LHC", CMS PAS SUS-10-010 (2011).

[77] The CMS Collaboration, "Searches for Supersymmetry using Multilepton Signatures in pp Collisions at 7 TeV", CMS PAS SUS-11-013 (2011).

[78] The CMS Collaboration, "Search for electroweak production of charginos, neutralinos, and sleptons using leptonic final states in pp collisions at $\sqrt{s} = 8$ TeV", CMS PAS SUS-12-022 (2012).

[79] The CMS Collaboration, "Search for stop in R-parity-violating supersymmetry with three or more leptons and b-tags", CMS PAS SUS-13-003 (2013).

[80] The CMS Collaboration, "Search for electroweak production of charginos, neutralinos, and sleptons using leptonic final states in pp collisions at $\sqrt{s} = 8$ TeV", CMS PAS SUS-13-006 (2013).

[81] The CMS Collaboration, "Search for supersymmetry in the 3 lepton + b-tag final state", CMS PAS SUS-13-008 (2013)

[82] I. Bertram et al., "A recipe for the construction of confidence limits", technical report, FERMILAB-TM-2104 (2000).

[83] Amnon Harel, "Statistical methods in CMS searches", http://indico.cern.ch /getFile.py/access?contribId=47&resId=0&materialId=paper&confId=107747 (2011).

[84] CMS Collaboration, Search for electroweak production of charginos and neutralinos using leptonic final states in pp collisions at ps = 7 TeV, JHEP 1211 (2012), doi:10.1007/JHEP11, 147, arXiv:1209.6620 (2012).

[85] K. T. Matchev and S. D. Thomas, Higgs and Z boson signatures of supersymmetry, Phys. Rev. D 62, 077702, doi:10.1103/PhysRevD.62.077702 (2000).

[86] P. Meade, M. Reece, and D. Shih, Prompt decays of general neutralino NLSPs at the Tevatron, JHEP 05, 105, doi:10.1007/JHEP05, 105 (2010).

거대강입자충돌실험에서 CMS검출기를 이용한 다중 경입자로 붕괴하는 초대칭성 힉스입자 탐색

김 재 호

전남대학교대학원 물리학과

(지도교수 : 김재률)

(국문초록)

본 연구에서는 질량중심 에너지가 8 TeV인 양성자-양성자 충돌에서의 초대칭성 힉스입자가 3개 또는 그 이상의 경입자로 붕괴하는 현상에 대한 탐색 결과를 기술하였다. 거대강입자충돌장치의 CMS 검출기를 이용하여 취득된 누적데이터는 그 휘도가 총 19.5 fb^{-1}에 해당된다. 연구에서는 표준모형으로부터 기인하는 배경사건을 예측하기 위해 데이터를 이용한 역추정 방식을 사용하였다. 본 연구는 $\mu\mu+\mu(\mu\mu)$ 과 $\mu\mu+e(ee)$ 붕괴 모드에 대한 연구를 각각 수행하였으며, 그 결과는 Simplified Model과 Gauge Mediated Supersymmetry Breaking Model에 대한 매개변수 공간에 대한 상한값을 설정하는 것으로 수행되었다.

그 중 $\mu\mu+\mu(e)$로 붕괴하는 GMSB 모델의 경우 힉스 질량 변수 μ가 330과 370의 사이의 값을 갖거나 310 이상의 값을 갖는 경우 해당 사건의 생성률이 95%신뢰 구간의 예상 상한값을 2σ 범위를 벗어나는 것으로 나타났다. 때문에 해당 구간값을 갖는 모델에 대한 여타의 분석방법을 통해 추가적인 비교연구가 수행될 필요가 있다.